OXIDATION OF MONOTERPENES IN THE ATMOSPHERE AND INDOOR ENVIRONMENTS

by

Olivia Jean Jenks

B.A., MANCHESTER UNIVERSITY, 2018

A thesis submitted to the Faculty of the Graduate School of the University of Colorado in partial fulfillment of the requirement for the degree of Doctor of Philosophy

Department of Chemistry

2024

Committee Members

Joost de Gouw

Paul Ziemann

Eleanor Browne

Jose Jimenez

Qing Ye

Jenks, Olivia (Ph.D., Chemistry)

OXIDATION OF MONTOERPENES IN THE ATMOSPHERE AND INDOOR ENVIRONMENTS

Thesis directed by Professor Joost de Gouw

Abstract

Monoterpenes are emitted into the atmosphere from vegetation and indoor products like personal care items and building materials. Once in the atmosphere, monoterpenes undergo oxidation by ozone (O_3), hydroxyl radicals (OH), and nitrate radicals (NO_3), forming secondary organic aerosol (SOA). These aerosols play crucial roles in the climate system, in limiting visibility, and impact human health. Aerosols reflect sunlight, contributing to a cooling of climate, and influence cloud properties. However, their small particle size enables them to penetrate deep into the lungs of humans, posing risks to cardiovascular and respiratory health.

My first project involved characterizing the gas-phase products of monoterpene oxidation, focusing on Δ-3-carene, α-pinene, β-pinene, ocimene, and limonene. Innovative techniques were developed to identify and quantify these products, including the use of tubing delay experiments with the Vocus mass spectrometer. Field studies in Los Angeles corroborated findings from the lab, highlighting the importance of both daytime and nighttime chemistry. The composition of the monoterpene oxidation products observed in the field were compared to that of the lab studies, contributing to a comprehensive understanding of atmospheric VOC oxidation processes.

My second project investigated the impact of germicidal ultraviolet (GUV) irradiation on indoor VOC oxidation. GUV has been widely used for air disinfection, particularly in public settings like hospitals and schools. However, its effect on indoor air quality remains poorly understood. By irradiating air that contains common indoor volatile organic compounds (VOCs),

like limonene, in a controlled chamber, the impact of GUV light on the monoterpene ozonolysis process was studied. This work contributes to a better understanding of the implications of GUV disinfection on indoor air quality and human health and will inform strategies for improving indoor air quality and reducing health risks associated with VOC exposure in indoor environments.

Acknowledgements

I extend my deepest gratitude to my advisor, Joost de Gouw, for your support, guidance, and mentorship throughout the entire journey of this dissertation. Your expertise, constructive feedback, and commitment to my academic and personal growth have been invaluable. I am truly fortunate to have had such a dedicated and inspiring mentor. Thank you for your encouragement, patience, and for instilling in me the passion for rigorous research. This dissertation is a testament to your commitment to excellence, and I am profoundly grateful for the immeasurable impact you have had on my academic and professional development.

I am immensely thankful for the profound influence of Dr. Susan Klein during my undergraduate studies. Your passion for and dedication to fostering intellectual curiosity left an indelible mark on my academic journey. Dr. Klein's unwavering support, challenging coursework, and genuine interest in my intellectual growth inspired me to pursue graduate studies. Your mentorship not only deepened my understanding of chemistry but also instilled in me the confidence and enthusiasm to embark on the challenging yet exciting path of graduate school. I am sincerely grateful for the pivotal role you played in shaping my academic aspirations.

I am incredibly blessed to have the unwavering support of my mom, dad, and brother throughout my academic journey. Your love, encouragement, and belief in my abilities have been my rock. You have been my pillars of strength, and I am deeply grateful for the sacrifices you have made and the constant encouragement you have provided. This achievement is as much yours as it is mine, and I could not have reached this milestone without each of you by my side. Thank you for being my greatest cheerleaders and the foundation of my success.

I want to express my deepest gratitude to my husband, Dylan, for being my unwavering source of support and love throughout this academic journey. Your encouragement, understanding,

and countless moments of reassurance have been my steady anchor. Your belief in my abilities, even when I doubted myself, has been the driving force behind my perseverance. Thank you for celebrating the highs, weathering the lows, and always standing by me with unwavering love. Your sacrifices and encouragement have made this achievement even more special, and I am profoundly grateful for the partnership we share in all aspects of life. I am lucky to have you by my side.

I want to extend my heartfelt thanks to my best friend and colleague, Mindy. Your steadfast support, camaraderie, and shared laughter have been the bright spots on this academic journey. Whether navigating challenges or celebrating victories, your presence has made every step memorable. Your insights, encouragement, and genuine friendship have been a source of strength. I am incredibly fortunate to have you not only as a colleague but as a confidante and true friend. Thank you for being an integral part of this journey and for making it richer with your friendship.

Marla, I am deeply grateful for the incredible support and guidance I've received from you. From the moment you took the time to train me to the countless hours spent working together on experiments, you have not only been an invaluable mentor but also a true friend. Your expertise, patience, and willingness to share her knowledge have significantly contributed to my growth in this role. Your kindness and camaraderie have turned our professional collaboration into a meaningful friendship. Thank you for your support and for being an instrumental part of my journey.

Thank you all so much,

Olivia Jean Jenks

Table of Contents

LIST OF FIGURES

LIST OF TABLES

Introduction

1.1. Oxidation of Monoterpenes in the Atmosphere

Monoterpenes (including α-pinene, ocimene, β-pinene, limonene, and Δ-3-carene) contribute around 15% to global biogenic volatile organic compound (BVOC) emissions, sourced from various ecosystems such as broadleaf tropical forests, shrubs, needleleaf forests, and grasses (Geron et al. 2000; Reichstein et al. 2014; Sindelarova et al. 2014). Monoterpene emissions are often temperature-dependent, making both daytime and nighttime chemistry significant (Staudt and Bertin 1998).

The oxidation of monoterpenes (by oxidants like O_3, NO_3, and OH) can lead to the formation of secondary organic aerosol (SOA) by decreasing the molecule's volatility, enhancing its partitioning to the particle phase (Hallquist et al. 2009). These organic aerosols impact climate, visibility, and human health, as they reflect sunlight back into space and influence cloud properties, which can either cool or warm the atmosphere (Pöschl 2005; Reichstein et al. 2014; Twomey 1977). Anthropogenic emissions transported to forested regions can exacerbate aerosol formation (Carlton et al. 2010; Shrivastava et al. 2019; Xu et al. 2015; Zhang et al. 2018). Elevated NO_x emissions in BVOC-rich regions are likely to produce ozone (O_3), an oxidant and greenhouse gas, and accelerate BVOC oxidation by NO_3 radicals formed from the reaction of O_3 with NO_2. Particulate matter formed from BVOC oxidation can adversely affect human and ecosystem health and visibility, as the small particle size enables penetration deep into the lungs, leading to negative cardiovascular effects (Pope and Dockery 2006).

1.2. Disinfection of Indoor Air: Germicidal UV Light

Since the mid-1800s, scientists have recognized the impact of light on microorganisms, leading to the use of germicidal ultraviolet (GUV), or ultraviolet germicidal irradiation (UVGI),

for airborne microbe inactivation since the early 1900s (Reed, 2010). GUV fixtures have been implemented in hospitals to reduce postoperative infections and curb the spread of diseases like tuberculosis and influenza (Hart, 1960; Wells, 1942; McLean, 1961; Riley et al., 1959). The popularity of GUV declined in the mid-1900s due to advancements in antibiotics and vaccines, coupled with a reduced emphasis on airborne transmission (Reed, 2010; Jimenez et al., 2022).

However, the COVID-19 pandemic has revived interest in GUV for air disinfection, given its effectiveness against SARS-CoV-2 (Ma et al., 2021; Camargo et al., 2022). While 254 nm UV lamps (GUV254) are effective, their human safety limitations necessitate ceiling or ventilation duct placement (Talbot et al., 2002; Nardell et al., 2008). Conversely, studies have demonstrated that 222 nm lamps can safely disinfect whole rooms without harming humans (Buonanno et al., 2017; Narita et al., 2018; Kaidzu et al., 2021). Nevertheless, concerns arise regarding ozone generation by GUV222, which can react with indoor compounds to form harmful pollutants like formaldehyde and $PM_{2.5}$ (Peng et al., 2023; Barber et al., 2023; Link et al., 2023). Given the significant time spent indoors, maintaining good indoor air quality is essential for overall health (Klepeis et al., 2001). Indoor sources such as cleaning products, furniture, and human activity emit volatile organic compounds (VOCs), some of which, like formaldehyde, pose health risks (McDonald et al., 2018; Stönner et al., 2018). Additionally, certain VOCs undergo reactions leading to hazardous products like secondary organic aerosol (SOA), underscoring the importance of assessing air quality in indoor environments.

1.3. Thesis Overview

This thesis presents advances in the understanding of monoterpene oxidation using laboratory studies and ambient measurements. Chapter 2 focuses on the oxidation of Δ-3-carene, a monoterpene that has received less scrutiny compared to the more commonly studied α- and β-

pinene. Although Δ-3-carene emissions account for an estimated 6% of global monoterpene emissions, in regions such as boreal forests, they can constitute as much as 30% of monoterpene emissions (Sindelarova et al., 2014; Spanke et al., 2001). Through experimentation in an environmental chamber, a proton-transfer-reaction time-of-flight mass spectrometer (PTR-TOF-MS) and a chemical-ionization mass spectrometer (CIMS) were employed to identify and quantify gas-phase oxidation products resulting from the Δ-3-carene + NO_3 reaction. A novel approach based on tubing delays to effectively group Vocus parent and fragment ions for analysis is introduced.

Chapter 3 focuses on the gas-phase products resulting from the nitrate radical oxidation of major monoterpenes, investigated in an environmental chamber using trace-gas measurements with a Vocus and iodide CIMS. Tubing delay experiments and voltage scanning methods were employed for quantification and sensitivity analysis. Field studies in Los Angeles further validate the laboratory findings, enhancing our understanding of monoterpene oxidation products' composition and their environmental implications. This research contributes to existing knowledge on particle-phase measurements, SOA yields, and gas-phase monoterpene oxidation, expanding our understanding of atmospheric chemistry and its impacts on air quality and human health.

Chapter 4 evaluates the influence of GUV222 on the chemistry of limonene and its oxidation products. Limonene, a common component of personal care and cleaning products, is prevalent in indoor air and reacts readily with hydroxyl (OH), ozone (O_3), and nitrate (NO_3). Ozone, originating from outdoor air and heightened by GUV222, reacts with limonene and contributes to indoor air pollution. Limonene ozonolysis can generate particulate matter (PM) indoors and produce gas-phase byproducts like formaldehyde and glyoxal. While limonene ozonolysis has been extensively investigated, our focus is on whether GUV222 alters the formation

of these products. The predictive capability of the Regional Atmospheric Chemistry Mechanism (RACM), modified to incorporate SOA formation and wall loss within the chamber, in estimating limonene removal and SOA formation under experimental conditions was assessed. Subsequently, a detailed analysis to ascertain whether the 222 nm light affects the generation of gas-phase and particle-phase oxidation products was conducted.

Investigation of Gas-Phase Products from the NO_3 Radical Oxidation of Δ-3-Carene

Reprinted with permission from Olivia J Jenks, Marla P DeVault, Anna C Ziola, Melissa A Morris, Melinda K Schueneman, Harald Stark, Jose L Jimenez, and Paul J Ziemann. "Investigation of Gas-Phase Products from the NO3 Radical Oxidation of Δ-3-Carene." *ACS Earth and Space Chemistry*, 2023. DOI: 10.1021/acsearthspacechem.3c00020, Copyright 2023.

2.1. Introduction

Biogenic volatile organic compounds (BVOCs) are organic compounds with high vapor pressures that are emitted from vegetation and soils into the atmosphere. BVOCs are primarily composed of isoprene, monoterpenes, sesquiterpenes, and oxygenated compounds, with global emissions of 760 Tg yr^{-1}(Guenther et al. 2012; Sindelarova et al. 2014). Isoprene is the dominant BVOC, and its sources and atmospheric chemistry have been studied extensively (Wennberg et al. 2018). Monoterpenes account for about 15% of global BVOC emissions, with sources including broadleaf tropical forests, shrubs, needleleaf forests, and grasses (Geron et al. 2000; Reichstein et al. 2014; Sindelarova et al. 2014). Monoterpene emissions are often temperature-dependent, not light-dependent, so daytime and nighttime monoterpene chemistry are both important (Staudt and Bertin 1998).

Oxidation of BVOCs can form secondary organic aerosol (SOA) by lowering the volatility of the molecule and thus enhancing partitioning to the particle phase (Hallquist et al. 2009). Organic aerosols impact climate, visibility, and human health (Pöschl 2005; Reichstein et al. 2014). Aerosols reflect sunlight back into space, creating a cooling effect. They also impact the properties of clouds, which can both cool and warm the atmosphere (Twomey 1977). Transport of anthropogenic emissions to forested areas can enhance the formation of aerosols (Carlton et al. 2010; Shrivastava et al. 2019; Xu et al. 2015; Zhang et al. 2018). The chemistry studied here is an example of how anthropogenic emissions of nitrogen oxides (NO_x = NO + NO_2) can affect terpene oxidation through nighttime chemistry. Higher NO_x emissions in BVOC-rich areas will likely

produce O_3, an oxidant and a greenhouse gas. Higher NO_x emissions also enhance the rate of BVOC oxidation by NO_3 radicals that are formed by the reaction of O_3 with NO_2. Particulate matter formed by the oxidation of BVOCs can have adverse effects on human and ecosystem health and on visibility. The average particle diameter of the oxidation products is small enough to penetrate deep into the lungs and can cause negative cardiovascular health effects (Pope and Dockery 2006).

In this study, we focused on the oxidation of Δ-3-carene, a monoterpene that has received less attention than the more commonly studied α- and β-pinene. Emissions of Δ-3-carene are estimated to be 6% of global monoterpene emissions, but in some regions, like boreal forests, Δ-3-carene emissions can be as high as 30% of monoterpene emissions (Sindelarova et al. 2014; Spanke et al. 2001). The differences in structure between α-pinene, a [3.1.1] bicyclic alkene with an internal C═C bond, β-pinene, a [3.1.1] bicyclic alkene with a terminal C═C bond, and Δ-3-carene, a [4.1.0] bicyclic alkene with an internal C═C bond, affect the SOA yield, and studying the differences helps elucidate oxidation mechanisms (Kurtén et al. 2017). The oxidation mechanism and SOA yield for the Δ-3-carene + NO_3 reaction have been published elsewhere, but to our best knowledge, only the gas phase yield of the dicarbonyl has been reported (Dam et al. 2022; Day et al. 2022; DeVault and Ziemann 2021; Draper et al. 2019; Hallquist et al. 1999; Kurtén et al. 2017; Ren et al. 2020).

The focus of this work was on the identification and quantification of gas-phase oxidation products from the Δ-3-carene + NO_3 reaction. The reaction was investigated in an environmental chamber using a proton-transfer-reaction time-of-flight mass spectrometer and a chemical-ionization mass spectrometer (CIMS). We first discuss the reaction mechanism and explain how the iodide CIMS was used to confirm the identity of the expected products. The Vocus

measurements were used to quantify gas-phase product yields, but because the measurements suffered from product-ion fragmentation, we used a new approach based on tubing delays to group Vocus parent and fragment ions together for the analysis. We also used the so-called voltage scanning method to study the sensitivity of the iodide CIMS for these reaction products and compare it with the Vocus measurements (Lopez-Hilfiker et al. 2016). This work focused on the gas-phase products of the Δ-3-carene + NO_3 reaction and complements a previous study that focused on the SOA yields (DeVault and Ziemann 2021).

2.2. Methods

2.2.1. Chemicals

The following chemicals were used: (1s)-(+)-3-carene from Sigma-Aldrich, ultra-high purity N_2 from Airgas, alkyl nitrate standards (2-ethylhexyl nitrate and cyclohexyl nitrate) from Sigma-Aldrich and Fluorochem, and a standard VOC mixture (described above) from Apel-Riemer. N_2O_5 was prepared using the procedure described by Schott and Davidson (1958) and stored at −20 °C.

2.2.2. Chamber Experiments

Experiments were conducted in a ~7.4 m^3 Teflon FEP environmental chamber in the dark, at room temperature (~23 °C) and pressure (~630 torr). Clean air in the chamber is supplied by two AADCO model 737-14A pure air generators (<0.1% RH and <5 ppbv hydrocarbons). Liquid Δ-3-carene was evaporated into the chamber under nitrogen flow using a glass bulb to produce a 500 ppbv concentration. NO_3 radicals were formed by adding 150 ppbv N_2O_5 to the chamber under nitrogen flow, which thermally decomposes to generate NO_2 and NO_3 radicals. A Teflon-coated fan was run for 30 s after each addition to ensure complete mixing in the chamber. The

disappearance of Δ-3-carene and the formation of products were monitored for ~30 min following injection. As the reaction took place in excess of the monoterpene, the majority of NO_3 radicals reacted with Δ-3-carene, and predominantly, first-generation products were formed.

A Vocus proton-transfer-reaction time-of-flight mass spectrometer (Vocus) and an iodide adduct high-resolution time-of-flight CIMS (iodide CIMS) were used to measure Δ-3-carene and oxidation products as a function of time. The Vocus and iodide CIMS were sampled through 1.5 m and 1.0 m 0.635 cm OD (0.397 cm ID) PFA Teflon tubing, respectively, at a flow rate of 2 L min^{-1}.

After ~30 min, the 1.5 m Vocus sampling line was replaced with a 5 m one. Once the tubing reached partitioning equilibrium with the gas-phase products (passivated), it was depassivated by sampling the room air for ~20 min and then re-attached to the chamber(Deming et al. 2019). The longer sampling line was added to enhance the differences in the delay times between different product molecules, which were subsequently used to group together product ions in the Vocus that come from the same reaction products.

2.2.3. Vocus

The Vocus has been described by Krechmer et al. (2018). It consists of a discharge reagent-ion source, which produces H_3O^+ ions; a focusing ion-molecule reactor (FIMR), where analytes are ionized through reaction with H_3O^+ and ions are focused to increase transmission into the mass spectrometer; and a big segmented quadrupole (BSQ), a primary beam ion optics region (PB), and a long time-of-flight (LTOF) mass analyzer for the measurement of the product ions. The water vapor flow rate was 15 sccm, and the applied discharge current was 2.0 mA. The FIMR DC voltage was 500 V, the RF voltage amplitude was 400 V at 1.3 MHz, and the FIMR pressure was 1.5 mbar,

resulting in a reduced electric field (E/N) of ~160 Td. The BSQ RF voltage was 255 V at 2.25 MHz. The Vocus acquired data with a time resolution of 1 s.

Six-point calibrations using a standard mixture of VOCs (methanol, acetonitrile, acetaldehyde, acetone, acrylonitrile, isoprene, 2-butanone, benzene, toluene, m-xylene, 1,2,4-trimethylbenzene, α-pinene, and β-caryophyllene in N_2) were performed immediately following chamber experiments to determine the Vocus sensitivity for these VOCs. The standard mixture was diluted in zero air to mixing ratios of ~30 to ~10 ppbv (except for β-caryophyllene, which is ten times more dilute). Instrument backgrounds were measured independently by overflowing the inlet with zero air. The sensitivity of acetone was ~4000 ncps ppb^{-1}, and the resolution ($m/\Delta m$) was 10,200 at m/z 150. These sensitivities are plotted against the reaction rate coefficients between the VOC and the H_3O^+ ion in Figure 2.1 and shown in Table 2.1.

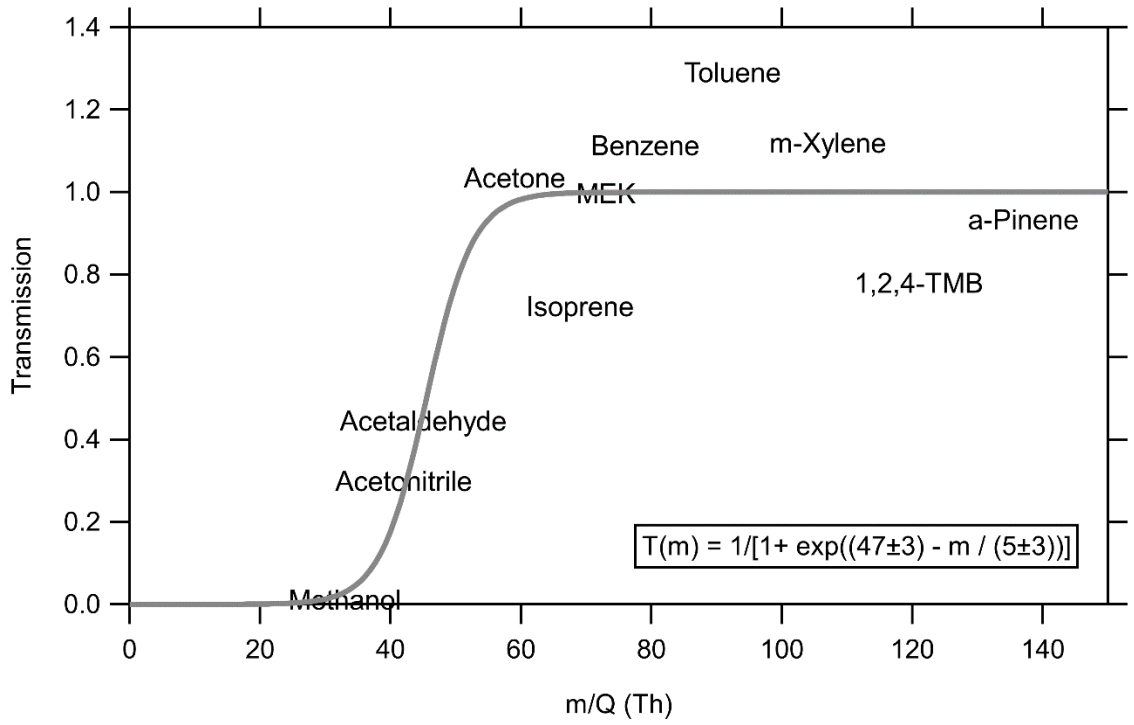

Figure 2.1 Measured sensitivities and calculated proton transfer reaction rate constants for compounds contained in the calibration standard mixture.

Table 2.1 Calculated rates of ion-molecule reaction rates and sensitivities of Vocus calibration standards.

Standard	Formula	k_{ptr} (10^{-9} cm^3 $molecule^{-1}$ s^{-1})(Cappellin et al. 2012)	Vocus Calibration Factor (ncps $ppbv^{-1}$)
Methanol	CH_4O	2.04	17
Acetonitrile	C_2H_3N	3.68	1578
Acetaldehyde	C_2H_4O	2.93	1616
Acrylonitrile	C_3H_3N	Not found	3872
Acetone	C_3H_6O	3.09	4127
MEK	C_4H_8O	2.98	3733
Isoprene	C_5H_8	1.95	1066
Benzene	C_6H_6	1.93	1594
Toluene	C_7H_8	2.07	2247
m-Xylene	C_8H_{10}	2.26	2418
1,2,4-Trimethylbenzene	C_9H_{12}	2.4	1922
α-Pinene	$C_{10}H_{16}$	2.37	2242
Δ-3-Carene	$C_{10}H_{16}$	2.44	2634
β-Caryophyllene	$C_{15}H_{24}$	2.89	423
2-Ethylhyexyl Nitrate	$C_8H_{17}NO_3$	Not found	1494
Cyclohexyl Nitrate	$C_6H_{11}NO_3$	Not found	1637
Acetic acid	$C_2H_4O_2$	1.86	Not included
Formic acid	CH_2O_2	1.66	Not included
Formaldehyde	CH_2O	2.56	Not included

Mixing ratios for neutral products from the NO_3 + Δ-3-carene reaction were calculated by using the average calibration factor of the standard mixture, 2500 ncps $ppbv^{-1}$, with the exception of those VOCs that are contained in the standard mixtures used to calibrate the instrument (e.g., acetone and acetaldehyde). Calibration factors for compounds with m/z < 60 (formic acid, acetaldehyde, and formaldehyde) were adjusted due to mass discrimination in the BSQ using the transmission curve in Figure 2.2.

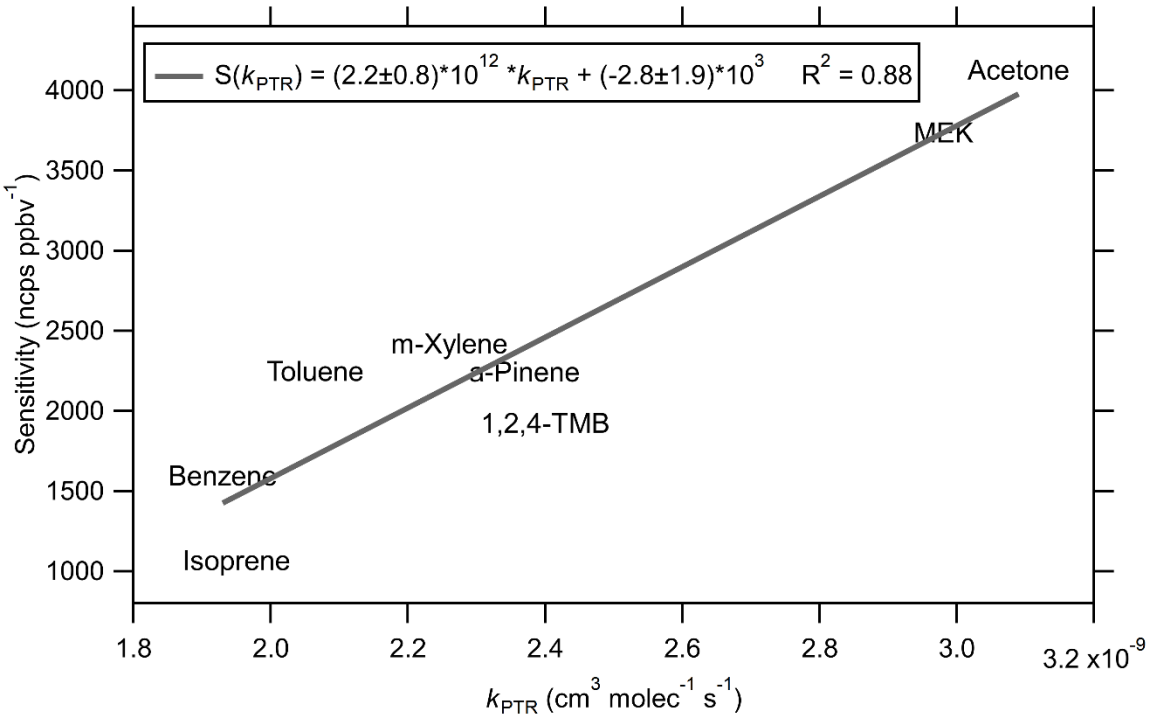

Figure 2.2 Sigmoidal fit to measured transmission of calibration standards in the Vocus assuming a baseline of zero.

2.2.4. Iodide CIMS

The iodide CIMS consists of a radioactive source that produces I^- reagent ions from CH_3I, an ion-molecule reactor (IMR), a small segmented quadrupole (SSQ), a BSQ, a PB region, and an LTOF. The pressure in the IMR was 100 mbar. The iodide CIMS was operated with a time resolution of 1 s, and the mass resolution ($m/\Delta m$) was ~9200 at m/z 275. Calibrations were not performed for this instrument; the data were only used to identify the reaction products. However, any signal variability due to changes in the iodide concentration was accounted for by normalizing product ion signals to the iodide ion signal.

2.2.5. Data Processing

Data processing was performed using Tofware (v3.2.3, www.tofwerk.com/tofware) running in the Igor Pro 8 (Wavemetrics, OR, USA) environment. Mass-to-charge ratio calibration was performed using 8 ions between *m*/*z* 37 and 371 with a resulting accuracy of 4 ppm for the Vocus and between *m*/*z* 127 and 388 with an accuracy of 2 ppm for the iodide CIMS. Peaks were assigned formulas manually. Tofware then allows the calculation of time series by fitting the peak shape to each of the assigned *m*/*z* values from the peak list. Backgrounds were measured in the clean chamber immediately before the addition of Δ-3-carene. Vocus data were normalized to 2×10^6 cps of $(H_2O)_2H^+$, and iodide CIMS data were normalized to 2×10^6 cps of I^-, which is indicated by the units of ncps (normalized counts per second).

2.3. Results and Discussion

2.3.1. Reaction Mechanism

The mechanisms for the reactions between NO_3 and monoterpenes, and specifically Δ-3-carene, have been discussed elsewhere (Claflin and Ziemann 2018; DeVault and Ziemann 2021; Draper et al. 2019; Kurtén et al. 2017). Figure 2.3 illustrates a portion of this mechanism for Δ-3-carene, which is the most relevant for the work described here. More complete mechanisms are shown in the Supporting Information. In the first step, an NO_3 radical adds to either side of the double bond to form a secondary (R1) or tertiary (R2) alkyl radical. This addition occurs at the less-substituted position in a ~60:40 ratio, according to quantum chemical calculations (Kurtén et al. 2017). Oxygen rapidly adds to the alkyl radical to form a peroxy radical, RO_2 (R3 and R4), which then reacts with another RO_2 to form a hydroxy nitrate (HN), carbonyl nitrate (CN), or an alkoxy radical (R5 and R6). The alkoxy radical can undergo a ring-opening reaction, followed by loss of NO_2 to form a dicarbonyl (DC), or a reaction by other pathways to form additional peroxy

radicals (R9 and R10) on the way to more oxygenated products, like a hydroxy carbonyl nitrate (HCN) and a dicarbonyl nitrate (DCN).

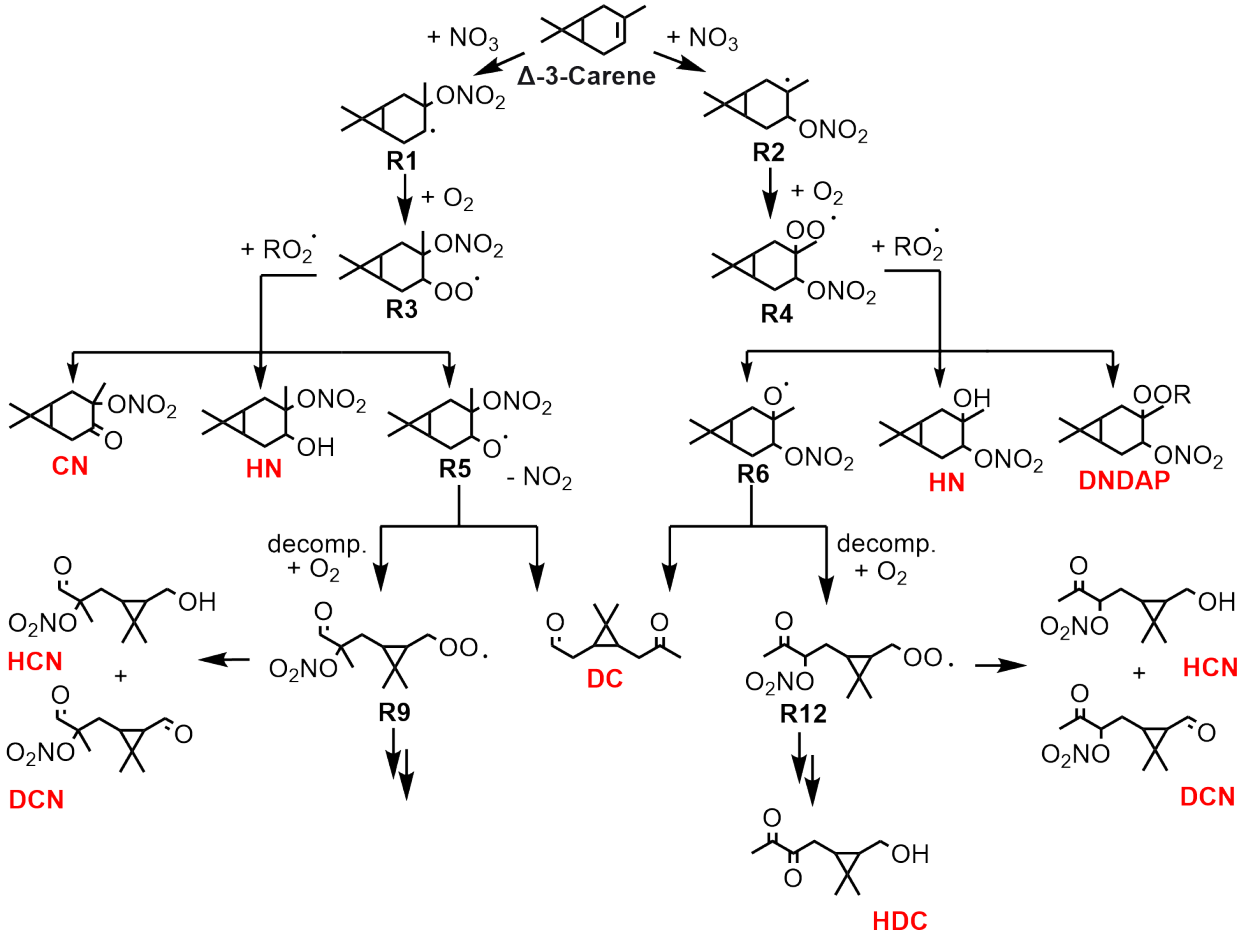

Figure 2.3 Proposed gas-phase reaction mechanism for the oxidation of Δ-3-carene by NO_3 radicals.

In this work, several gas-phase products were observed in addition to the products formed in the mechanism described in DeVault and Ziemann (2021). Figures 2.4-2.6 show a more extensive proposed reaction mechanism that includes these products. The initial β-nitrooxyalkyl radicals (R1 and R2) can also lose NO_2 to form an epoxide (E) (Wängberg et al. 1997). The initial β-nitrooxyalkoxy radicals (R5 and R6) can add NO_2 to form a dinitrate (DN), or DN could be formed from the reaction of N_2O_5 on the walls (Spittler et al. 2006). The formation of C7 products

from NO_3-initiated oxidation of Δ-3-carene by RO bond scission has been described by Draper et al. (2019).

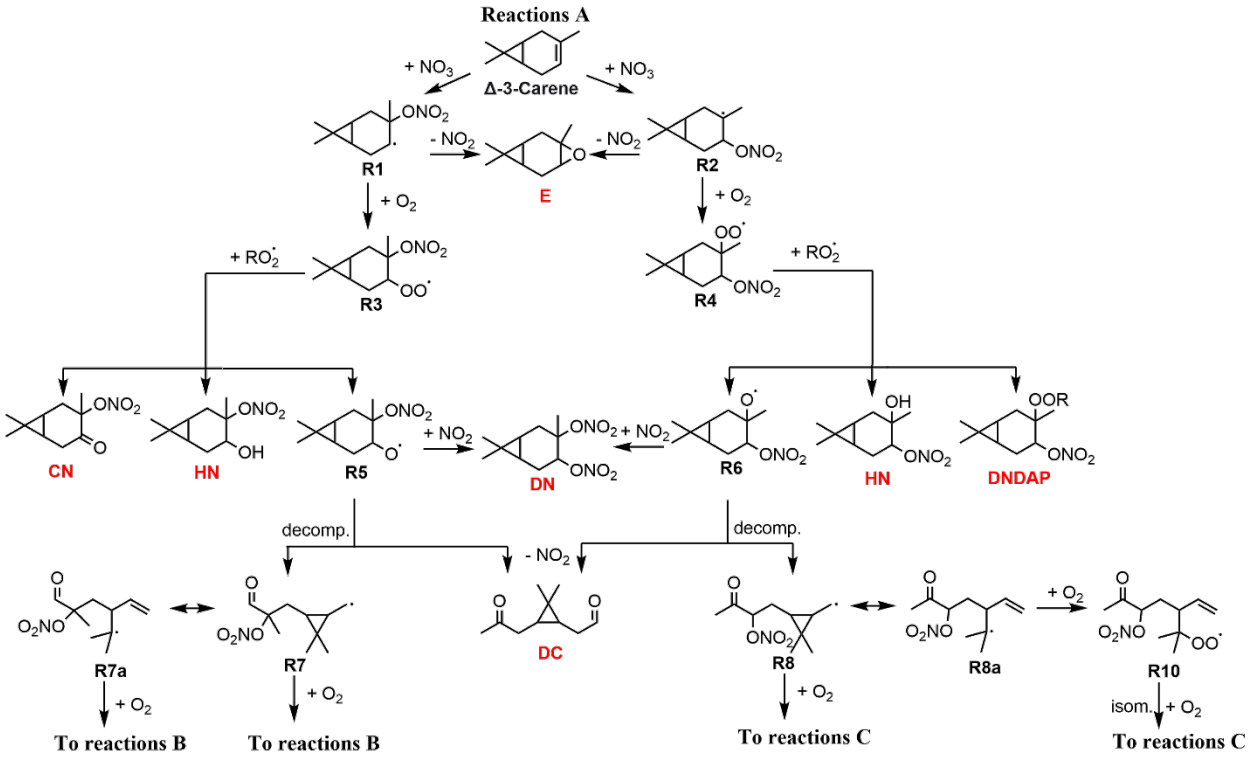

Figure 2.4 Proposed partial gas-phase mechanism (reactions A) for the reaction of NO_3 + Δ-3-carene.

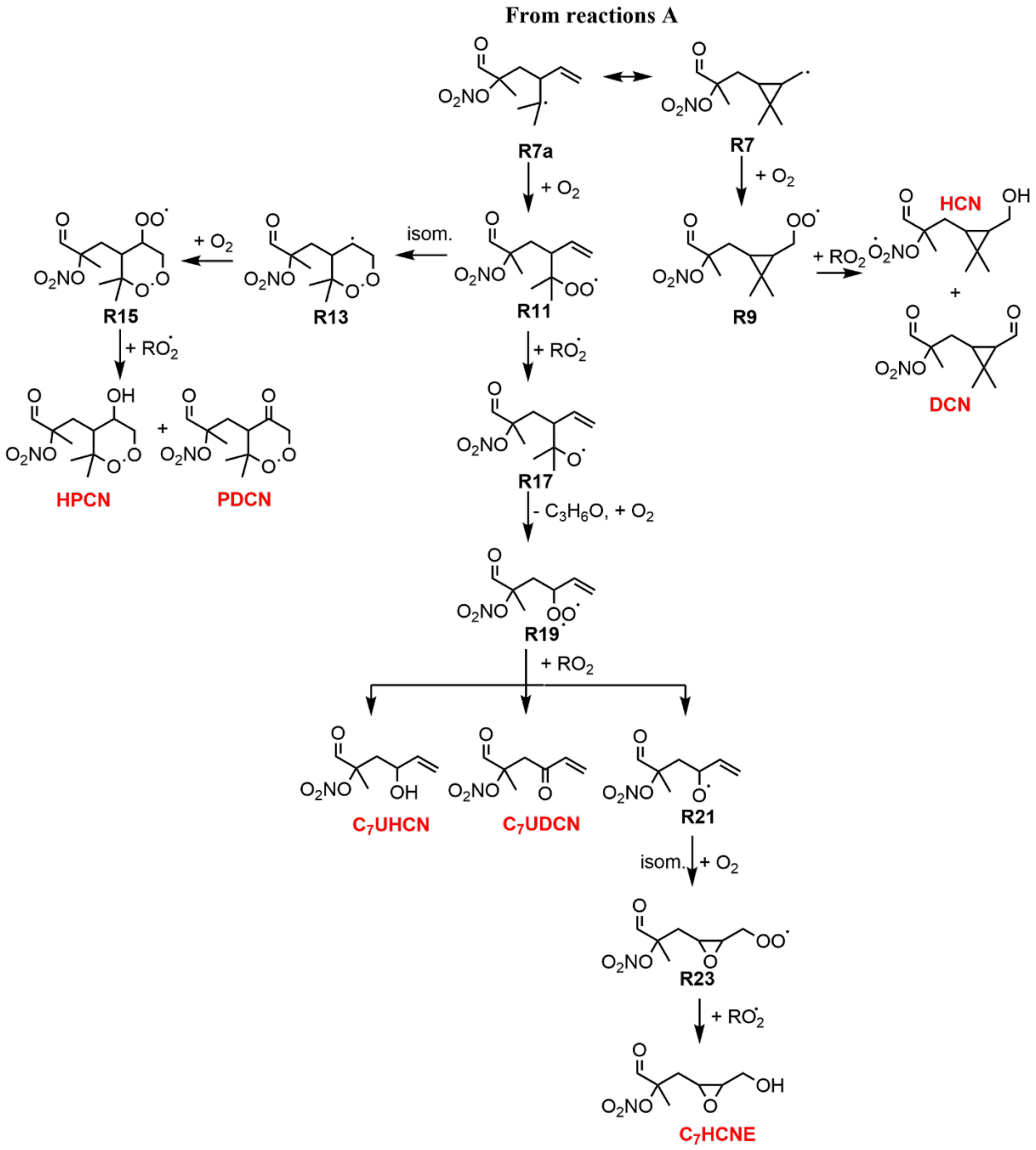

Figure 2.5 Reactions B in the gas-phase mechanism for the NO_3 + Δ-3-carene reactions in Figure 2.4.

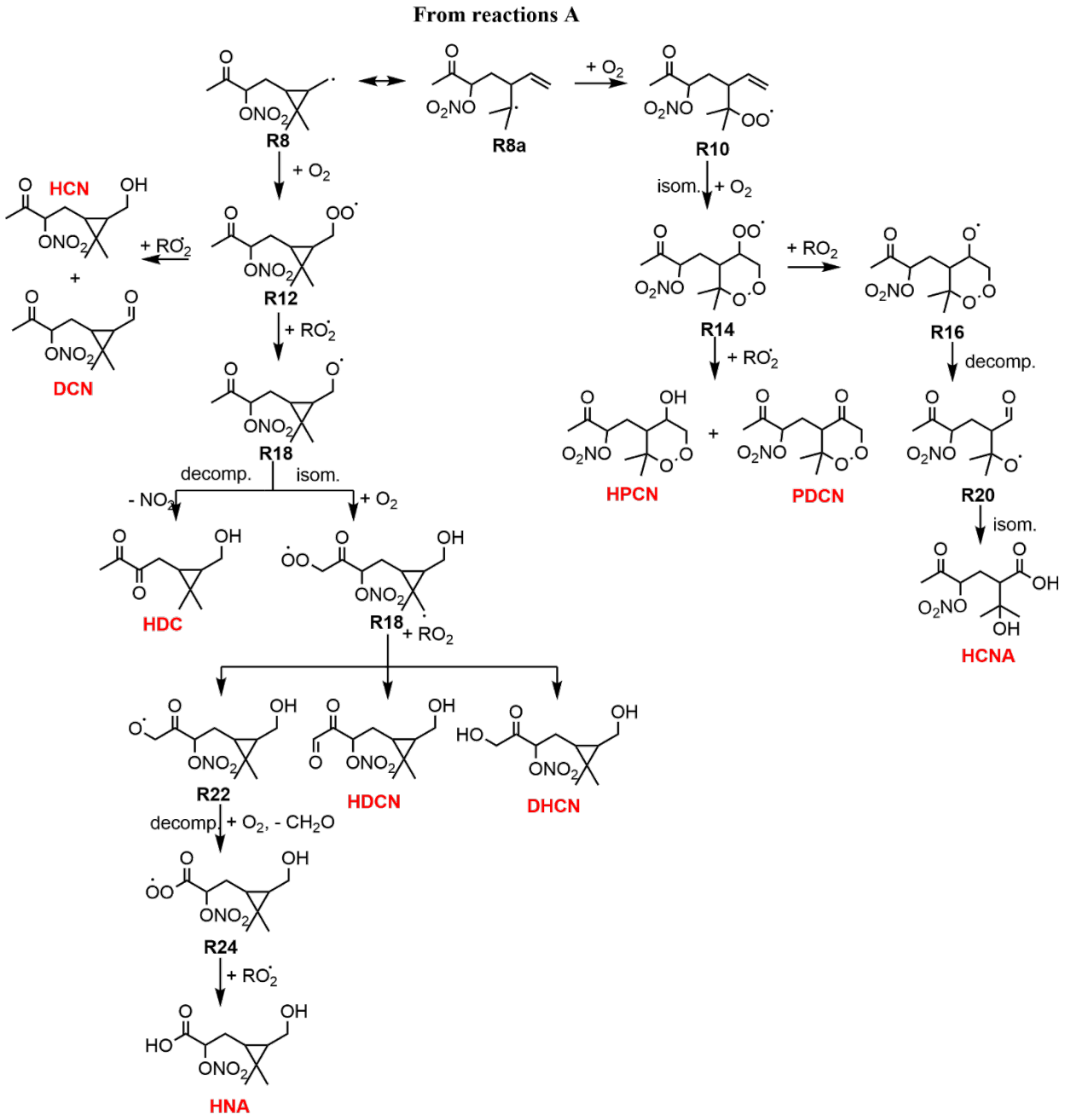

Figure 2.6 Reactions C in the gas-phase mechanism for the NO_3 + Δ-3-carene reactions in Figure 2.4.

2.3.2. Time Series Measurements

Figure 2.7 shows an example time series of Δ-3-carene ($C_{10}H_{17}^+$), N_2O_5, and several gas-phase products detected by the iodide CIMS (panel A) and Vocus (panel B). The reaction was initiated by the addition of N_2O_5 to the chamber, which quickly forms NO_3 through thermal decomposition. The reaction was complete in 5 min after all the NO_3 had reacted, primarily with Δ-3-carene. Iodide CIMS mass spectra show the addition and then depletion of N_2O_5 (and thus NO_3) in a few minutes and the increase of products like HN and HCN (Figure 2.7 A). Vocus mass spectra show the depletion of Δ-3-carene by 49% and the increase of products like DC and HDC (Figure 2.7 B). The slow decay after the reaction is complete is likely due to gas-wall partitioning, which is expected to occur on a timescale of ~10 min (Krechmer et al. 2016).

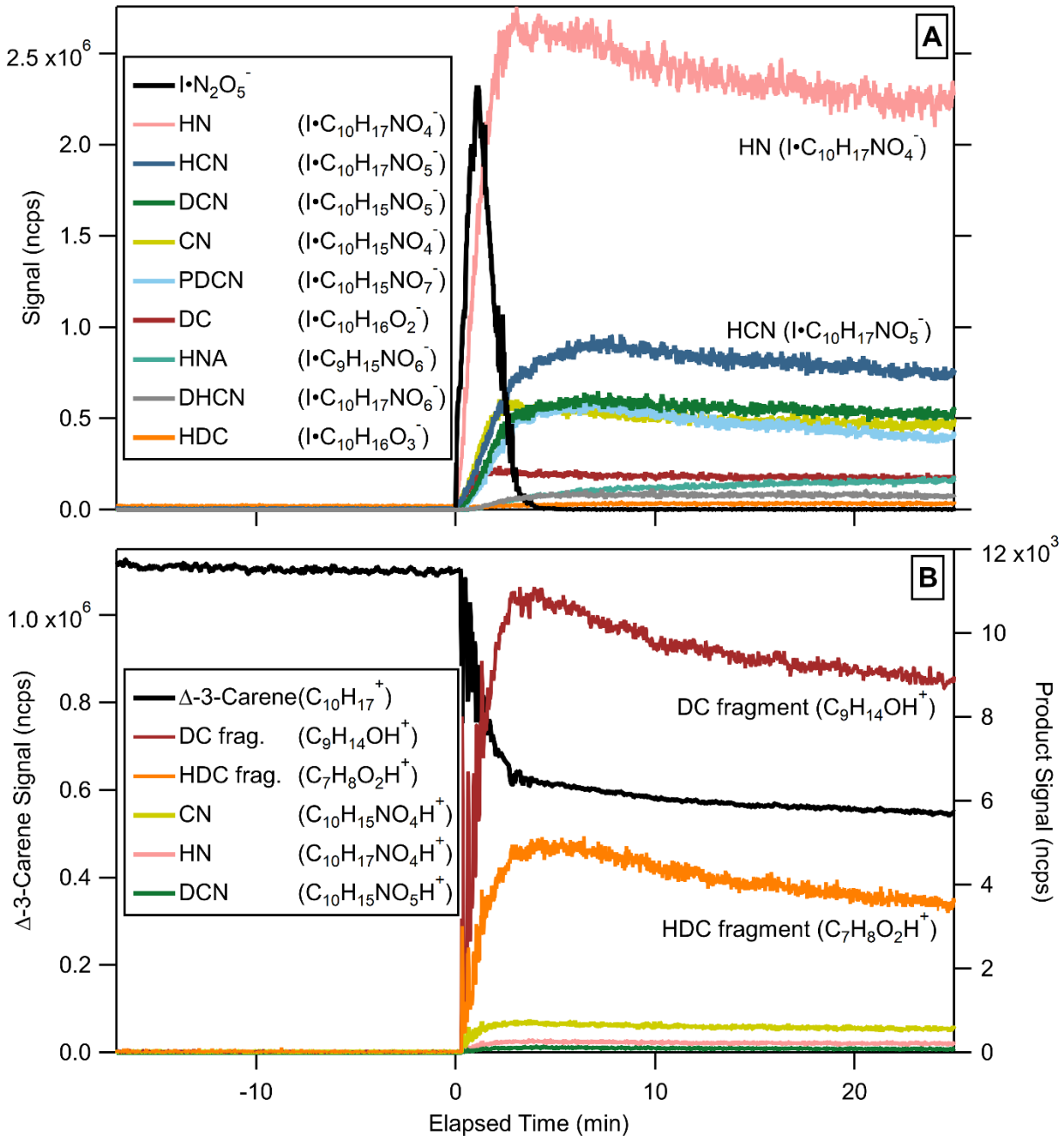

Figure 2.7 Results from an experiment on the reaction between NO_3 radicals and Δ-3-carene obtained by the iodide CIMS (A) and Vocus (B). Product-ion traces are marked by their elemental composition and the neutral reaction product they are attributed to.

A comparison of the time series of the formation of the HN detected by the Vocus and iodide CIMS is shown in Figure 2.8. The two traces correlate very well, but the Vocus signal is lower for a variety of reasons.

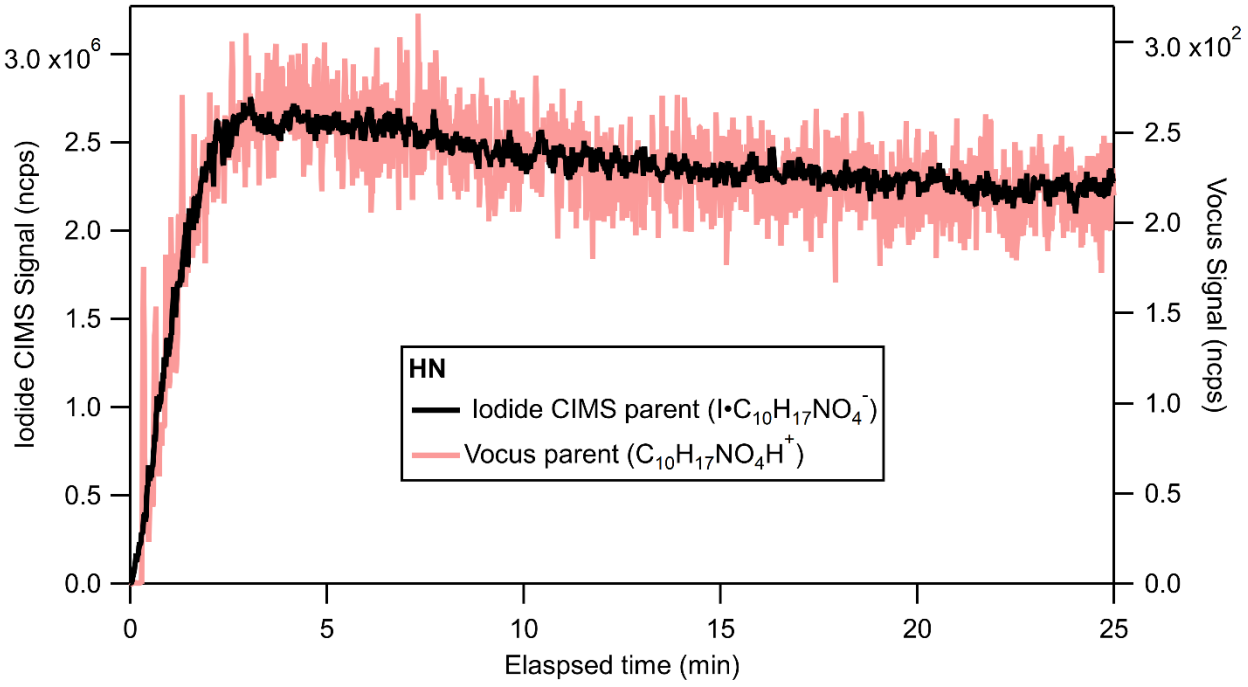

Figure 2.8 Comparison of the time series for the HN parent ion measured by the Vocus and the iodide CIMS. Data were obtained during a chamber experiment after adding N_2O_5 to the environmental chamber containing Δ-3-carene at time zero.

2.3.3. Mass Spectra

The mass spectra of products detected by the iodide CIMS (panel A) and Vocus (panel B) are shown in Figure 2.9. The ions attributed to HN and HCN are highlighted in the iodide CIMS mass spectrum in panel A. The ions attributed to CN and dicarbonyl DC are highlighted in the Vocus mass spectrum in panel B. The signal of the parent ions is much lower than that of some of the ion fragments (formed by the loss of CH_2O and C_3H_6O for DC and the loss of $C_4H_5NO_4$ and $C_2H_3NO_4$ for CN).

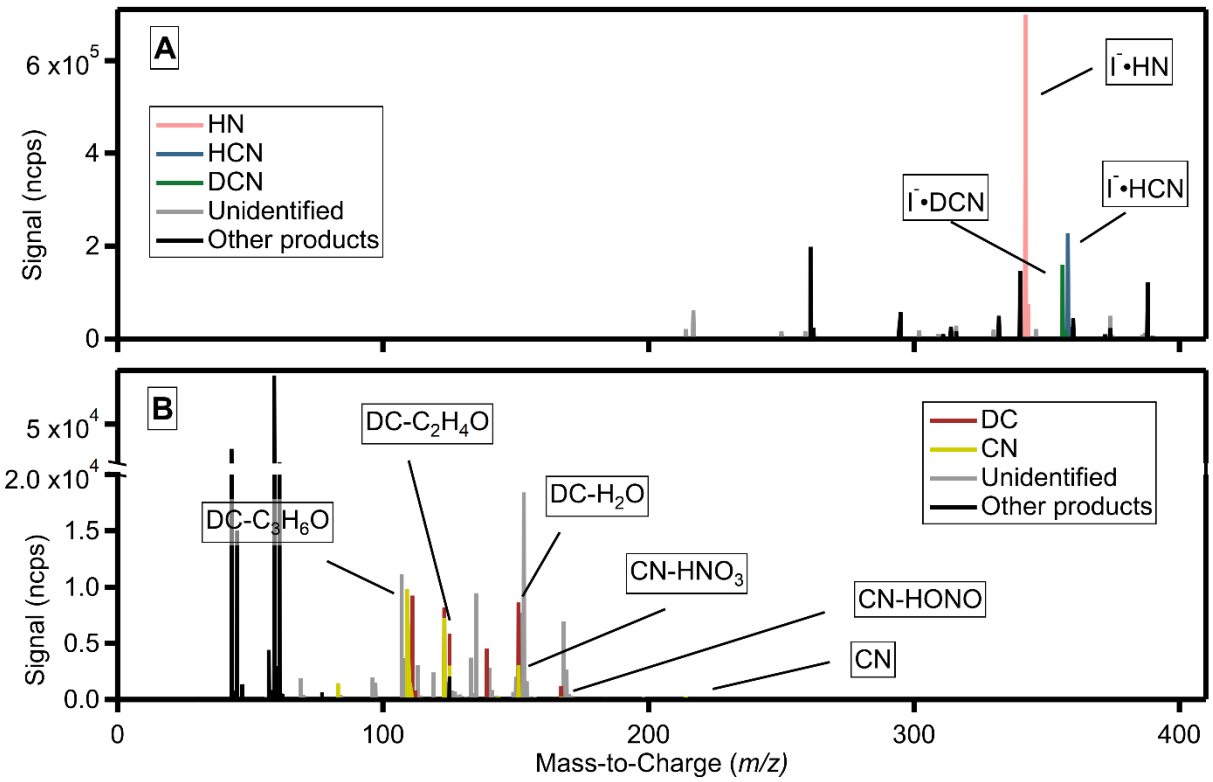

Figure 2.9 Iodide CIMS mass spectrum (A) and Vocus mass spectrum (B) of the products detected from the reaction of Δ-3-carene by NO_3 radicals.

Table 2.2 lists the main ions observed and the neutral reaction products they are attributed to. All products in Table 2.2 were detected with the iodide CIMS except acetone, acetaldehyde, and formaldehyde. All products in 2.2 were detected with the Vocus except HDCN, HNA, DHCN, HPCN, HCNA, DNDAP, and C_7HCNE.

Table 2.2 Proposed gas-phase products formed from the reaction of NO_3 + Δ-3-carene and signals (% of total product signal) detected by the Vocus and iodide CIMS.

Product ID	Formula	Monoisotopic Mass (Da)	Iodide CIMS Detection	Iodide CIMS Signal (% of total)	Vocus Detection (%)		Vocus Signal (% of total)
Dicarbonyl (DC)	$C_{10}H_{16}O_2$	168.115	$I{\bullet}C_{10}H_{16}O_2^-$	1.91	$C_7H_{10}OH^+$ $C_9H_{14}OH^+$ $C_{10}H_{14}OH^+$ $C_{10}H_{14}O_2H^+$ $C_7H_8OH^+$ $C_8H_{12}OH^+$ $C_9H_{15}^+$	19.96 9.78 18.62 2.59 18.79 12.61 17.66	15.99
Carbonyl nitrate (CN)	$C_{10}H_{15}NO_4$	213.100	$I{\bullet}C_{10}H_{15}NO_4^-$	5.18	$C_6H_{11}^+$ $C_8H_{13}^+$ $C_8H_{14}O_2H^+$ $C_{10}H_{14}OH^+$ $C_{10}H_{14}O_2H^+$ $C_8H_{12}OH^+$ $C_{10}H_{15}NO_4H^+$ $C_{10}H_{17}NO_5H^+$ $C_9H_{15}^+$	5.72 38.70 0.76 11.99 1.04 11.90 1.11 0.07 28.70	8.73
Peroxy dicarbonyl nitrate (PDCN)	$C_{10}H_{15}NO_7$	261.085	$I{\bullet}C_{10}H_{15}NO_7^-$	4.32	$C_{10}H_{13}NO_6H^+$ $C_{10}H_{15}NO_7H^+$	70.68 29.32	0.01
Hydroxy dicarbonyl (HDC)	$C_{10}H_{16}O_3$	184.110	$I{\bullet}C_{10}H_{16}O_3^-$	0.15	$C_7H_8O_2H^+$ $C_{10}H_{16}O_3H^+$	94.39 5.61	0.75
Dicarbonyl nitrate (DCN)	$C_{10}H_{15}NO_5$	229.095	$I{\bullet}C_{10}H_{15}NO_5^-$	5.63	$C_{10}H_{14}O_4H^+$ $C_{10}H_{13}NO_5H^+$ $C_{10}H_{15}NO_5H^+$	38.70 22.71 38.58	0.04
Hydroxy nitrate (HN)	$C_{10}H_{17}NO_4$	215.116	$I{\bullet}C_{10}H_{17}NO_4^-$	49.71	$C_{10}H_{18}N_2O_5H^+$ $C_{10}H_{16}OH^+$ $C_{10}H_{17}NO_4H^+$	0.05 99.26 0.69	5.25
Hydroxy carbonyl nitrate (HCN)	$C_{10}H_{17}NO_5$	231.110	$I{\bullet}C_{10}H_{17}NO_5^-$	8.02	Not detected or may overlap with other product(s)		Not detected or may overlap with other product(s)
Hydroxy dicarbonyl nitrate (HDCN)	$C_{10}H_{15}NO_6$	245.090	$I{\bullet}C_{10}H_{15}NO_6^-$	0.33	Not detected		Not detected
Hydroxy nitrate acid (HNA)	$C_9H_{15}NO_6$	233.09	$I{\bullet}C_9H_{15}NO_6^-$	1.58	Not detected		Not detected

Dicarbonyl hydroxy carbonyl nitrate (DHCN)	$C_{10}H_{17}NO_6$	247.106	$I•C_{10}H_{17}NO_6^-$	0.82	Not detected		Not detected
Hydroxy peroxy carbonyl nitrate (HPCN)	$C_{10}H_{17}NO_7$	263.101	$I•C_{10}H_{17}NO_7^-$	0.19	Not detected		Not detected
Hydroxy carbonyl nitrate acid (HCNA)	$C_9H_{15}NO_7$	249.085	$I•C_9H_{15}NO_7^-$	0.06	Not detected		Not detected
Carene epoxide (E)	$C_{10}H_{16}O$	152.120	$NO_3•C_{10}H_{17}NO_3^-$	7.06	$C_{10}H_{16}OH^+$	100	1.14
Dinitrooxy dialkyl peroxide (DNDAP)	$C_{20}H_{32}N_2O_8$	428.216	$I•C_{20}H_{32}N_2O_8^-$	0.09	Not detected		Not detected
Dinitrate (DN)	$C_{10}H_{16}N_2O_6$	260.101	$I•C_{10}H_{16}N_2O_6^-$	0.46	$C_{10}H_{16}N_2O_6H^+$	100	<0.01
C7 Hydroxy carbonyl nitrate epoxide (C_7HCNE)	$C_7H_{11}NO_6$	205.059	$I•C_7H_{11}NO_6^-$	1.85	Not detected		Not detected
C7 Unsaturated dicarbonyl nitrate (C_7UDCN)	$C_7H_9NO_5$	187.048	$I•C_7H_9NO_5^-$	0.94	May overlap with other product(s)		May overlap with other product(s)
C7 Unsaturated hydroxy carbonyl nitrate (C^7UHCN)	$C_7H_{11}NO_5$	189.064	$I•C_7H_{11}NO_5^-$	0.60	$C_7H_9NO_4H^+$ $C_7H_9NO_5H^+$ $C_7H_{11}NO_5H^+$	54.72 29.93 15.35	0.02
Acetone	C_3H_6O	58.0419	Not Detected	Not Detected	$C_3H_4OH^+$ $C_3H_6OH^+$ $C_3H_8O_2H^+$	4.80 94.53 0.67	31.78
Acetic acid	$C_2H_4O_2$	60.0211	$I•C_2H_4O_2^-$	<0.01	$C_2H_2OH^+$ $C_2H_4O_2H^+$	59.69 40.31	17.90
Formic acid	CH_2O_2	46.005	$I•CH_2O_2^-$	0.15	$CH_4O_3H^+$ $CH_2O_2H^+$	3.77 96.23	0.49
Acetaldehyde	C_2H_4O	44.0262	Not Detected	Not Detected	$C_2H_4OH^+$ $C_2H_6O_2H^+$	98.95 1.05	5.24
Formaldehyde	CH_2O	30.0106	Not Detected	Not Detected	CH_2OH^+	100	0.03
Unidentified				11.39			12.69

The Vocus and iodide CIMS both have strengths and limitations in these experiments. Only the Vocus detects Δ-3-carene, while only the iodide CIMS detects N_2O_5. The Vocus is the more easily quantifiable instrument: the proton-transfer reactions that ionize the sample molecules are collision-limited, and instrument sensitivities can be estimated even in the absence of calibration standards (Cappellin et al. 2012; Sekimoto et al. 2017). In contrast, the iodide CIMS has vastly different sensitivities for different compounds, making the quantification of products very uncertain without authentic calibration standards (Iyer et al. 2016). Fragmentation of product ions is mostly absent in the iodide CIMS but common in the Vocus, typically occurring for compounds containing alcohol, aldehyde, acid, ester, and nitrate groups. This complicates the attribution of the signals to most oxidation products and needs to be accounted for in the quantification of product yields since calculated sensitivities require the total product ion signals, including all fragments (Pagonis et al. 2019). As described in the next section, Vocus parent and fragment ions were grouped based on their inlet delay times and elemental composition and used to calculate yields.

2.3.4. Tubing Delay Experiments

A novel aspect of this work is the use of tubing delay experiments to identify products, and group parent and fragment ions for quantification. Figure 2.10 A shows an example of a tubing delay experiment, in which the longer (5 m) sampling line was abruptly switched from the environmental chamber to room air (with much lower levels of these compounds than the chamber).

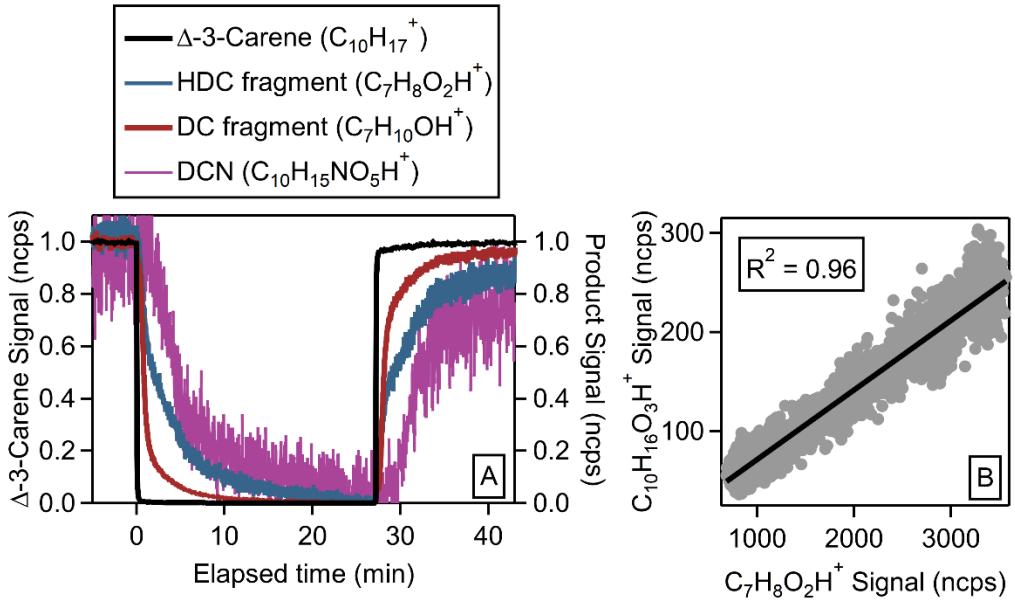

Figure 2.10 Vocus signals of Δ-3-carene and oxidation products when the sampling line is abruptly switched from the environmental chamber to room air and then back to the chamber. (B) Scatter plot illustrating the correlation of two ions, HDC ($C_{10}H_{16}O_3H^+$) and an HDC fragment ion ($C_7H_8O_2H^+$). Data were obtained during a delay-time experiment and were used to group parent and fragment ions from the same neutral products.

Because gas-wall partitioning in the Teflon tubing separates products by their effective saturation concentration (C*), the corresponding Vocus signal either changes very quickly (e.g., Δ-3-carene) or slowly (e.g., DCN) depending on the volatility of the molecule (Liu et al. 2019; Pagonis et al. 2017). Based on the similarity in tubing delay times and consistent ion elemental compositions, parent and fragment ions from the same neutral reaction products were grouped (Table 2.2), and then, the sums of the signals were used to determine product yields. This grouping was done in the following steps:

1. Ions were grouped based on tubing delay time and profile.
2. Multivariate regression analysis was performed for ions with two distinct delay profiles.
3. Fragment assignments were evaluated based on the structure of the parent ion.

An example of this method is shown in Figure 2.11. In Figure 2.11 A-C the CN fragment ion (left axis) is plotted against the CN parent ion (bottom axis). Since the correlation is high, these fragments are assigned to CN. In Figure 2.11 4 D-H a multivariate fit of a fragment (left axis) is plotted against the fragment. Since the fits are good, we conclude that those fragments have contributions from the parent ions listed. We then evaluated the eight fragment ions (Table 2.10 based on the structure on CN. As discussed below, we expect loss of HNO_3, HONO, and alkyl nitrates from nitrate-containing products.

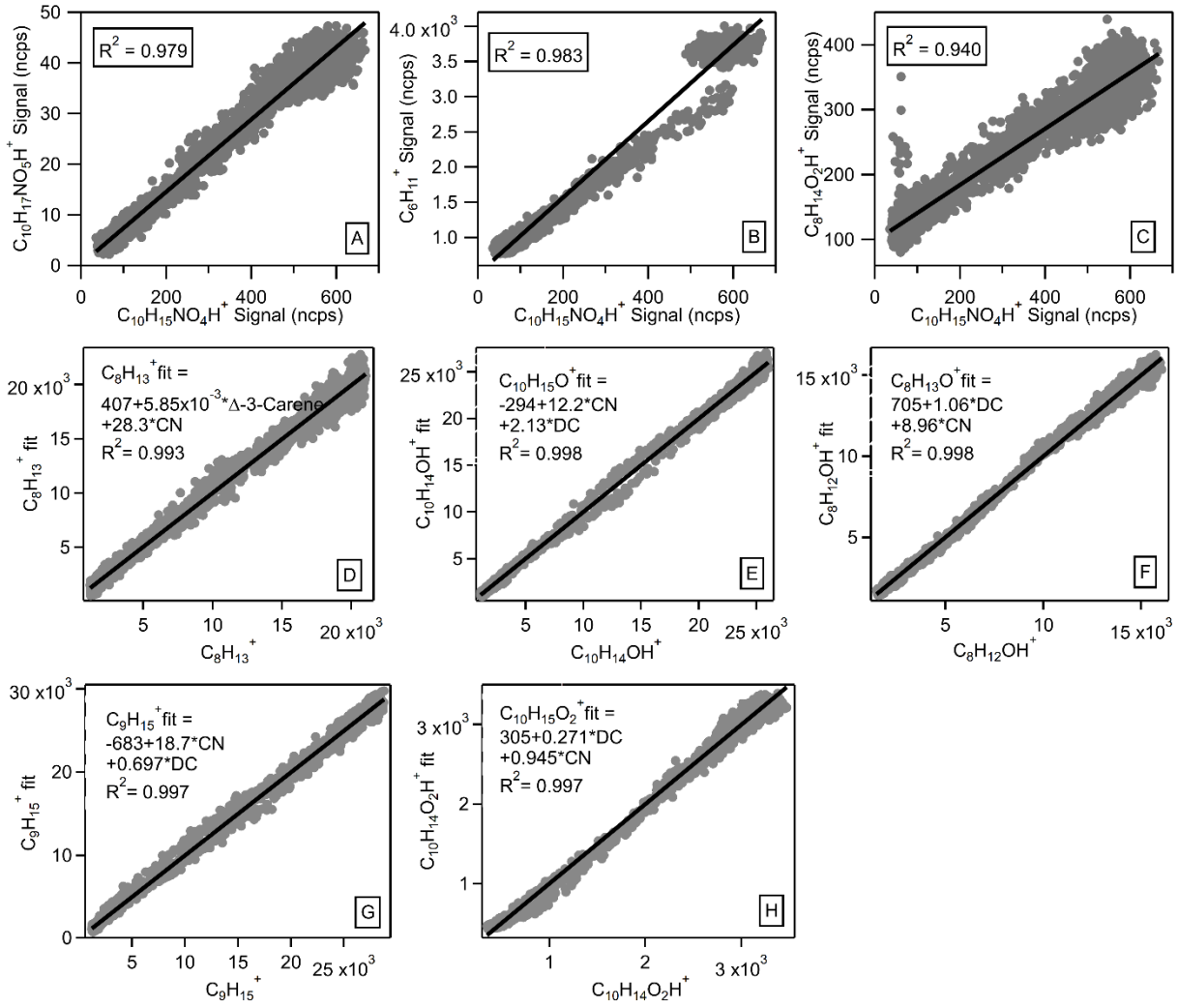

Figure 2.11 Scatter plots of CN fragment and parent ions measured with the Vocus (A-C). Scatter plots of CN fragment ions (with contributions from other ions) measured with the Vocus and their linear least-squares fits (D-H). (D) $C_8H_{13}^+$ with contributions from Δ-3-carene and CN. (E) $C_{10}H_{15}O^+$ with contributions from HN and DC. (F) $C_8H_{13}O^+$ with contributions from DC and CN. (G) $C_9H_{15}^+$ with contributions from CN and DC. (H) $C_{10}H_{15}O_2^+$ with contributions from DC and CN.

Table 2.3 Ions assigned to CN and the fragmentation loss from CN.

Vocus Detection	Fragmentation Loss
$C_{10}H_{15}NO_4H^+$ (Parent)	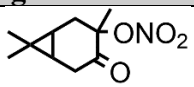
$C_{10}H_{17}NO_5H^+$	$+H_2O$
$C_{10}H_{14}O_2H^+$	-HONO
$C_{10}H_{14}OH^+$	$-HNO_3$
$C_8H_{14}O_2H^+$	$-C_2HNO_2$
$C_8H_{12}OH^+$	$-C_2H_3NO_3$
$C_9H_{15}^+$	$-CHNO_4$
$C_8H_{13}^+$	$-C_2H_3NO_4$
$C_6H_{11}^+$	$-C_4H_5NO_4$

Figure 2.10 B shows that the time series of $C_{10}H_{16}O_3H^+$ (HDC) and $C_7H_8O_2H^+$ (HDC–C_3H_8O) are highly correlated. In addition, the C* values for the products were estimated using SIMPOL.1 and used to calculate delay times using the tubing model from Pagonis et al. (2017; Pankow and Asher 2008). The measured delay times for the oxidation products were compared to modeled delay times, and the results are shown in Figure 2.12. It should be noted that saturation vapor pressure estimation methods like SIMPOL.1 may not perform as well for compounds containing nitrate groups due to limited experimental data (Bilde et al. 2015).

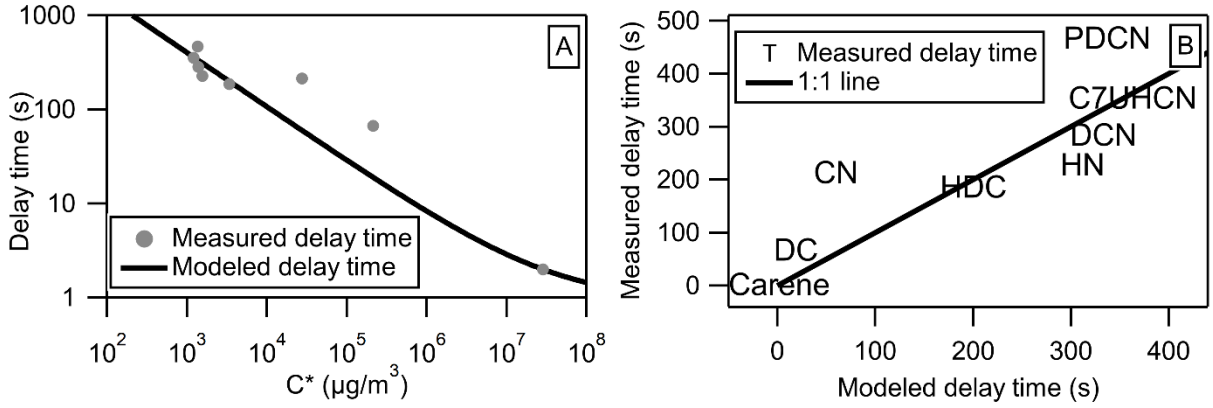

Figure 2.12 Tubing delay times for NO_3 + Δ-3-carene reaction products measured with the Vocus and modeled using the Pagonis et al. (2017) model, plotted vs. C* of each molecule as estimated from SIMPOL.1 (Pankow and Asher 2008). (B) Measured vs modeled delay times.

Some fragment ions clearly had contributions from multiple parent ions. An example is shown in Figure 2.13 for the ion $C_8H_{13}^+$. In Figure 2.13 A, it can be seen that this ion showed a fast decay for the first ~10 s, which correlated well with the decay of Δ-3-carene. The decay in $C_8H_{13}^+$ then slowed considerably and correlated much better with the decay of CN. Multivariate regression analysis was used to assign fragment ions with contributions from two parent ions quantitatively to each channel, as shown in Figure 2.13 B.

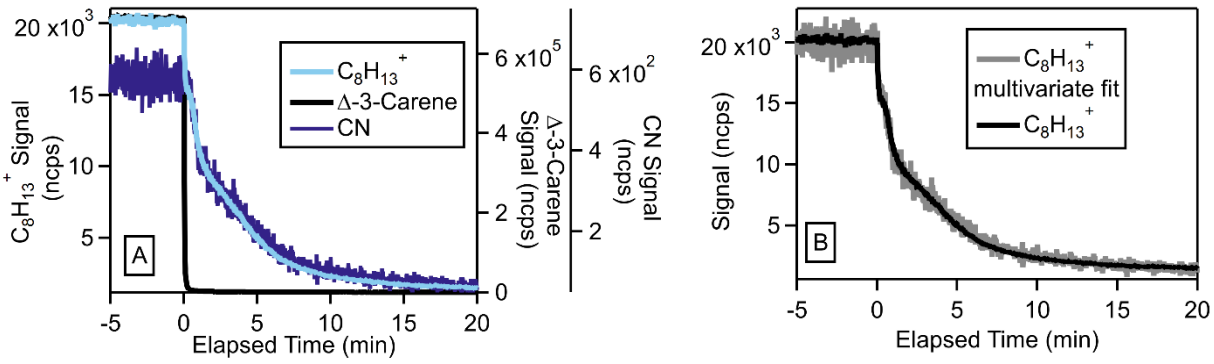

Figure 2.13 (A) Vocus signals measured for Δ-3-carene, CN, and $C_8H_{13}^+$ when the sampling line was abruptly switched from the environmental chamber to room air, showing the correlation of $C_8H_{13}^+$ with Δ-3-carene in the first ~10 s and CN after. (B) Multivariate fit for $C_8H_{13}^+$ and Vocus signal measured for $C_8H_{13}^+$.

By grouping the signals that show similar delay times, we identified 87% of the total ion signal attributed to reaction products by the Vocus: 44% as parent ions and 43% as fragments. For comparison, 89% of the iodide CIMS product ion signal was identified. The average measured delay times of fragment and parent ions and the calculated C* values are listed in Table 2.4 and shown in Figure 2.14.

Table 2.4 The average delay time in seconds for each product and its fragment ions detected by the Vocus.

Product ID	Formula	C* ($\mu g/m^3$)*	Vocus Detection	Fragmentation Loss	Average Vocus delay time (s)
Dicarbonyl (DC)	$C_{10}H_{16}O_2$	$2.13x10^5$	$C_7H_{10}OH^+$	$-C_3H_6O$	67
			$C_9H_{14}OH^+$	$-CH_2O$	
			$C_{10}H_{14}OH^+$	$-H_2O$	
			$C_{10}H_{14}O_2H^+$	$-H_2$	
			$C_7H_8OH^+$	$-C_3H_8O$	
			$C_8H_{12}OH^+$	$-C_2H_4O$	
			$C_9H_{15}^+$	$-CH_2O_2$	
Carbonyl nitrate (CN)	$C_{10}H_{15}NO_4$	$2.75x10^4$	$C_6H_{11}^+$	$-C_4H_5NO_4$	213
			$C_8H_{13}^+$	$-C_2H_3NO_4$	
			$C_8H_{14}O_2H^+$	$-C_2HNO_2$	
			$C_8H_{12}OH^+$	$-C_2H_3NO_3$	
			$C_9H_{15}^+$	$-CHNO_4$	
			$C_{10}H_{14}OH^+$	$-HNO_3$	
			$C_{10}H_{14}O_2H^+$	-HONO	
			$C_{10}H_{15}NO_4H^+$	Parent	
			$C_{10}H_{17}NO_5H^+$	$+H_2O$	
Hydroxy dicarbonyl (HDC)	$C_{10}H_{16}O_3$	$3.37x10^3$	$C_7H_8O_2H^+$	$-C_3H_8O$	186
			$C_{10}H_{16}O_3H^+$	Parent	
C7 Unsaturated hydroxy carbonyl nitrate (C_7UHCN)	$C_7H_{11}NO_5$	$2.93x10^3$	$C_7H_9NO_4H^+$	$-H_2O$	354
			$C_7H_9NO_5H^+$	$-H_2$	
			$C_7H_{11}NO_5H^+$	Parent	
Dicarbonyl nitrate (DCN)	$C_{10}H_{15}NO_5$	$1.93x10^3$	$C_{10}H_{14}O_4H^+$	-HNO	284
			$C_{10}H_{13}NO_5H^+$	$-H_2O$	
			$C_{10}H_{15}NO_5H^+$	Parent	
Hydroxy nitrate (HN)	$C_{10}H_{17}NO_4$	$1.56x10^3$	$C_{10}H_{18}N_2O_5H^+$	+HNO	228
			$C_{10}H_{17}NO_4H^+$	Parent	
Peroxy dicarbonyl nitrate (PDCN)	$C_{10}H_{15}NO_7$	$1.36x10^3$	$C_{10}H_{13}NO_6H^+$	$-H_2O$	467
			$C_{10}H_{15}NO_7H^+$	Parent	
Acetone	C_3H_6O	$3.03x10^9$	$C_3H_4OH^+$	$-H_2$	268
			$C_3H_6OH^+$	Parent	
			$C_3H_8O_2H^+$	$+H_2O$	
Acetic acid	$C_2H_4O_2$	$2.12x10^8$	$C_2H_2OH^+$	$-H_2O$	289
			$C_2H_4O_2H^+$	Parent	
Formic acid	CH_2O_2	$5.75x10^8$	$CH_2O_2H^+$	Parent	187
			$CH_4O_3H^+$	$+H_2O$	
Acetaldehyde	C_2H_4O	$1.21x10^{10}$	$C_2H_4OH^+$	Parent	393
			$C_2H_6O_2H^+$	$+H_2O$	
Formaldehyde	CH_2O	$2.02x10^7$	CH_2OH^+	Parent	286

* Product saturation concentrations (C*) are calculated using the SIMPOL.1 method.

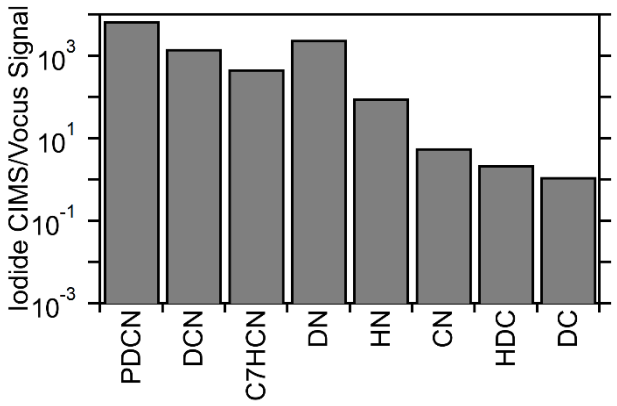

Figure 2.14 Delay time distribution of remaining Δ-3-carene after oxidation and oxidation products measured by the Vocus.

Some common fragmentation patterns were observed in the Vocus mass spectra:

- For compounds that contain an aldehyde group (DC, DCN, PDCN, and C_7UHCN), we observed the loss of H_2O, as is very common for aldehydes in proton-transfer reactions (Pagonis et al. 2019). CH_2O (formaldehyde) and C_2H_4O (acetaldehyde) were lost from DC, which makes sense given its molecular structure.
- For compounds with an alcohol group (HN, HDC, and C_7UHCN), we expected a loss of H_2O and alcohols (Pagonis et al. 2019). We observed loss of H_2O for C_7UHCN, but the fragments formed by loss of H_2O from HN and HDC ions may have contributions from other molecules and were unable to be assigned uniquely to HN and HDC. Based on the structures of these products, we also expected to see loss of neutral CH_4O (methanol) from HDC and loss of neutral C_3H_6O (propenol) from C_7UHCN, but the ionized fragments may have contributions from other product ions and could not be assigned uniquely to HDC and C_7UHCN.

- For compounds with a nitrate group (CN, HN, DN, DCN, PDCN, and C_7UHCN), we expected loss of HNO_3, HONO, and alkyl nitrates (Duncianu et al. 2017). We observed loss of HNO_3 for CN and HN but could not definitively determine if DN, DCN, PDCN, and C_7UHCN lost HNO_3. We saw the loss of HONO from CN but could not definitively determine if HN, DCN, DN, C_7UHCN, and PDCN lost HONO.
- For compounds with a ketone group (DC, CN, PDCN, HDC, and DCN), we did not expect fragmentation, but we observed loss of C_3H_6O (acetone) from DC. Other fragments observed are included in Table 2.2.

2.3.5. Product Yields

Estimated product concentrations and molar yields from the reaction of Δ-3-carene with NO_3 radicals were calculated by summing the parent and fragment ion signals, applying the relative *m*/*z* transmission values (shown in Figure 2.1) for each product measured by the Vocus, and converting to a mixing ratio using a calibration factor of 2500 ncps $ppbv^{-1}$. Vocus calibration factors and the results are shown in Table 2.5.

Table 2.5 The calibration factors used for products detected by the Vocus and iodide CIMS.[†]

Product	Formula	Vocus Calibration Factor (cps ppb^{-1})	Iodide CIMS Calibration Factor (cps ppt^{-1})[‡]	Concentration (ppb)	Molar Yield (%)
Dicarbonyl (DC)	$C_{10}H_{16}O_2$	$2.5x10^3$	$2.9x10^0$	18.534 ± 9.267	7.57 ± 3.79
Carbonyl nitrate (CN)	$C_{10}H_{15}NO_4$	$2.5x10^3$	$1.4x10^1$	10.112 ± 5.056	4.13 ± 2.07
Peroxy dicarbonyl nitrate (PDCN)	$C_{10}H_{15}NO_7$	$2.5x10^3$	$1.7x10^4$	0.007 ± 0.003	<0.01 ± 0.01
Hydroxy dicarbonyl (HDC)	$C_{10}H_{16}O_3$	$2.5x10^3$	$5.7x10^0$	0.865 ± 0.433	0.35 ± 0.18
Dicarbonyl nitrate (DCN)	$C_{10}H_{15}NO_5$	$2.5x10^3$	$3.7x10^3$	0.043 ± 0.022	0.02 ± 0.01
Hydroxy nitrate (HN)	$C_{10}H_{17}NO_4$	$2.5x10^3$	$2.3x10^2$	6.081 ± 3.041	2.48 ± 1.24
Epoxide (E)	$C_{10}H_{16}O$	$2.5x10^3$	$7.5x10^0$	1.325 ± 0.663	0.54 ± 0.27
Dinitrate (DN)	$C_{10}H_{16}N_2O_6$	$2.5x10^3$	$6.1x10^3$	0.002 ± 0.001	<0.01 ± 0.01
C_7 Unsaturated hydroxy carbonyl nitrate (C_7UHCN)	$C_7H_{11}NO_5$	$2.5x10^3$	$1.2x10^3$	0.024 ± 0.012	0.01 ± 0.01
Acetone	C_3H_6O	$4.1x10^3$	Not detected	22.287± 0.074	9.10 ± 0.03[§]
Acetic acid	$C_2H_4O_2$	$1.5x10^3$	$3.0x10^{-3}$	34.836 ± 17.418	14.22 ± 7.11[**]

[†] Uncertainty for calibrated species is propagated from the measurement uncertainty and the calibration factor uncertainty. All other species are assumed to have a 50% uncertainty.
[‡] Product concentrations calculated from the Vocus sensitivities were used to calculate the iodide CIMS calibration factors.
[§] The calibration factor from standards was used.
[**] The proton-transfer reaction rate coefficient k_{ptr} was used to calculate the calibration factor, and was adjusted due to mass discrimination.

Formic acid	CH_2O_2	$6.2x10^2$	$1.9x10^0$	2.282 ± 1.141	0.93 ± 0.47[††]
Acetaldehyde	C_2H_4O	$1.6x10^3$	Not detected	9.388± 0.615	3.83 ± 0.25[‡‡]
Formaldehyde	CH_2O	$6.5x10^1$	Not detected	1.551 ± 0.776	0.63 ± 0.32[†]
Unidentified gas phase products				14.708 ± 7.354	6.00 ± 3.00
Total gas-phase organic nitrate products	$C_xH_yN_iO_z$			16.569 ± 8.285	6.76 ± 3.38
Total gas phase products				122.045 ± 45.856	49.82 ± 18.77
SOA(DeVault and Ziemann 2021)					34 ± 1
Total (SOA + gas-phase)					84± 20

The total molar yield of gas phase products was 50 ± 19%, which combined with the SOA molar yield of 34 ± 1% measured by DeVault and Ziemann (2021) gives a total product yield of 84 ± 20%. The product with the largest gas-phase molar yield is acetic acid at 14%, followed by acetone at 9%, DC at 8%, CN at 4%, acetaldehyde at 4%, HN at 2%, and the remaining products at <1%. The 8% yield of DC is higher than the 2–3% value previously reported, the reasons for that are not known (Hallquist et al. 1999). The total gas-phase organic nitrate yield is 7% and is mostly CN (4%) and HN (2%). The molar yield of organic nitrates in SOA was estimated to be 34% based on bulk analysis of nitrate groups (DeVault and Ziemann 2021). The differences in structure between Δ-3-carene and α-pinene have been shown to lead to different yields of gas-phase products, organic nitrates, and SOA, which can be explained by the preference for bond

[††] The proton-transfer reaction rate coefficient k_{ptr} was used to calculate the calibration factor, and was adjusted due to mass discrimination.
[‡‡] The calibration factor from standards was used.

scission of the nitroxy alkoxy radicals to form DC or less volatile multifunctional organic nitrates (Day et al. 2022; Kurtén et al. 2017). Calibration factors for the products detected by the iodide CIMS were calculated from the Vocus-derived product concentrations. These values are shown in Table 2.5, and many fall within the range of sensitivities reported by Bi et al. (2021).

2.3.6. Voltage Scanning

A strength of the iodide CIMS is that most reaction products are detected with little or no fragmentation. This aids greatly in the evaluation of reaction mechanisms. However, a limitation of this technique is that the sensitivity varies by orders of magnitude across different analytes, making the method more labor-intensive and uncertain for quantifying product yields. Lopez-Hilfiker et al. (2016) described a method that employs "voltage scanning" to estimate the bond strengths of iodide-product adducts and then use those strengths to estimate instrument sensitivities (based on calibrations of that relationship). The method is based on the principle that as the voltage difference between the skimmer and the BSQ increases, the collision energy between adduct ions and gas-phase neutrals increases, and the adducts can subsequently dissociate (into I^- and a neutral molecule that therefore goes undetected) according to the strength of the adduct binding energy. We used this method here to study the reaction products and observed a clear trend in which the less functionalized compounds, such as DC, CN, and HN, dissociated at lower voltages (collision energies) than the more functionalized compounds, such as DHCN (Figure 2.15).

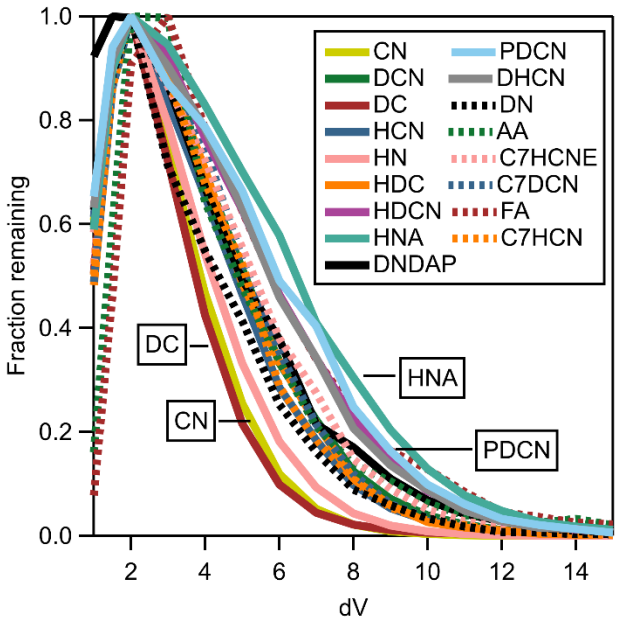

Figure 2.15 Results from a voltage-scanning experiment on the products of the NO_3 + Δ-3-carene reaction. Changes in iodide adduct signals were measured by the iodide CIMS as a function of the voltage difference between the skimmer and quadrupole ion guide located between the ion-molecule reactor and mass analyzer.

In general, the weaker the iodide adduct, the lower the iodide CIMS sensitivity. This is also illustrated in Figure 2.16, where the ratio between the iodide CIMS and Vocus signals (summed over the parent and all fragments) is shown for each product and in Figure 2.17, where this ratio is shown as a function of dV_{50}, which is the voltage at which the iodide adducts are at 50% of their maximum value. A clear trend is observed for the ratio of the sensitivities of the iodide CIMS and Vocus instruments: the more functionalized compounds, like PDCN, are detected more efficiently by the iodide CIMS compared to the less functionalized compounds, like DC. We did not find a clear relationship between the Vocus-derived iodide CIMS sensitivity and the iodide CIMS sensitivity from the voltage scanning method.

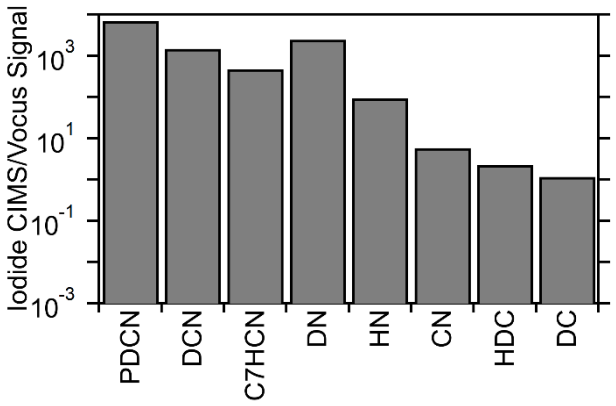

Figure 2.16 Ratios of iodide CIMS and Vocus signals measured for NO_3 + Δ-3-carene reaction products.

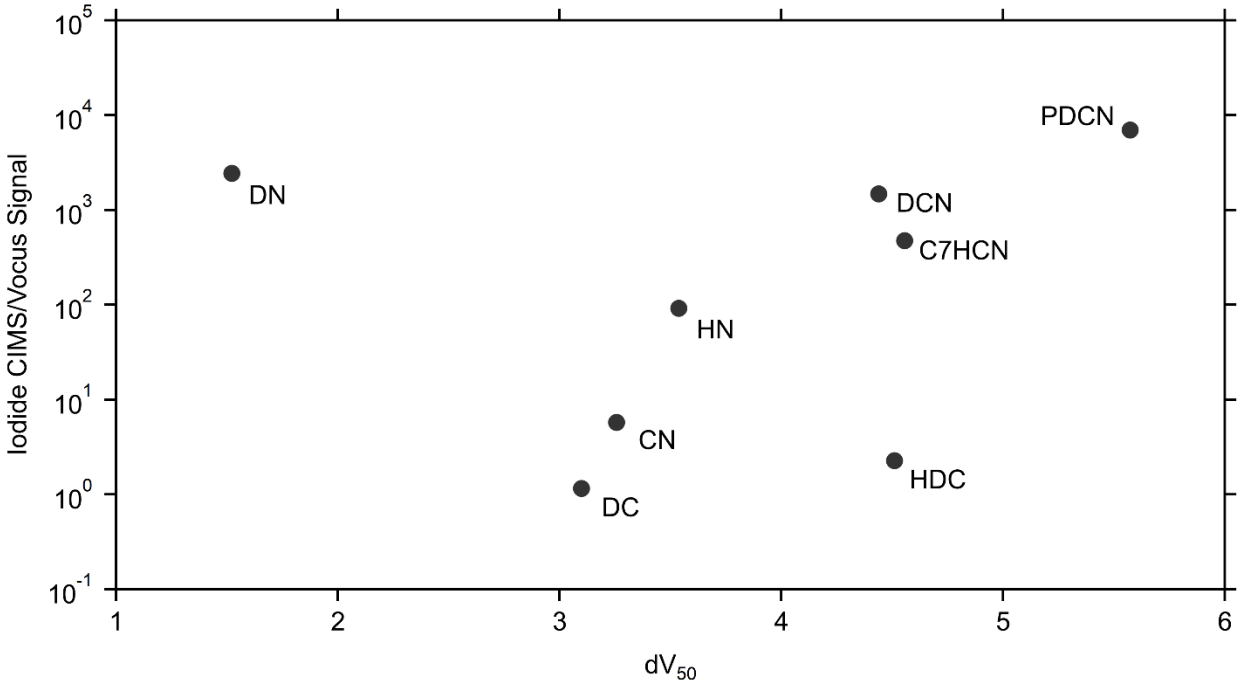

Figure 2.17 The ratio between the iodide CIMS and Vocus signals for Δ-3-carene oxidation products as a function of dV_{50}, which is the voltage where the iodide adducts are at 50% of their maximum value. There are likely DN fragments in the Vocus that were not able to be assigned.

2.4. Conclusions

This work describes the gas-phase products, yields, and mechanism of the reaction of Δ-3-carene with NO_3 radicals. The measured total molar yield of gas-phase products was 50%, which consisted of multifunctional compounds containing ketone, aldehyde, alcohol, carboxylic acid, peroxide, epoxide, and nitrate functional groups. Acetic acid had the largest yield of 14%, followed by acetone at 9%, DC at 8%, CN at 4%, acetaldehyde at 4%, and HN at 2%. The total gas-phase organic nitrate yield was 7%, due to mostly CN and HN.

The iodide CIMS was found to be a valuable tool for identifying parent ions, and the Vocus allowed for easier quantification of gas-phase products. Tubing delay experiments proved to be a useful tool in identifying ion fragments in the Vocus, which was essential for more accurately quantifying gas-phase product yields. Implementation of the voltage scanning technique showed

that the iodide CIMS is more sensitive to the degree of product functionalization than the Vocus. We are currently exploring whether these differences can be described by structure-activity relationships, which would be helpful for quantifying products with the iodide CIMS.

In addition to the described advances in methods of gas-phase product analysis, this study of the oxidation of Δ-3-carene by NO_3 radicals allows for a better understanding of the fate of monoterpenes in the atmosphere and their reaction products, including organic nitrates. The results should prove useful for interpreting field data and improving chemical models.

Chamber and Field Investigation of Gas-Phase Products of NO_3 Radical Oxidation of Five Monoterpenes

3.1. Introduction

Globally, about 150 Tg monoterpenes (34% α-pinene, 23% ocimene, 17% β-pinene, 9% limonene, 7% sabinene, 6% Δ-3-carene, and 3% myrcene) are emitted to the atmosphere each year (Sindelarova et al., 2014; Guenther et al., 2012). After emission, these monoterpenes are quickly oxidized to form lower volatility products that can partition to the particle phase (Hallquist et al., 2009). This particulate matter can have adverse health effects on humans and the ecosystem, and also impact visibility (Reichstein et al., 2014; Pöschl, 2005). Organic nitrates are formed from monoterpene oxidation by OH radicals under high NO_x conditions during the day and by NO_3 radicals at night (Perring et al., 2013). The formation of SOA from the oxidation of biogenic volatile organic compounds (BVOCs) is thus controlled by anthropogenic emissions of nitrogen oxides (NO_x) (Weber et al., 2007). The nighttime chemistry studied here is an example of how monoterpene oxidation can be affected by anthropogenic emissions of NO_x.

Formation of organic nitrates from nitrate radical monoterpene oxidation is well understood. Previous studies that have evaluated the mechanisms and SOA yields of the most abundant monoterpenes with nitrate radicals have found that the differences in structure between the monoterpenes (Δ-3-carene, a [4.1.0] bicyclic compound with an internal C=C bond; α-pinene, a [3.1.1] bicyclic compound with an internal C=C bond; β-pinene, a [3.1.1] bicyclic compound with a terminal C=C bond; ocimene, an acyclic compound with a terminal C=C bond and two internal C=C bonds; and limonene, a monocyclic compound with an internal C=C bond and a terminal C=C bond) affect the SOA yield and quantifying the differences helps to elucidate the oxidation mechanisms (Kurtén et al., 2017). Computational studies by Kurtén et al. (2017) suggest that breaking bonds in nitrooxy alkoxy radicals derived from Δ-3-carene produces reactive keto-

nitrooxy-alkyl radicals, facilitating SOA formation. In contrast, bond scissions in nitrooxy alkoxy radicals from α-pinene primarily yield pinonaldehyde, which is less reactive and volatile, limiting organonitrate and SOA production (Kurtén et al., 2017).

In this study, we focused on the first generation gas-phase products from the nitrate radical oxidation of Δ-3-carene, α-pinene, β-pinene, ocimene, and limonene, the monoterpenes that make up about 90% of global monoterpene emissions (Sindelarova et al., 2014). These reactions were investigated in an environmental chamber using trace-gas measurements with a Vocus and iodide CIMS. This combination of instruments allows the products to be detected as iodide adducts with the CIMS, whereas the measurements with the Vocus are used for quantification. After discussion of the reaction mechanisms, we will discuss how tubing delay experiments were performed to group parent and fragment ions in the Vocus for quantification of the oxidation products. We also used the voltage scanning method described by Lopez-Hilfiker et al. (2016) to study the sensitivity of the iodide CIMS for these reaction products and make a comparison with the Vocus measurements. Many of the ions attributed to monoterpene oxidation products in the lab were also observed during a field study in Los Angeles in summer of 2022 (Jensen, 2023). The composition of the monoterpene oxidation products observed in the field will be compared to that of the lab measurements. This work builds on the results of particle-phase measurements and SOA yields and a more detailed look at the gas-phase yields of Δ-3-carene oxidation by nitrate radicals published elsewhere (DeVault and Ziemann, 2021; DeVault et al., 2022; Jenks et al., 2023).

3.2 Experimental

3.2.1. Chemicals

The following chemicals with purities and suppliers were used: (1s)-(+)-3-carene (99%) and ocimene (90%) from Sigma Aldrich; (1R)-(+)-α-pinene (99%), (1S)-(-)-β-pinene (99%), (R)-

(+)-limonene (97%), 2-ethylhexyl nitrate (97%), from Aldrich Chemical Company; ultra-high purity (UHP) N_2 from Airgas; and a standard mixture (methanol, acetonitrile, acetaldehyde, acetone, acrylonitrile, isoprene, 2-butanone, benzene, toluene, m-xylene, 1,2,4-trimethylbenzene, α-pinene, and β-caryophyllene in N_2) from Apel-Riemer. N_2O_5 was prepared using the procedure described by Schott and Davidson (1958) and stored at -20°C.

3.2.2. Chamber Experiments

Chamber experiments were conducted in a ~7.4 m^3 Teflon FEP chamber and have been described in greater detail elsewhere (Jenks et al., 2023). Under nitrogen flow, liquid monoterpene was evaporated into the chamber using a glass bulb to produce ~500 ppbv concentration and NO_3 radicals were introduced by adding ~150 ppb N_2O_5 into the chamber (thermally decomposing to NO_2 and NO_3 radicals). To ensure complete mixing in the chamber a Teflon-coated fan was used following each addition. Under these conditions, the majority of NO_3 radicals reacted with the monoterpene to form predominantly first-generation products.

Our previous work has shown that measurement delay times caused by the Teflon sampling line can be useful for the interpretation of the Vocus mass spectra. For these experiments, the 1.5 m Vocus sampling line was replaced with a 5 m one after ~30 min. Once the tubing reached partitioning equilibrium with the gas-phase products, tubing delay experiments were performed as described in Jenks et al. (2023). Briefly, we determined measurement delay times for each *m/z* and used the data to group together product ions in the Vocus with the same delay times that likely come from the same reaction products. The longer sampling line was used to enhance the effects of the gas-wall interactions.

3.2.3. Ambient Measurements

Ambient monoterpene measurements were undertaken in Pasadena, California as a component of the CalNext-2022 campaign, serving as a follow-up of the California Nexus 2010 (CalNex-2010) campaign (Ryerson et al., 2013). Measurements spanned from June 30th to August 14th, 2022. Ambient air samples were gathered from a location atop Caltech Hall, with the inlet situated approximately 44 meters above ground level. Further details can be found in Jensen (2023).

3.2.4. Vocus Proton-Transfer-Reaction Time-of-Flight Mass Spectrometer

The Vocus has been described by Krechmer et al. (2018). It consists of a discharge reagent-ion source, which produces H_3O^+ ions, a focusing ion-molecule reactor (FIMR) where analytes are ionized and focused onto a sampling orifice, a big segmented quadrupole (BSQ), a primary beam ion optics region (PB), and a long time-of-flight (LTOF) mass analyzer for measurement of the product ions. The water vapor flow rate through the ion source was 15 sccm, and the applied discharge current was 2.0 mA. The Vocus was operated under conditions (for both laboratory and field measurements) resulting in a reduced electric field (E/N) of ~160 Td. The BSQ RF voltage amplitude was 255 V at 2.25 MHz. The Vocus acquired data with a time resolution of 1 s.

A standard mixture of VOCs (methanol, acetonitrile, acetaldehyde, acetone, acrylonitrile, isoprene, 2-butanone, benzene, toluene, m-xylene, 1,2,4-trimethylbenzene, α-pinene, and β-caryophyllene in N_2) was used for six-point calibrations in the Vocus by diluting the mixture in zero air to mixing ratios of ~30 ppbv to ~10 ppbv (except for β-caryophyllene which is ten times more dilute). These calibrations were performed immediately following chamber experiments to determine the Vocus sensitivity for the VOCs in the standard mixture. Measured sensitivities are shown in Table 3.1.

Table 3.1 Sensitivities of calibration standards.

Standard	Formula	k_{ptr} (10^{-9} cm^3 $molecule^{-1}$ s^{-1}) (Cappellin et al., 2012)	Carene Experiment Calibration Factor (cps $ppbv^{-1}$)	α-Pinene Experiment Calibration Factor (cps $ppbv^{-1}$)	β-Pinene Experiment Calibration Factor (cps $ppbv^{-1}$)	Limonene Experiment Calibration Factor (cps $ppbv^{-1}$)	Ocimene Experiment Calibration Factor (cps $ppbv^{-1}$)
Methanol	CH_4O	2.04	17	16	47	1203	
Acetonitrile	C_2H_3N	3.68	1578	1623	4658	4776	
Acetaldehyde	C_2H_4O	2.93	1616	1576	7187	876	
Acrylonitrile	C_3H_3N	Not found	3872			1637	
Acetone	C_3H_6O	3.09	4127	4081	17663	1754	
MEK	C_4H_8O	2.98	3733	4013	15309	1576	
Isoprene	C_5H_8	1.95	1066	1154	5480	446	
Benzene	C_6H_6	1.93	1594	1752	9591	631	
Toluene	C_7H_8	2.07	2247	2509	14128	772	
m-Xylene	C_8H_{10}	2.26	2418	2739	11122	766	
1,2,4-Trimethylbenzene	C_9H_{12}	2.4	1922	2210	13827	566	
α-Pinene	$C_{10}H_{16}$	2.37	2242	2528	9591	2342	
Δ-3-Carene	$C_{10}H_{16}$	2.44	2634	N/A	N/A	N/A	

β-Caryophyllene	$C_{15}H_{24}$	2.89	423			165	
2-Ethylhyexyl Nitrate	$C_8H_{17}NO_3$	Not found	1494	N/A	N/A	N/A	N/A
Cyclohexyl Nitrate	$C_6H_{11}NO_3$	Not found	1637	N/A	N/A	N/A	N/A
Acetic acid	$C_2H_4O_2$	1.86	N/A	N/A	N/A	N/A	N/A
Formic acid	CH_2O_2	1.66	N/A	N/A	N/A	N/A	N/A
Formaldehyde	CH_2O	2.56	N/A	N/A	N/A	N/A	N/A

Mixing ratios for the products from the NO_3 + monoterpene reactions were calculated by using the average calibration factor of the standard mixture for each experiment, with the exception of those VOCs that are contained in the standard mixtures used to calibrate the instrument (e.g. acetone, acetaldehyde). The transmission curve in Figure 3.1 was used to adjust the calibration factors for compounds with $m/z < 60$ (formic acid, acetaldehyde, and formaldehyde) to account for mass discrimination in the BSQ.

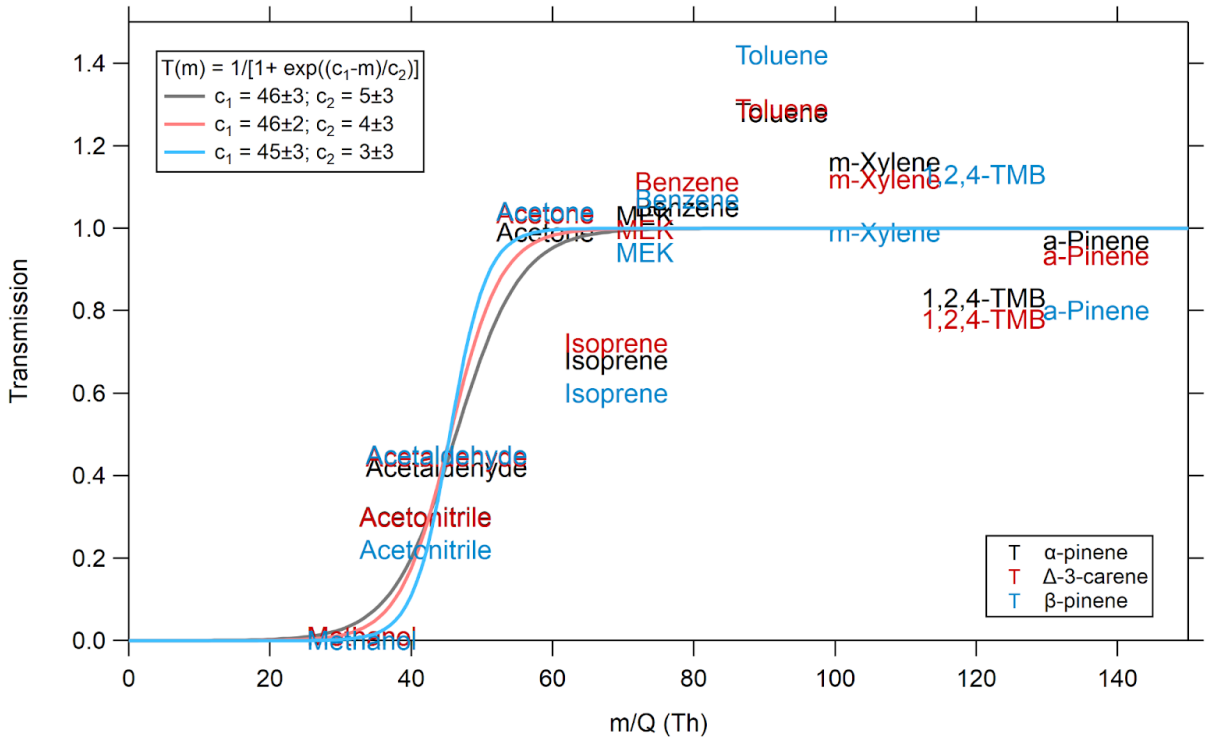

Figure 3.1 The sigmoidal transmission fit of calibration standards for three experiments measured by the Vocus assuming a base of zero.

3.2.5. Iodide Chemical Ionization Mass Spectrometer

The high-resolution time-of-flight chemical-ionization mass spectrometer using iodide adducts (iodide CIMS) consists of a Po-210 source (to produce I^- reagent ions from CH_3I), an ion-

molecule reactor (IMR), a small segmented quadrupole (SSQ), a BSQ, a PB region, and an LTOF. The pressure in the IMR was ~100 mbar. Chamber air was sampled at 2 L min^{-1} and mass spectra were measured at 1 Hz. Calibrations were not performed for this instrument; however, any signal variability due to changes in the iodide concentration were accounted for by normalizing product ion signals to the reagent ion signals (I^- + $I \cdot H_2O^-$).

3.2.6. Data Processing

Tofware (v3.2.3, www.tofwerk.com/tofware) in the Igor Pro 8 (Wavemetrics, OR, USA) environment was used for processing data from both the Vocus and the iodide CIMS. Peaks were assigned formulas manually, then the time series of these peaks were calculated using peak shape fitting. Backgrounds were measured from the clean chamber immediately before the addition of the monoterpene. Vocus data were normalized to $(H_2O)_2H^+$ and iodide CIMS data were normalized to the sum of the I^- and $I \cdot H_2O^-$ signals, which is indicated by the units of normalized counts per second (ncps). Mass-to-charge ratio calibration was performed using ions between *m/z* 42 and 371 with a resulting accuracy of ~5 ppm for the Vocus and between *m/z* 46 and 381 with an accuracy of ~5 ppm for the iodide CIMS.

3.2.7. Modeling

Product yields for α-pinene, β-pinene, and limonene were modeled with the Master Chemical Model (MCM, version 3.3.1) using the Framework for 0-D Atmospheric Modeling (F0AM), a near-explicit chemical model that outlines the reaction of VOCs, leading to the production of ozone and other secondary pollutants (Wolfe et al., 2016; Saunders et al., 2003).

3.3. Results and Discussion

3.3.1. Reaction Mechanism

The mechanisms for the reaction between monoterpenes and NO_3 have been described elsewhere (Kurtén et al., 2017; DeVault and Ziemann, 2021; DeVault et al., 2022; Jenks et al., 2023; Atkinson and Arey, 2003; Ng et al., 2013; Dam et al., 2022; Draper et al., 2019; Wängberg et al., 1997; Bates et al., 2022; Claflin and Ziemann, 2018; Boyd et al., 2015; Fry et al., 2011; Leungsakul et al., 2005; Spittler et al., 2006). Schemes 1 and 2 illustrate a summary mechanism with the reactions that are the most relevant for the work described here.

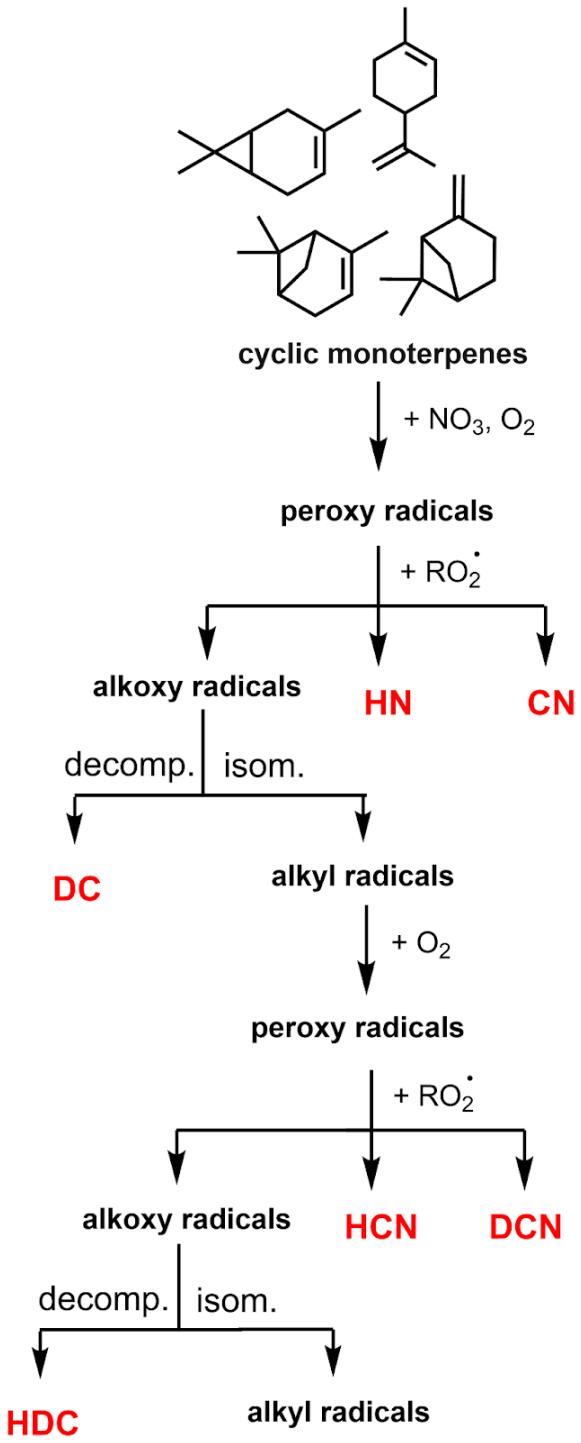

Figure 3.2 The proposed gas-phase reaction mechanism for the oxidation of the cyclic monoterpenes by NO_3 radicals.

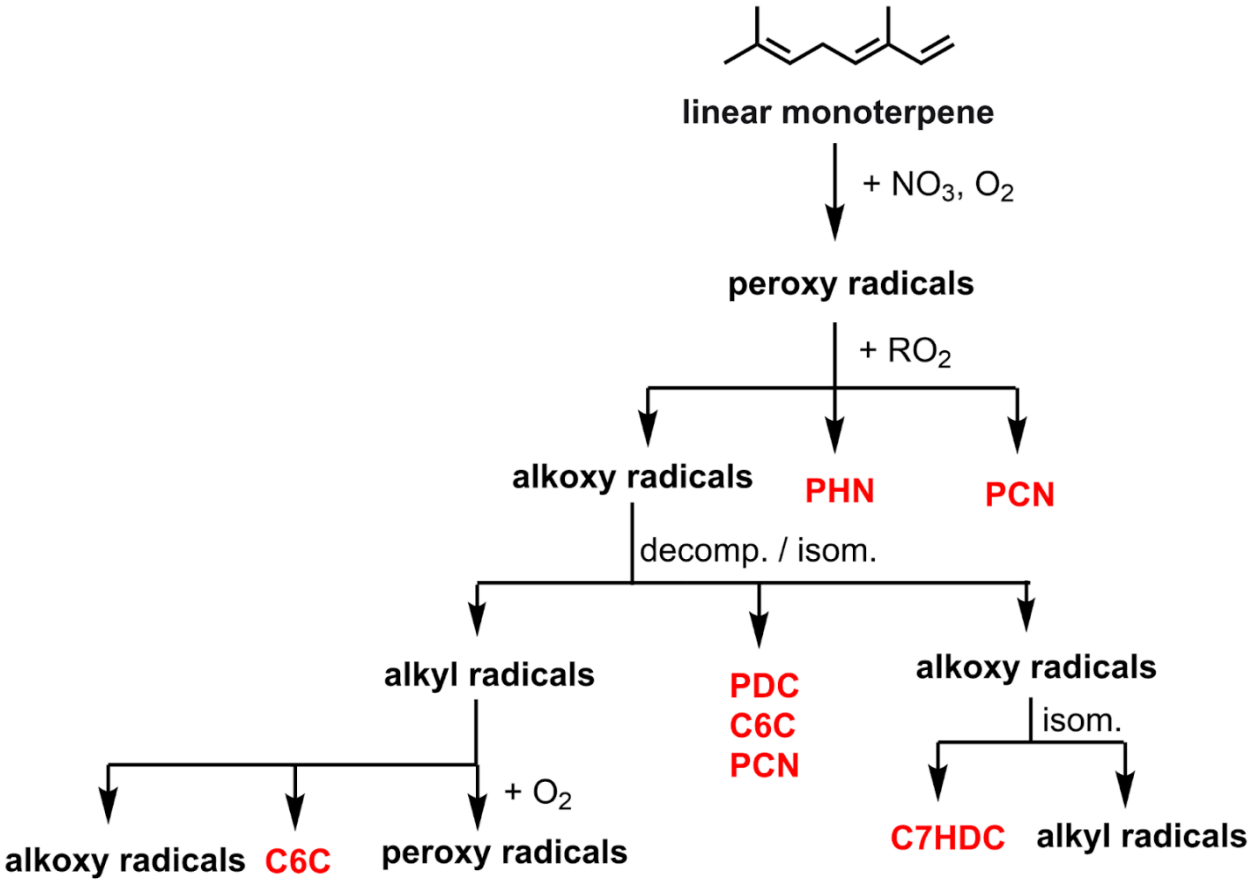

Figure 3.3 The proposed gas-phase reaction mechanism for the oxidation of the linear monoterpene by NO_3 radicals.

In the first step, a nitrate group is added to a C=C bond in the monoterpene to form an alkyl radical. Oxygen rapidly adds to the alkyl radical to form a peroxy radical. The peroxy radical then reacts with RO_2 to form the hydroxy nitrate (HN) and the carbonyl nitrate (CN) for the cyclic monoterpenes or the peroxy hydroxy nitrate (PHN) and the peroxy carbonyl nitrate (PCN) for the linear monoterpene. This step can also form an alkoxy radical, which can lose NO_2 forming the dicarbonyl (DC) for Δ-3-carene, α-pinene, and limonene, the C9 carbonyl (C9C) for β-pinene, and peroxy dicarbonyl (PDC) for ocimene. The alkoxy radical can also go on to propagate another peroxy radical after the addition of O_2, which will go on to form more oxygenated species like the

hydroxy carbonyl nitrate (HCN) and the dicarbonyl nitrate (DCN) for the cyclic monoterpenes or peroxy carbonyl nitrate (PCN) for the linear monoterpene in a similar reaction mechanism. Schemes 3.1-3.5 show more extensive proposed reaction mechanisms for each of these monoterpenes.

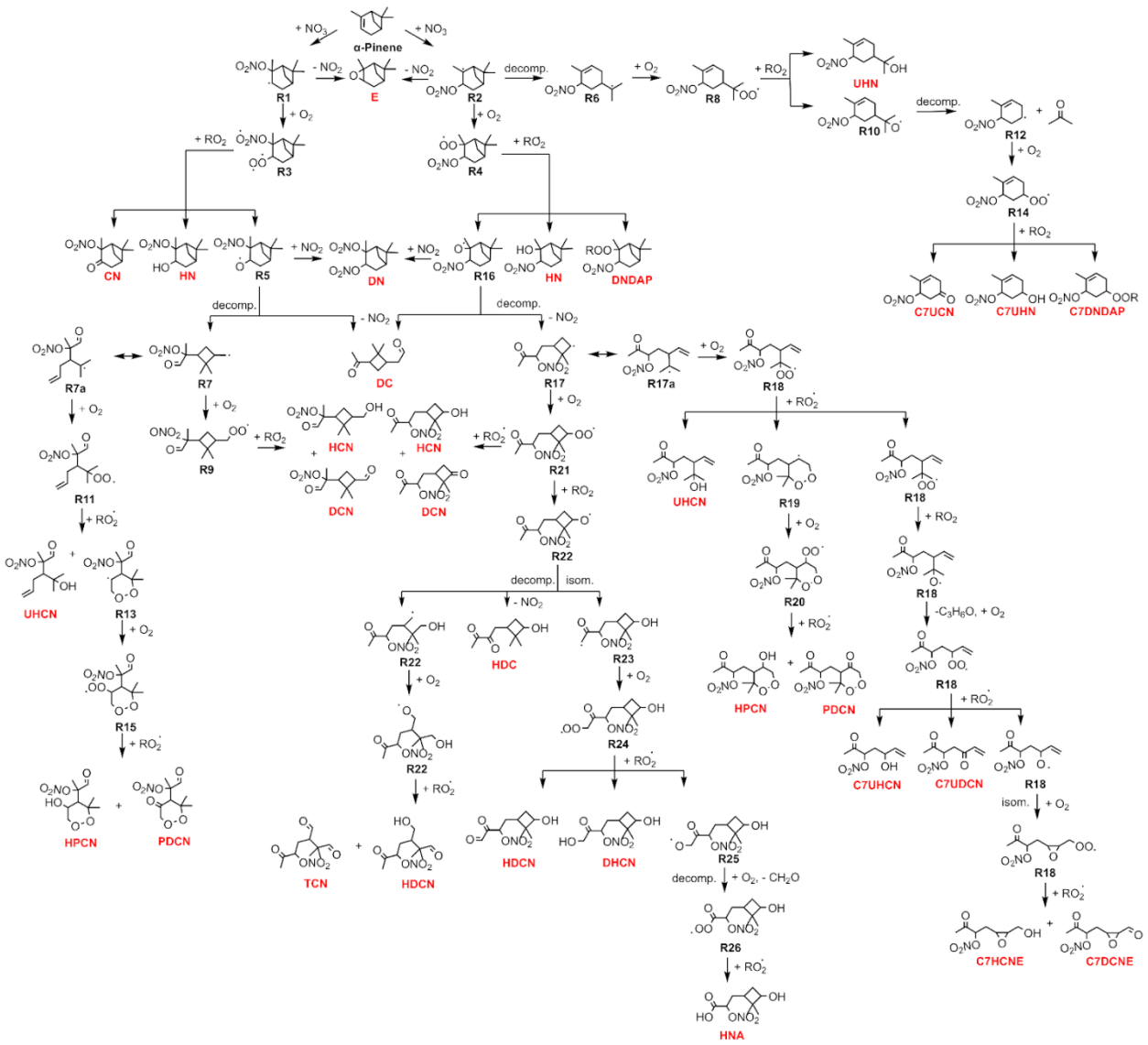

Figure 3.4 Proposed gas-phase reaction mechanism for the oxidation of α-pinene by NO_3 radicals.

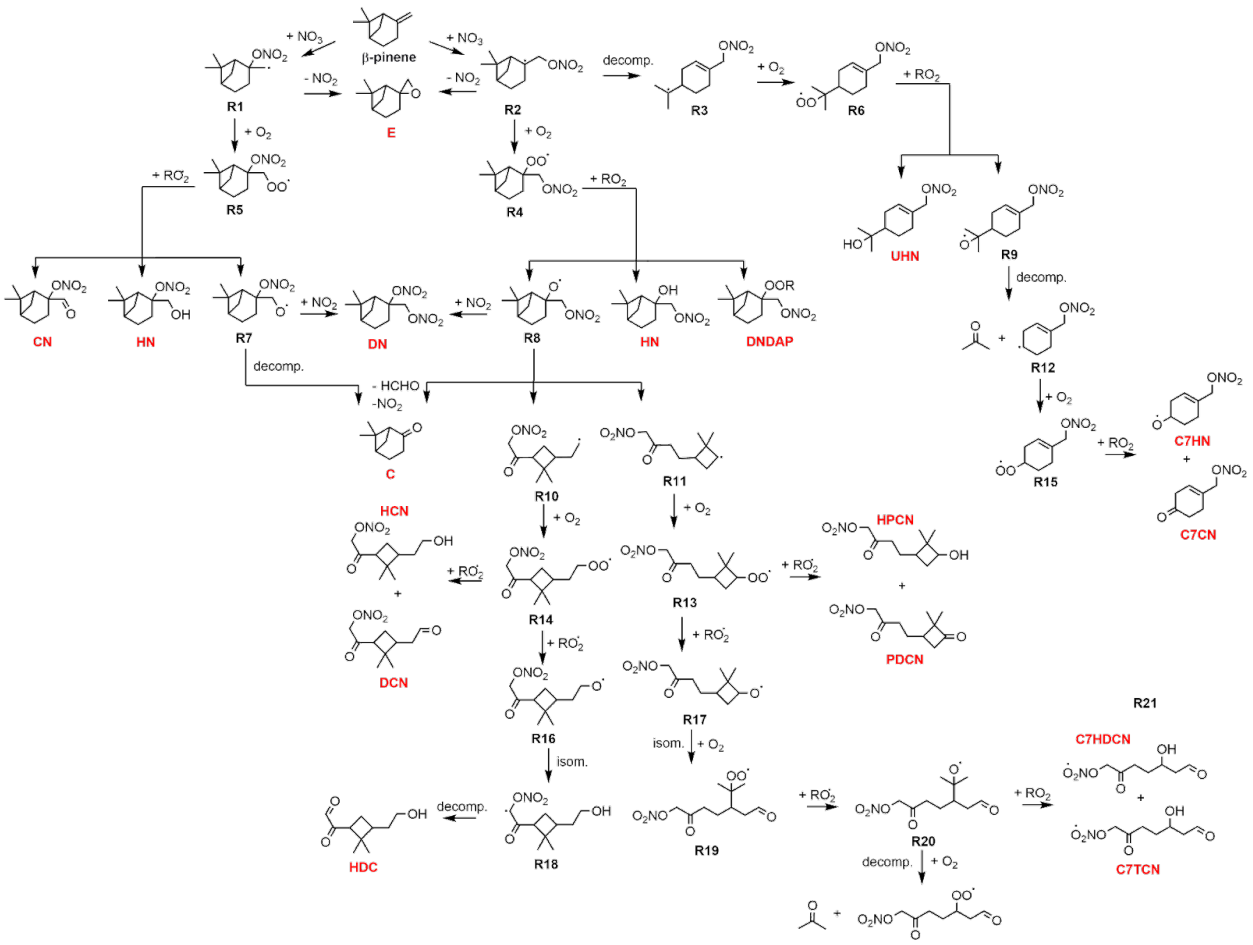

Figure 3.5 Proposed gas-phase reaction mechanism for the oxidation of β-pinene by NO_3 radicals.

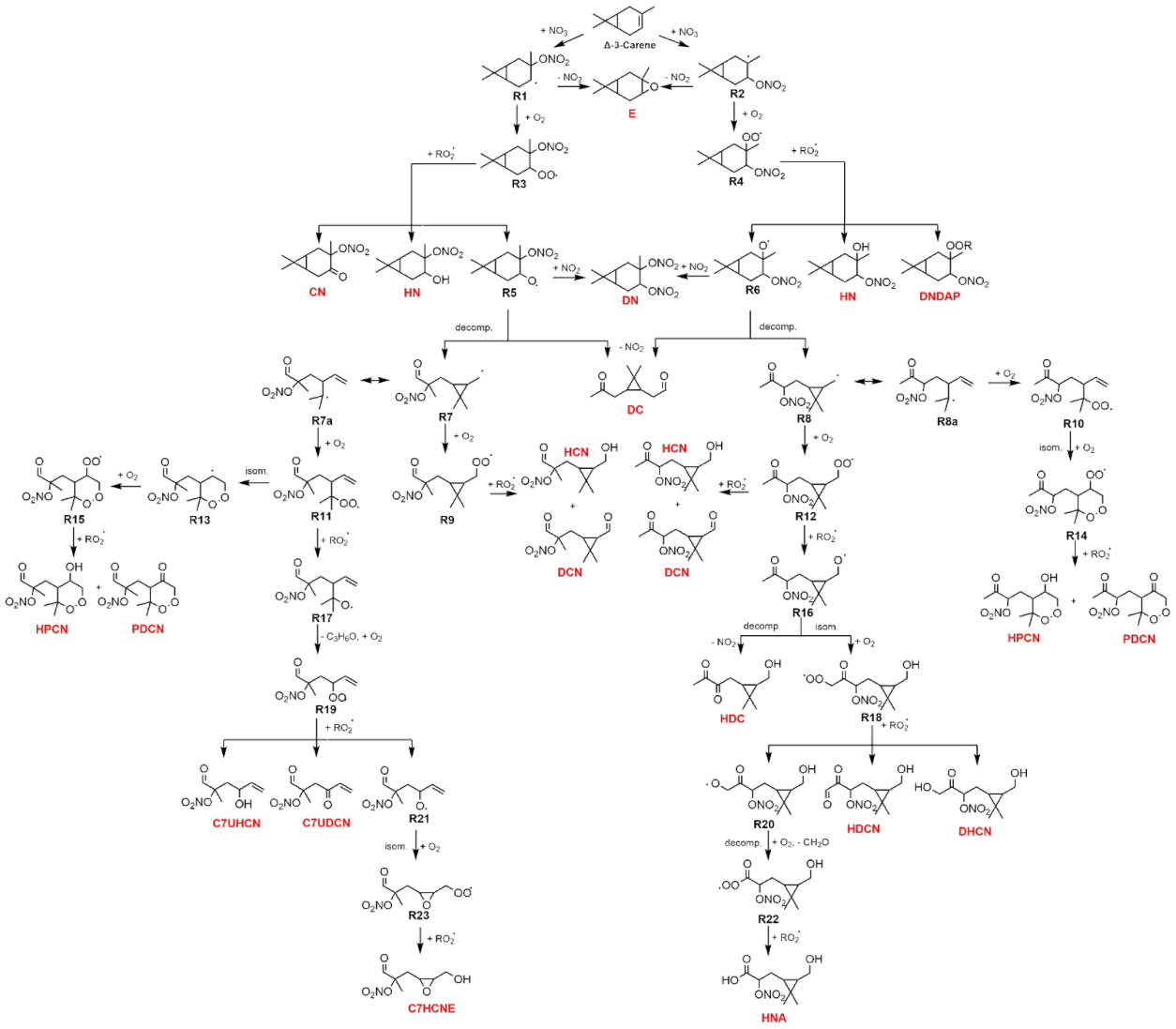

Figure 3.6 Proposed gas-phase reaction mechanism for the oxidation of Δ-3-carene by NO_3 radicals.

Figure 3.7 Proposed gas-phase reaction mechanism for the oxidation of limonene by NO_3 radicals.

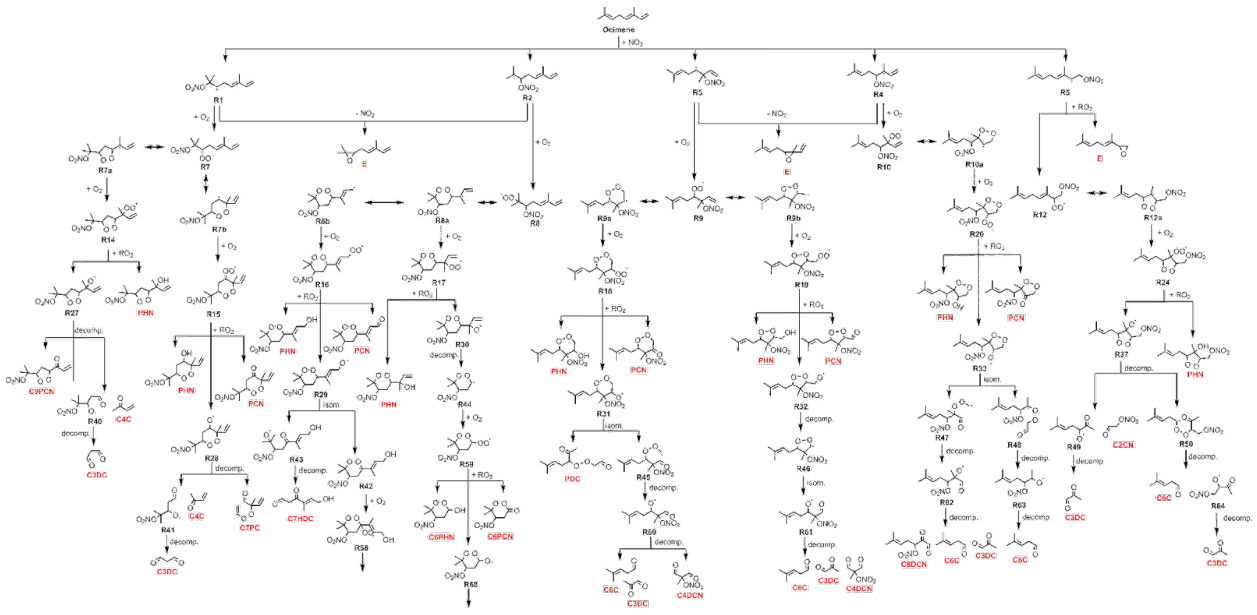

Figure 3.8 Proposed gas-phase reaction mechanism for the oxidation of ocimene by NO_3 radicals.

3.3.2. Time Series Measurements and Mass Spectra

Figure 3.2 shows the time series of the five monoterpenes, N_2O_5, and a few gas-phase oxidation products for each experiment. The reactions were initiated by the addition of N_2O_5 to the chamber (which quickly forms NO_3 through thermal decomposition) and was complete in <5 min after all the NO_3 had reacted, primarily with the monoterpene. The iodide CIMS time series show the addition and depletion of N_2O_5 (and thus NO_3) in a few minutes and the increase of products like HN, HCN, and DCN. The Vocus time series shows the depletion of the monoterpene by ~40% and the increase of products like DC, CN, and HN. Due to a sampling error for the iodide CIMS measurements of the β-pinene reaction, some data is missing in the time series.

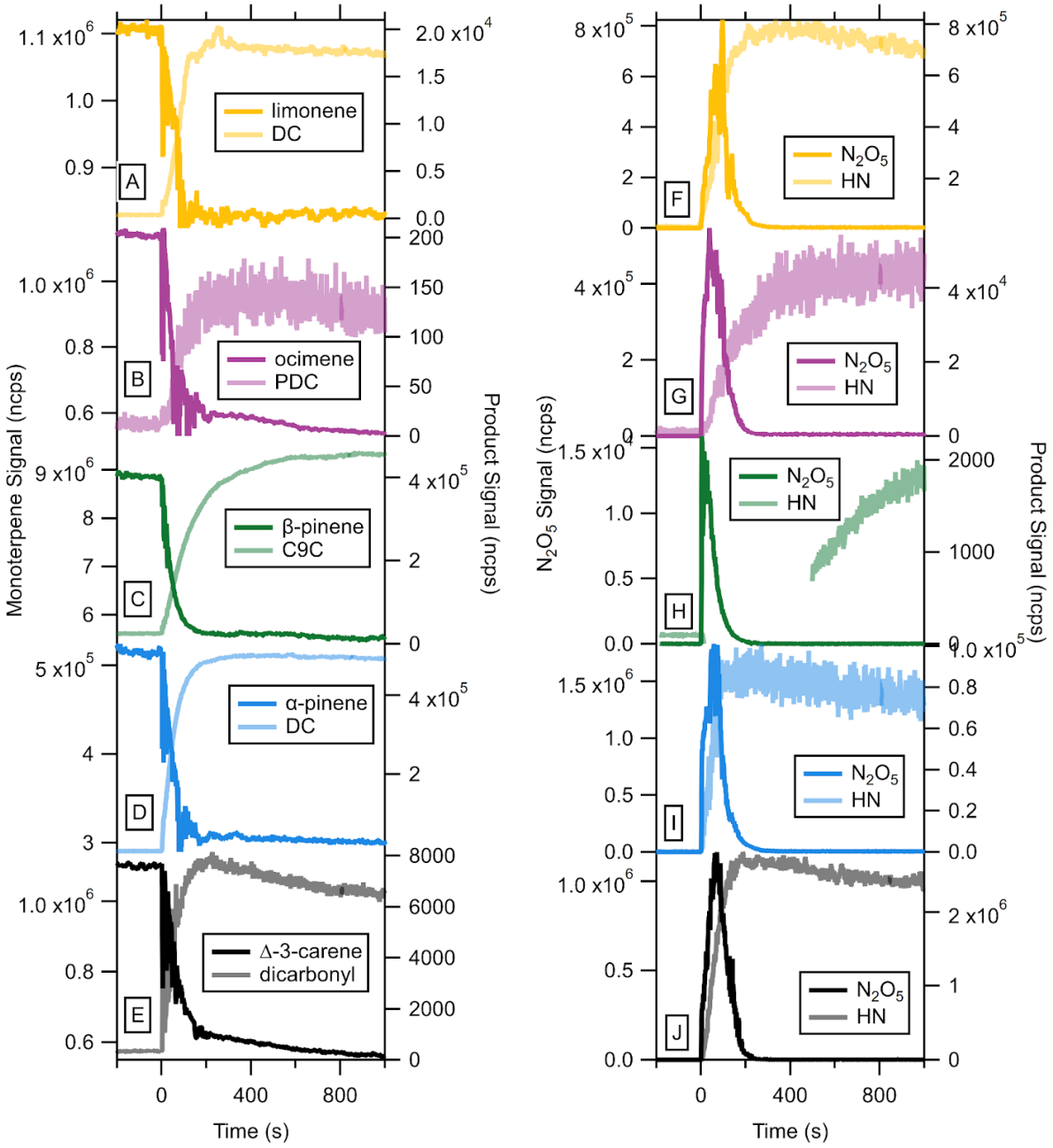

Figure 3.9 Time series of limonene, ocimene, β-pinene, α-pinene, and Δ-3-carene, and a selected oxidation product for each monoterpene detected by the Vocus (A-E). Time series of N_2O_5 and a selected oxidation product for each experiment detected by the iodide CIMS (F-J).

The mass spectra of the oxidation products detected by the Vocus and iodide CIMS are shown in Figure 3.3 and Figure 3.4. The Vocus mass spectra show similarities between α-pinene,

limonene, and Δ-3-carene. The dicarbonyl and its fragments are one of the main products shown in these mass spectra. In β-pinene, C9C is formed rather than DC, but otherwise the mass spectrum looks similar to that of α-pinene, limonene, and Δ-3-carene. Because of fragmentation of gas-phase products in the reaction mechanism (not to be confused with fragmentation in the Vocus) for ocimene, the mass spectrum shows much more signal in the lower *m/z* range. The iodide CIMS mass spectrum shows similarities between the cyclic monoterpenes, with HCN, DCN, HN, and CN being the main gas-phase products detected by the iodide CIMS. There are differences in the linear monoterpene (ocimene) mass spectrum, with PCN and PHN being the main gas-phase products detected by the iodide CIMS.

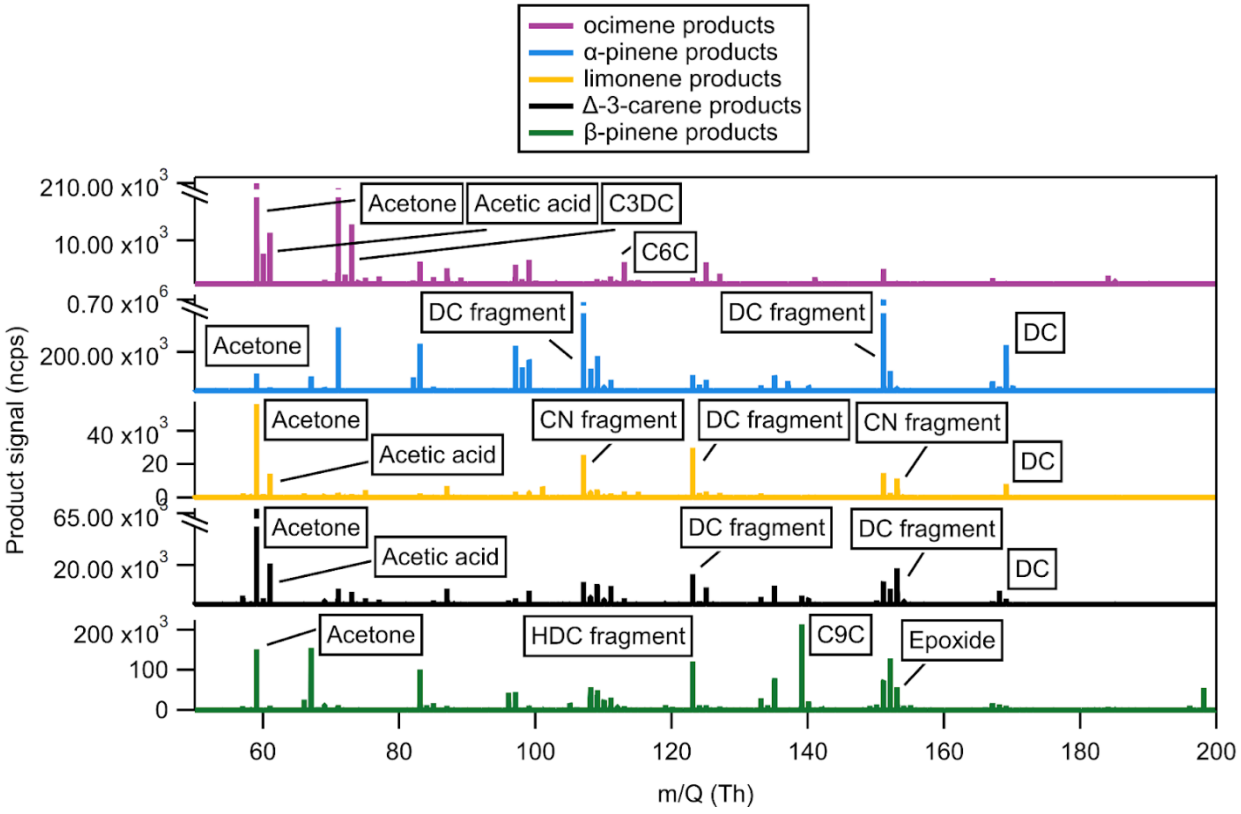

Figure 3.10 Vocus mass spectra of the products detected from the reactions of ocimene, α-pinene, limonene, Δ-3-carene, and β-pinene with NO_3 radicals.

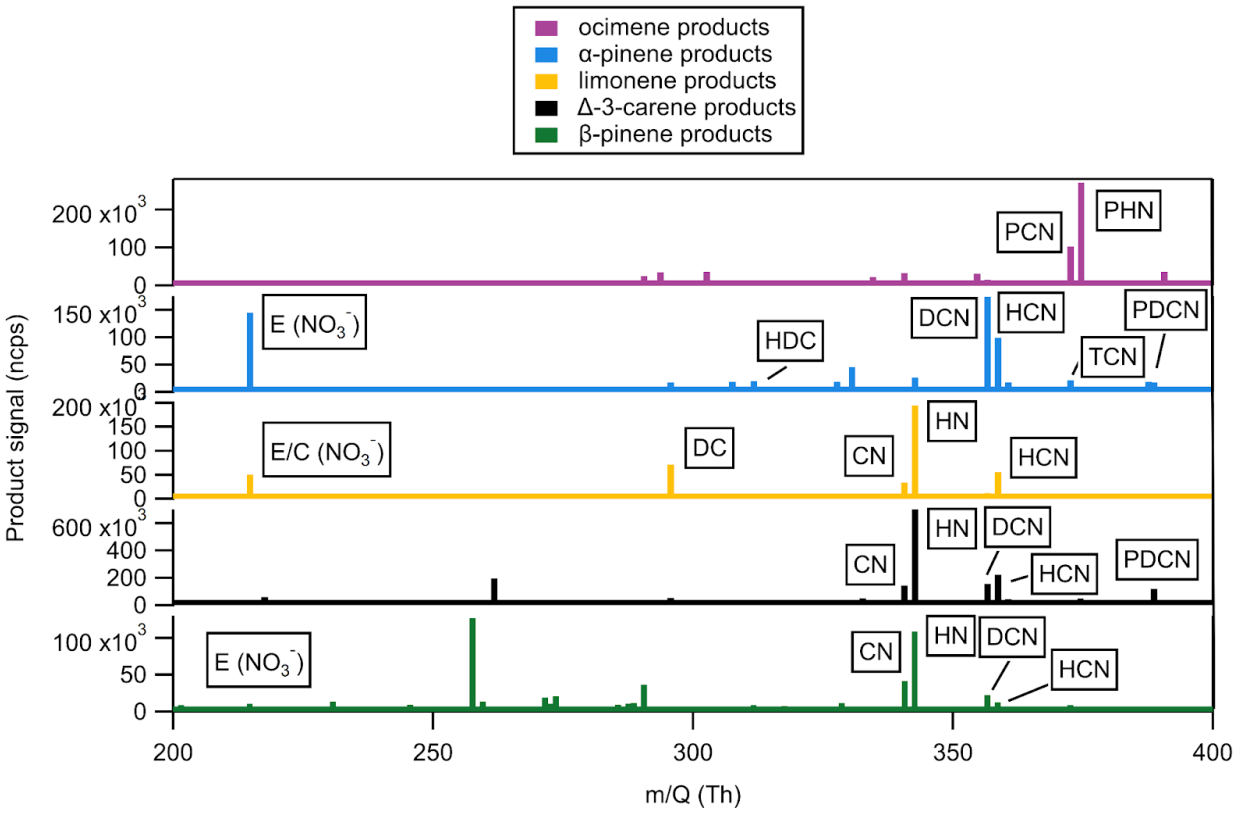

Figure 3.11 Iodide CIMS mass spectra of the products detected from the reactions of ocimene (purple), α-pinene (blue), limonene (yellow), Δ-3-carene (black), and β-pinene (green) with NO_3 radicals.

Figure 3.5 shows the fraction of the total signal for select products formed by the oxidation of cyclic monoterpenes.

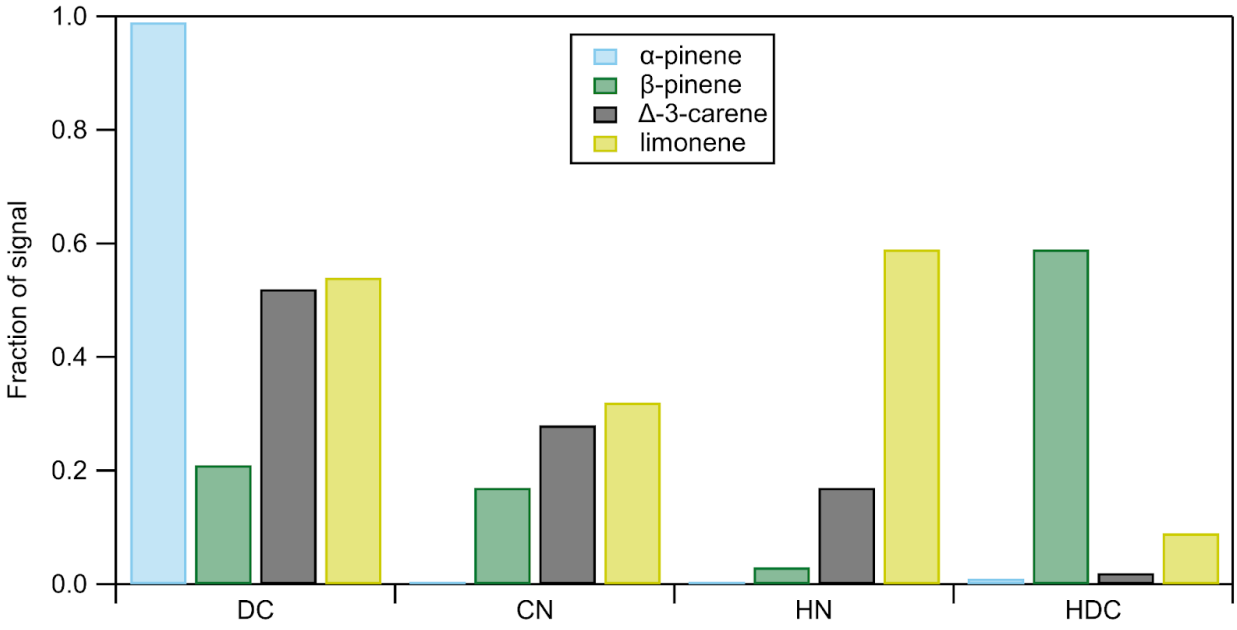

Figure 3.12 Relative signal distribution for four gas-phase oxidation products (DC, CN, HN, HDC) for each of the cyclic monoterpene oxidation experiments. The signal fractions are calculated such that the sum of the different products adds up to 1 for each monoterpene.

3.3.3. Product Yields

Using the Vocus and the iodide CIMS together can be a powerful tool in analysis of gas-phase products. While the Vocus detects the monoterpene precursors, the iodide CIMS exclusively detects N_2O_5. In terms of quantification, the Vocus offers a more straightforward approach, enabling sensitivity estimation even in the absence of calibration standards. Conversely, the iodide CIMS exhibits widely varying sensitivities across different compounds, leading to significant uncertainty in product quantification without authentic calibration standards. Fragmentation of product ions is infrequent in the iodide CIMS, but it is common in the Vocus, especially for compounds with alcohol, aldehyde, acid, ester, and nitrate groups as seen in this and previous work

(Jenks et al., 2023; Pagonis et al., 2019). This complicates signal attribution and necessitates careful consideration in product yield quantification. As detailed in Jenks et al. (2023), Vocus parent and fragment ions were grouped based on their inlet delay times and elemental composition for more accurate yield calculations for select gas-phase products.

Table 3.2 and Table 3.3 show the gas-phase products detected by the Vocus and iodide CIMS that we are focusing on in this work. Additionally, the product signals, shown in % of total product signal, are listed in Table 3.2 and Table 3.3. Notable differences are the high relative signals of DC in α-pinene, CN in limonene, HDC in β-pinene, and HN in Δ-3-carene. This can mostly be attributed to differences in monoterpene precursor structure. As described in Kurtén et al. (2017), the nitrooxy alkoxy radicals derived from Δ-3-carene produces reactive keto-nitrooxy-alkyl radicals, facilitating SOA formation, and therefore reducing the yield of DC. In contrast, the nitrooxy alkoxy radical derived from α-pinene limits SOA formation by almost exclusively forming DC.

Table 3.2 Proposed gas-phase products and signals (% of total product signal) formed from the reaction of Δ-3-carene, α-pinene, β-pinene, limonene, and ocimene by NO_3 radicals detected by the Vocus.

Product ID	Formula	Δ-3-carene product signal (% of total)	α-pinene product signal (% of total)	β-pinene product signal (% of total)	limonene product signal (% of total)	ocimene product signal (% of total)
Dicarbonyl (DC)	$C_{10}H_{16}O_2$	15.99	62.21	NE	17.05	NE
C9 carbonyl (C9C)	$C_9H_{14}O$	NE	NE	4.42	NE	NE
C6 carbonyl (C6C)	$C_6H_{10}O$	NE	NE	NE	NE	0.03
Carbonyl nitrate (CN)	$C_{10}H_{15}NO_4$	8.73	0.16	3.57	23.86	0.10
Peroxy carbonyl nitrate (PCN)	$C_{10}H_{15}NO_6$	NE	NE	NE	NE	0.22
Hydroxy dicarbonyl (HDC)	$C_{10}H_{16}O_3$	0.75	0.62	12.51	2.94	NE
C7 hydroxy dicarbonyl (C7HDC)	$C_7H_{11}O_3$	NE	NE	NE	NE	0.60
Dicarbonyl nitrate (DCN)	$C_{10}H_{15}NO_5$	0.04	0.02	0.46	0.02	0.02
peroxy dihydroxy nitrate (PDHN)	$C_{10}H_{17}NO_7$	NE	NE	NE	NE	0.06
Hydroxy nitrate (HN)	$C_{10}H_{17}NO_4$	5.25	0.04	0.56	1.62	0.21
Peroxy hydroxy nitrate (PHN)	$C_{10}H_{17}NO_6$	NE	NE	NE	NE	0.05
Epoxide (E)	$C_{10}H_{16}O$	1.14	0.57	1.77	1.63	0.02
Acetone	C_3H_6O	31.75	2.59	11.17	26.00	62.95
Acetic acid	$C_2H_4O_2$	17.88	5.92	4.72	14.25	10.62
Formic acid	CH_2O_2	0.49	0.04	0.30	0.30	0.29

Acetaldehyde	C_2H_4O	5.24	0.21	0.56	2.29	2.94
Formaldehyde	CH_2O	0.03	<0.01	0.01	0.02	0.05
Other		12.71	27.61	59.95	10.02	21.3

Table 3.3 Select proposed gas-phase products and signals (% of total product signal) formed from the reactions of Δ-3-carene, α-pinene, β-pinene, limonene, and ocimene by NO_3 radicals detected by the iodide CIMS.

Product ID	Formula	Iodide CIMS Detection	Δ-3-carene product signal (% of total)	α-pinene product signal (% of total)	β-pinene product signal (% of total)	limonene product signal (% of total)	ocimene product signal (% of total)
Dicarbonyl (DC)	$C_{10}H_{16}O_2$	$I•C_{10}H_{16}O_2^-$	1.91	2.12	NE	14.65	NE
C9 carbonyl (C9C)	$C_9H_{14}O$	$I•C_9H_{14}O^-$	NE	NE	ND	NE	NE
C6 carbonyl (C6C)	$C_6H_{10}O$	$NO_3•C_6H_{10}O^-$	NE	NE	NE	NE	0.12
Carbonyl nitrate (CN)	$C_{10}H_{15}NO_4$	$I•C_{10}H_{15}NO_4^-$	5.18	0.36	5.78	6.94	3.53
Peroxy carbonyl nitrate (PCN)	$C_{10}H_{15}NO_6$	$I•C_{10}H_{15}NO_6^-$	NE	NE	NE	NE	10.95
Hydroxy dicarbonyl (HDC)	$C_{10}H_{16}O_3$	$I•C_{10}H_{16}O_3^-$	0.15	2.36	1.24	0.86	NE
C7 hydroxy dicarbonyl (C7HDC)	$C_7H_{11}O_3$	$I•C_7H_{11}O_3^-$	NE	NE	NE	NE	0.51
Dicarbonyl nitrate (DCN)	$C_{10}H_{15}NO_5$	$I•C_{10}H_{15}NO_5^-$	5.63	20.70	3.14	2.47	NE
peroxy dihydroxy nitrate (PDHN)	$C_{10}H_{17}NO_7$	$I•C_{10}H_{17}NO_7^-$	NE	NE	NE	NE	3.84
Hydroxy nitrate (HN)	$C_{10}H_{17}NO_4$	$I•C_{10}H_{17}NO_4^-$	49.67	3.15	14.98	39.57	1.25
Peroxy hydroxy nitrate (PHN)	$C_{10}H_{17}NO_6$	$I•C_{10}H_{17}NO_6^-$	NE	NE	NE	NE	28.76
Epoxide (E)	$C_{10}H_{16}O$	$NO_3•C_{10}H_{16}O^-$	0.71	17.22	1.50	10.36	0.11
Acetone	C_3H_6O	$NO_3•C_3H_6O^-$	0.00	0.00	0.33	ND	ND
Acetic acid	$C_2H_4O_2$	$I•C_2H_4O_2^-$	0.00	0.00	0.00	0.00	0.10

Formic acid	CH_2O_2	$I•CH_2O_2^-$	0.15	0.00	1.28	0.03	0.17
Acetaldehyde	C_2H_4O	$NO_3•C_2H_4O$	0.03	0.05	8.98	0.02	0.04
Formaldehyde	CH_2O	$NO_3•CH_2O^-$	0.04	0.05	4.39	0.06	0.04
Other			36.53	53.99	58.38	25.04	50.58

Because of fragmentation in the Vocus, inlet delay experiments were performed to group select parent and fragment ions together and quantify product yields. This method has been described by Jenks et al (2023). Estimated product concentrations and molar yields (the amount of a product formed per mole of reactant consumed) from the reactions of the five monoterpenes by NO_3 radicals are shown in Table 3.3. The molar yield of gas phase products is 50% for Δ-3-carene, 91% for α-pinene, 48% for β-pinene, 44% for ocimene, and 73% for limonene. DeVault et al. (2022) reported an SOA molar yield of 34% for Δ-3-carene, 37% for α-pinene, 55% for β-pinene, 43% for ocimene, and 53% for limonene (DeVault et al., 2022). These findings suggest significant impacts of monoterpene structural characteristics on the gas- and particle-phase yields.

Table 3.4 Gas-phase products formed from the reaction of Δ-3-carene, α-pinene, β-pinene, limonene, and ocimene with NO_3 radicals. * Indicates that the calibration factor from standards was used. † Indicates that the value was adjusted due to mass discrimination.

Product ID	Formula	Δ-3-Carene Molar Yield (%)	α-Pinene Molar Yield (%)	β-Pinene Molar Yield (%)	Limonene Molar Yield (%)	Ocimene Product ID	Ocimene Molar Yield (%)
Dicarbonyl (DC) or C9 carbonyl (C9C) for β-Pinene	$C_{10}H_{16}O_2$	7.57	36.95	2.72	12.44	Peroxy dicarbonyl (PDC)	
Carbonyl nitrate (CN)	$C_{10}H_{15}NO_4$	4.13	0.01	2.20	9.03	Peroxy carbonyl nitrate (PCN)	0.12
Hydroxy nitrate (HN)	$C_{10}H_{17}NO_4$	2.48	<0.01	0.34	0.09	Peroxy hydroxy nitrate (PHN)	0.02
Formaldehyde†	CH_2O	0.63	0.18	0.52	0.40	Formaldehyde†	0.68

The (di)carbonyl yields were 8% for Δ-3-carene, 37% for α-pinene, 3% for β-pinene, and 13% for limonene. Previous studies have reported (di)carbonyl yields of 0-3% for Δ-3-carene, 40-72% for α-pinene, 0-2% for β-pinene, and 25-69% for limonene (Ng et al., 2017; Wängberg et al., 1997; Spittler et al., 2006; Hallquist et al., 1999). While the trends are the same -the DC yield for β-pinene was the lowest, followed by Δ-3-carene, limonene, and α-pinene- our absolute values are higher. CN yields were 4% for Δ-3-carene, 0% for α-pinene, 2% for β-pinene, and 9% for limonene. HN yields were 2% for Δ-3-carene and 0% for the other cyclic monoterpenes. Formaldehyde yields were 0-1% for all monoterpenes. These yields are also shown in Table 3.3.

These results can be compared to MCM modeled results, which are shown in Figure 3.#. Overall, the yields measured in the laboratory were much lower than that of the MCM model. This could be due to errors in the fragment assignments in the experimental results. On the other hand, our yields were higher than other yields determined from measurements. The yield of

formaldehyde from α-pinene was less than 1% for the model and experimental results. The yield of HN from α-pinene was 9% from the model, and <1% experimentally. The carbonyl was the largest product from α-pinene (81% from the model and 37% from experimental results). CN from α-pinene had a 6% yield from the model and <1% yield from the experimental results.

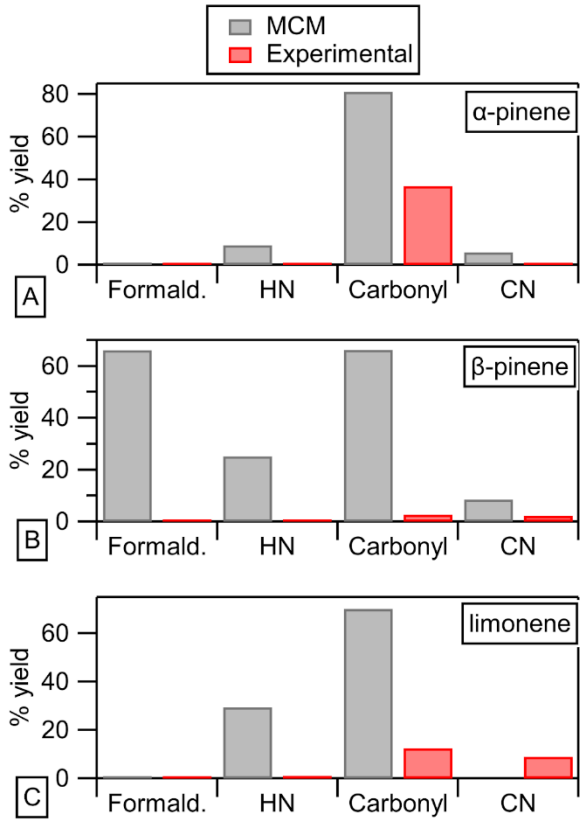

Figure 3.13 Yield comparison for α-pinene (A), β-pinene (B), and limonene (C) oxidation products between MCM model results and chamber experimental measurements.

The biggest difference in model vs. experimental yields was formaldehyde in β-pinene, which was 1% in the lab and 66% from MCM. This can be attributed to the low sensitivity of formaldehyde in the Vocus (the proton affinity of formaldehyde is close to that of water) (Warneke et al., 2011). The yield of HN formed from β-pinene was 25% from the model and <1% from the experimental results. The carbonyl was the β-pinene oxidation product with the largest yield (66%

from the model and 3% from the experimental results). CN from β-pinene had a yield of 9% from the model and 2% from the experimental results.

For limonene, the yield of formaldehyde was <1% for both the model and the experimental results. HN from limonene had a yield of 30% from the model and 1% from the experimental results. DC was the limonene oxidation product with the highest yield (70% from the model and 12% from the experimental results). The yields of CN were 0 and 9% from the model and experiments, respectively.

Some of the gas-phase products from ocimene included PCN, PHN, and PDC. These all had a molar yield of less than 1%. The extensive fragmentation in both the chemical mechanism and the Vocus, combined with the many isomers for each product complicated the fragmentation analysis used to calculate product yields for the cyclic monoterpenes.

An overarching conclusion is that the MCM overestimates gas-phase product yields in many cases. This has implications for both ozone and SOA chemistry and deserves further investigation. When oxidation products remain in the gas phase in the model, they can continue to participate in the reactions that form ozone and lead to overestimates. In contrast, it can lead to underestimates of SOA formation.

3.3.4. Voltage Scanning

The oxidation products are detected by the iodide CIMS with little or no fragmentation, which allows for the identification of products and evaluation of reaction mechanisms. However, quantifying product yields using the iodide CIMS is difficult because the sensitivity can vary by orders of magnitude between different compounds (Bi et al., 2021). Instrument sensitivities have been estimated using a "voltage scanning" method described by Lopez-Hilfiker et al. (2016), which estimates the bond strengths of iodide-product adducts. As the voltage difference between

the skimmer and the BSQ increases, the collision energy increases, and the adducts can then dissociate into I^- and a neutral molecule by the strength of the adduct binding energy. We used this method here to build on the work in Jenks et al. (2023). We observed the same trend in which the less functionalized compounds dissociated at lower voltages (collision energies) than the more functionalized compounds. This is shown in Figure 3.14 for each of the monoterpene oxidation experiments, where the changes in iodide adduct signals are shown as a function of the voltage difference between the skimmer and quadrupole ion guide located between the ion-molecule reactor and mass analyzer.

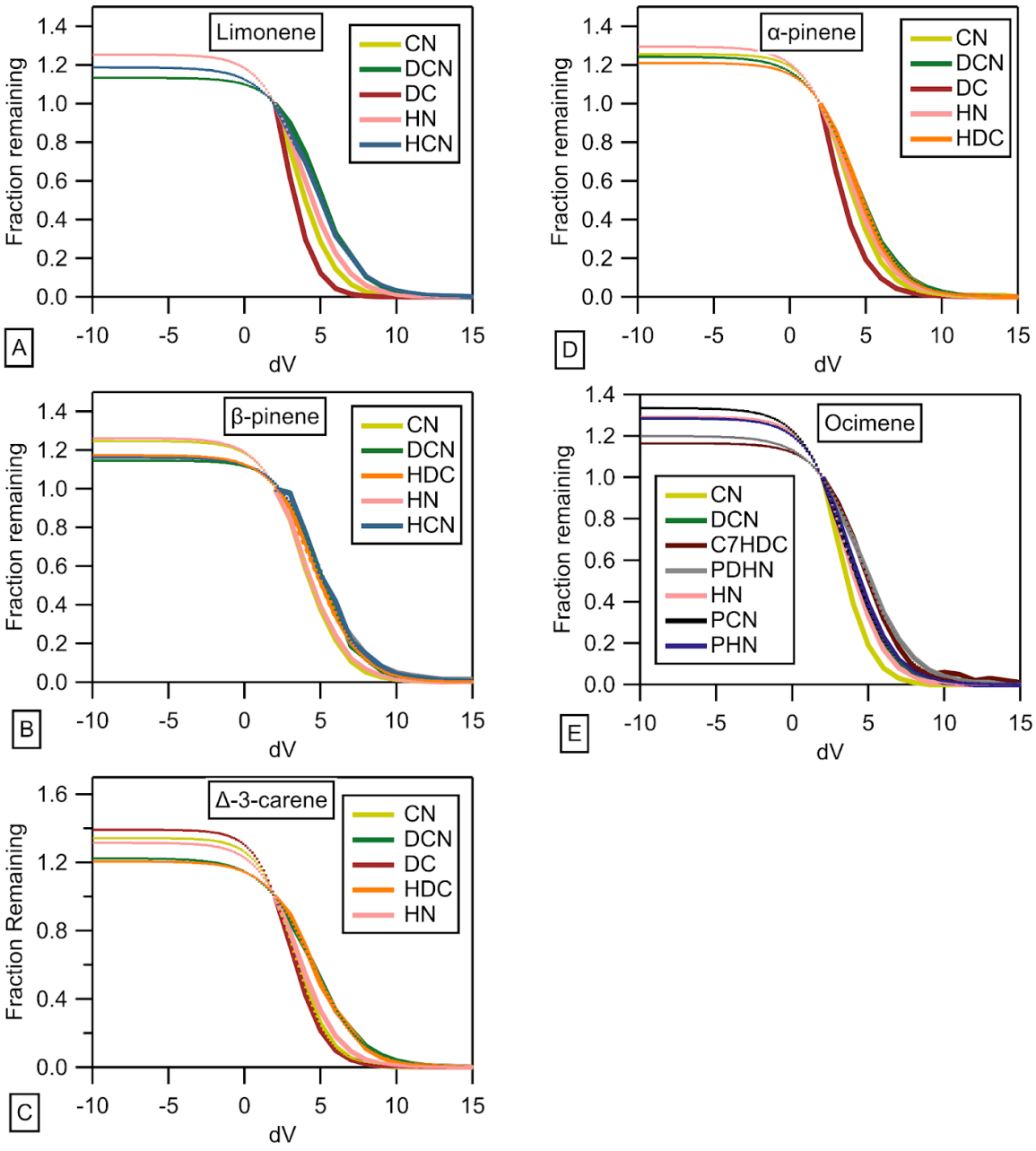

Figure 3.14 Results from voltage-scanning experiments on the products of the NO_3 + monoterpenes limonene (A), β-pinene (B), Δ-3-carene (C), α-pinene (D), ocimene (E), reactions. Changes in iodide adduct signals were measured by the iodide CIMS as a function of the voltage difference between the skimmer and quadrupole ion guide located between the ion-molecule reactor and mass analyzer.

The sigmoidal fit of the declustering scan curve is used to determine S_0 (the inverse of the amplitude of the fit) and dV_{50} (the inflection point of the fit). Figure 3.15 shows S_0 as a function of dV_{50} for all product ions measured by the iodide CIMS. This is similar to the results shown in Lopez-Hilfiker et al. (2016).

Figure 6 shows that the same product type from different precursors falls into a similar region in the diagram. For example, most DC products are at the lower end of the dV_{50} range, meaning that they form the weakest bound clusters with iodide. In contrast, most DCN products are at the higher end of the dV_{50} range, meaning they form the strongest bound clusters with iodide. However, even within one class of products, there is still quite a range in dV_{50} values. One might have hoped that the number and type of functional groups of these products could be used to parameterize instrument sensitivities. These results suggest that such an analysis only constrain sensitivities to within an order of magnitude or so.

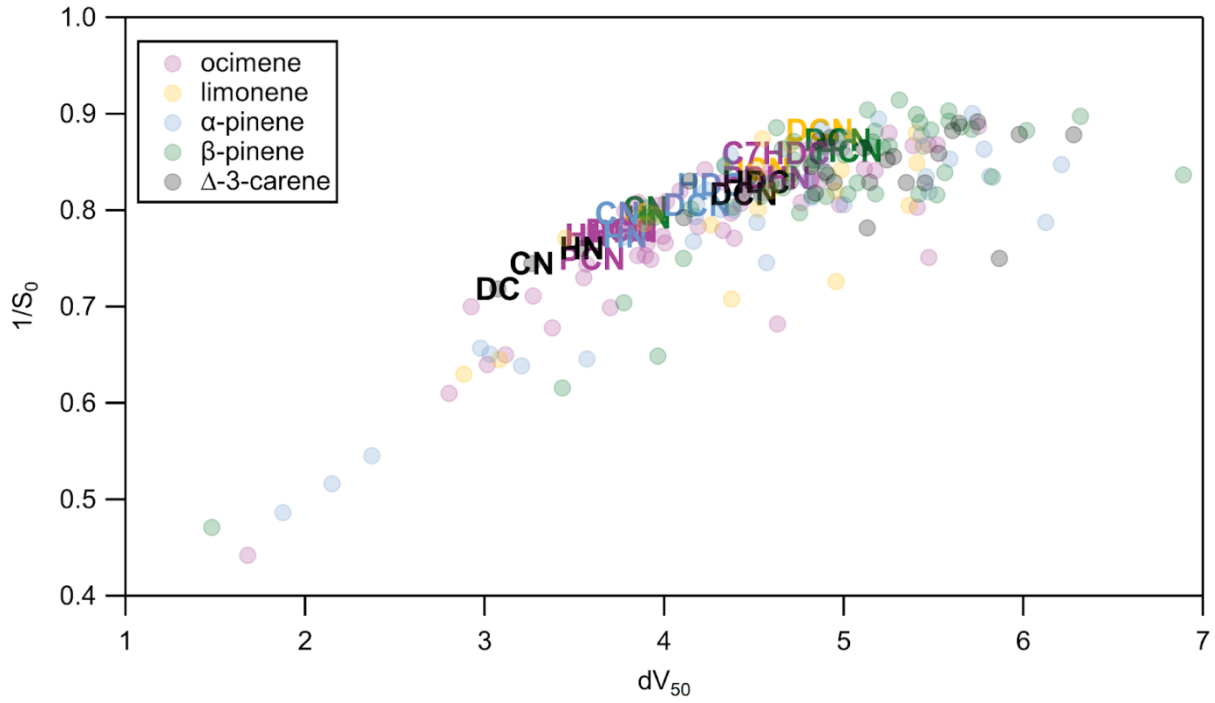

Figure 3.15 Results from voltage-scanning experiments on the products of the NO_3 + monoterpenes Δ-3-carene (black), α-pinene (blue), ocimene (purple), limonene (yellow), and β-pinene (green) reactions. Changes in iodide adduct signals were measured by the iodide CIMS as a function of the voltage difference between the skimmer and quadrupole ion guide located between the ion-molecule reactor and mass analyzer.

3.3.5. Comparison to Ambient Measurements.

VOC measurements were conducted in Pasadena, California, during the summer of 2022 as a part of the CalNext-2022 campaign. This is a good location to study the interaction of biogenic and anthropogenic emissions, due to the urban environment densely populated with trees. The conditions for these ambient measurements differed significantly from those in the laboratory. In the lab, the oxidation process was limited to the examination of first-generation products, with a single injection of monoterpene and oxidant. In the real atmosphere, continued reactions of monoterpene oxidation products with NO_3 can occur. Additionally, in ambient measurements variations existed in temperature, humidity, aerosol loading, and the presence of other species.

Unlike the lab setting where only one monoterpene was studied at a time, the ambient measurements involved a mixture of monoterpenes. However, despite these disparities, a broad comparison between the measurements can still be made.

Many of the monoterpene oxidation product ions measured in the lab were also detected in these ambient measurements. The diurnal variation of the monoterpene and monoterpene oxidation products is shown in Figure 7A. Monoterpenes are emitted and oxidized during the day and at night. Nighttime emissions are lower because of lower ambient temperatures, but not zero as in the case of isoprene, which emissions are also light-dependent. Because of the slower nighttime oxidation process and the lower boundary layers, the mixing ratios of monoterpenes are often higher during the nighttime compared to the daytime. Additionally, Volatile Chemical Products (VCPs) are a significant source of monoterpene anthropogenic emissions and can also occur at night (Gkatzelis et al., 2021). As the focus of this work was nighttime chemistry, the analysis will be on the average signals of these ions at 3 AM (local time).

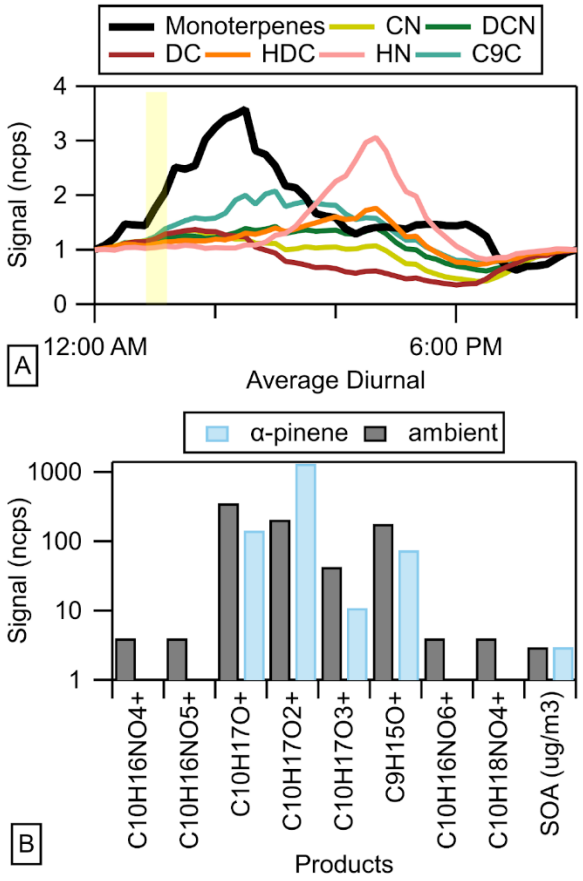

Figure 3.16 Diurnal of monoterpene and oxidation products measured by the Vocus during the ambient measurements in Los Angeles during the summer of 2022 (A) and product signal comparison between ambient measurements and α-pinene lab experiments (B).

The diurnal variations of the monoterpenes and some of the monoterpene product ions detected in the laboratory are shown in Figure 7A. While the ambient measurements encompass a blend of various monoterpenes and their oxidation products, the signals align most closely with laboratory signals derived from α-pinene. This observation suggests that α-pinene might dominate among the monoterpenes present in the ambient measurements. α-Pinene is typically the most abundant emission from vegetation. The a-pinene reaction rate with NO_3 is a little bit lower than that of limonene and carene, but faster than that of β-pinene. In combination these facts rationalize that the observed monoterpene products most resemble those of α-pinene. The signal of ions

detected in both ambient (detected at 3 AM local time) and α-pinene laboratory measurements are shown in Figure 7B. In addition to the gas-phase products formed by monoterpenes in ambient air, SOA is also formed. The amount of SOA for ambient measurements is predicted from the SOA yields reported in DeVault et al. (2022). The average ratio of the gas-phase ion signals shown in Figure 7B, and the ambient signals were increased proportionally for comparison. The agreement is not perfect, and that is likely due to other monoterpenes and their oxidation products contributing to the ambient signals, as well as the difference in conditions as mentioned above.

3.4. Conclusions

This work describes the gas-phase products, yields, and mechanism of the reaction of five monoterpenes, Δ-3-carene, α-pinene, β-pinene, ocimene, and limonene, with NO_3 radicals. The gas-phase products were measured by the Vocus and iodide CIMS and were found to consist of multifunctional compounds containing ketone, aldehyde, alcohol, carboxylic acid, peroxide, epoxide, and nitrate functional groups.

The iodide CIMS was used as a valuable tool for identifying parent ions, while the Vocus facilitated the quantification of gas-phase products. Tubing delay experiments proved instrumental in identifying ion fragments within the Vocus, enhancing the precision of gas-phase product yield assessments. The integration of the voltage scanning technique confirmed that more functionalized monoterpene oxidation products are more strongly bound to the iodide adduct, which could be used to develop a structure-activity relationship to predict iodide CIMS sensitivity in the future.

Several of the ions derived from monoterpene oxidation products observed in the laboratory are also identified in the ambient measurements. A comparison between the measurements showed that the ambient measurements are most similar to the laboratory measurements of α-pinene, suggesting the dominant monoterpene during these measurements was α-pinene.

The oxidation of monoterpenes by NO_3 radicals contributes to a deeper comprehension of the atmospheric fate of monoterpenes and their resultant reaction products, notably organic nitrates. These findings are anticipated to offer valuable insights for deciphering field data and refining chemical models. Future work will explore the gas-phase products of monoterpene OH oxidation in the lab and in the field.

Gas-Phase Products of OH Radical Oxidation of Five Monoterpenes

4.1. Introduction

Worldwide, approximately 150 teragrams of monoterpenes are released into the atmosphere annually, comprising α-pinene, ocimene, β-pinene, limonene, sabinene, Δ-3-carene, and myrcene (Sindelarova et al., 2014; Guenther et al., 2012). Following their release, these monoterpenes undergo rapid oxidation, leading to the formation of less volatile compounds that can distribute into the particle phase, which can have adverse health effects on humans and the ecosystem. Reactions of monoterpenes with OH radicals in high NOx conditions in the day and NO_3 radicals at night can also lead to the formation of organic nitrates (ON) (Perring et al., 2013). The process of generating organic nitrates from monoterpene oxidation by OH radicals in environments with elevated NOx levels has been studied extensively (Sakamoto et al., 2022; Liebmann et al., 2019; Fisher et al., 2016; Morales et al., 2021; DeVault et al., 2022). These products are an important sink for nitrogen in the atmosphere (Browne and Cohen, 2012; Pusede et al., 2015). ON can partition into the particle phase, which affects climate and air quality (Hallquist et al., 2009; Rollins et al., 2012; Biesenthal et al., 1997; Fry et al., 2009; Perraud et al., 2012). This underscores how anthropogenic nitrogen oxide emissions influence the production of secondary organic aerosols (SOA) from the oxidation of biogenic volatile organic compounds (BVOCs).

In this study, our focus was on examining the initial generation of gas-phase products resulting from the OH radical oxidation of five key monoterpenes: Δ-3-carene, α-pinene, β-pinene, ocimene, and limonene. These monoterpenes collectively represent approximately 90% of global monoterpene emissions. To investigate these reactions, experiments were conducted in an environmental chamber, employing trace-gas measurements with both a Vocus and iodide CIMS.

Following an exploration of the reaction mechanisms, we applied the voltage scanning method, as outlined by Lopez-Hilfiker et al. (2016), to assess the sensitivity of the iodide CIMS towards these reaction products. This research builds upon prior investigations focusing on particle-phase measurements, SOA yields, and provides a more comprehensive examination of the gas-phase yields resulting from monoterpene oxidation by nitrate radicals, as documented in previous studies.

4.2. Experimental

4.2.1. Chemicals

The following chemicals with purities and suppliers were used: (1s)-(+)-3-carene (99%) and ocimene (90%) from Sigma Aldrich; (1R)-(+)-α-pinene (99%), (1S)-(-)-β-pinene (99%), (R)-(+)-limonene (97%), 2-ethylhexyl nitrate (97%), from Aldrich Chemical Company; NO from Matheson Tri Gas; ultra-high purity (UHP) N_2 from Airgas; and a standard mixture (methanol, acetonitrile, acetaldehyde, acetone, acrylonitrile, isoprene, 2-butanone, benzene, toluene, m-xylene, 1,2,4-trimethylbenzene, α-pinene, and β-caryophyllene in N_2) from Apel-Riemer. Methyl nitrite was synthesized following the procedure described by Taylor et al. (1980).

4.2.2. Chamber Experiments

Chamber experiments were carried out in a Teflon environmental chamber equipped with lights on two opposite walls and a volume of approximately 7 m^3, maintained at room temperature (~23 °C) and pressure (~630 Torr). The chamber was supplied with clean, dry air from two AADCO pure air generators, ensuring minimal levels of hydrocarbons (<5 ppbv) and low relative humidity (<1%). The monoterpene, methyl nitrite, and NO were introduced individually into the chamber via a glass bulb, with the monoterpene subjected to mild heating, to achieve target concentrations of approximately 500, 250, and 250 ppbv, respectively. Following the addition of each chemical, a Teflon-coated fan was activated for 30 seconds to ensure complete mixing within

the chamber. OH radicals were formed by photolysis (J_{NO2} = 0.19 min^{-1}) of methyl nitrite by the following reactions:

$$CH_3ONO + hv \rightarrow CH_3O + NO \quad (4.1)$$

$$CH_3O + O_2 \rightarrow CH_2O + HO_2 \quad (4.2)$$

$$HO_2 + NO \rightarrow OH + NO_2 \quad (4.3)$$

The introduction of NO served to ensure the exclusive interaction of $RO_2\cdot$ radicals with NO, thereby enhancing the conversion of HO_2 to OH radicals, while also preventing the formation of O_3 and NO_3 radicals. Under these conditions, the majority of NO_3 radicals reacted with the monoterpene to form predominantly first-generation products. The lights were turned on for 75-250 s, when ~50% of the monoterpene had reacted.

4.2.3. Instrumentation

Monoterpene and monoterpene oxidation products were measured using a Vocus 2R proton-transfer-reaction time-of-flight mass spectrometer (Vocus), manufactured by Tofwerk AG in collaboration with Aerodyne Research Inc., with a 2-meter Teflon sample line, operating at a flow rate of approximately 2 L min^{-1} (LPM). Data acquisition with the Vocus occurred at a frequency of 1 Hz. Calibration of the Vocus was performed using a standard gas mixture comprising various VOCs, including methanol, acetonitrile, acetaldehyde, acetone, acrylonitrile, isoprene, 2-butanone, benzene, toluene, m-xylene, 1,2,4-trimethylbenzene, α-pinene, and β-caryophyllene, each at a concentration of approximately 1 ppm in nitrogen (Apel-Riemer). The sigmoidal transmission curve from these calibrations is shown in Figure 4.1

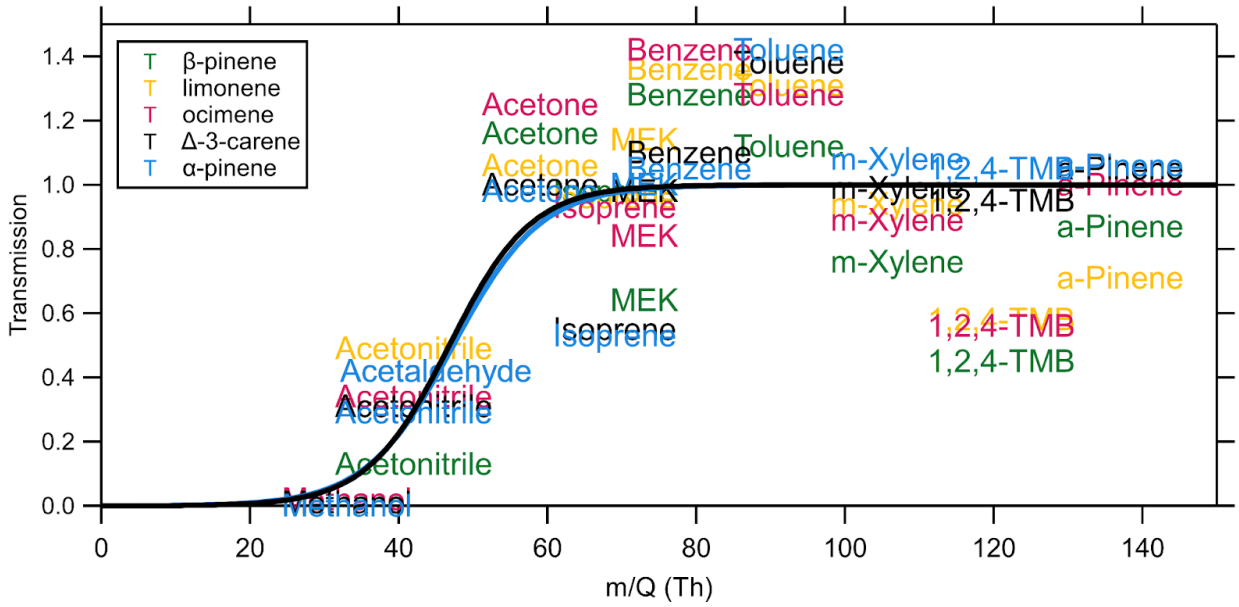

Figure 4.1 The sigmoidal transmission fit of calibration standards for five experiments measured by the Vocus assuming a base of zero.

For VOCs not present in this mixture, sensitivities were estimated using established methodologies outlined in Jenks et al., 2023.

An iodide chemical ionization mass spectrometer (iodide CIMS) comprises a radioactive source generating I^- reagent ions from CH_3I. Operating with a time resolution of 1 s, the iodide CIMS achieved an average mass resolution ($m/\Delta m$) of approximately 9,200 at m/z 275. Although no calibrations were conducted for this instrument, the collected data solely served for identifying reaction products. Nevertheless, any signal fluctuations resulting from variations in iodide concentration were adjusted by normalizing product ion signals against the iodide and iodide water cluster ion signals.

4.2.4. Data Processing

Data processing was conducted using Tofware (v3.2.3, www.tofwerk.com/tofware) within the Igor Pro 8 environment (Wavemetrics, OR, USA). Formulas for peaks were manually assigned,

followed by the calculation of their time series using peak shape fitting. Background measurements were taken from the clean chamber immediately before introducing the monoterpene. Iodide CIMS data were normalized to $I^- + I \cdot H_2O^-$, denoted by the units of normalized counts per second (ncps). Mass-to-charge ratio calibration was executed resulting in an average accuracy of approximately 4 ppm for the Vocus and 3 ppm for the iodide CIMS.

4.3. Results and Discussion

4.3.1. Reaction Mechanism

The mechanisms for the reaction between monoterpenes and OH have been described elsewhere (Morales et al., 2021; DeVault et al., 2022; D'Ambro et al., 2022; Hantscheke et al., 2021; Baptista et al., 2014; Peeters et al., 2001; Lee et al., 2023; Piletic and Kleindienst, 2022; Capouet et al., 2004; Vereecken and Peeters, 2000; Davis and Stevens, 2005; Hatakeyama et al., 1991; Kaminski et al., 2017; Du and Zhang, 2023; Pang et al., 2022; Li et al 2020; Atkinson and Arey 2003; Lee et al., 2006). Figure 4.2 illustrates a summary mechanism that is the most relevant for the work described here.

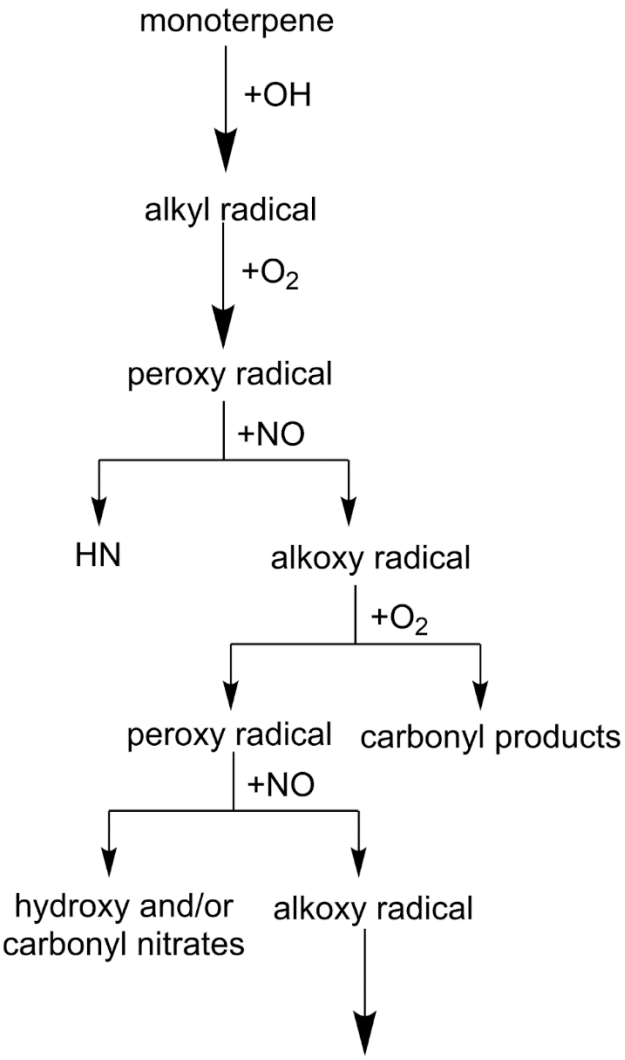

Figure 4.2 The proposed gas-phase reaction mechanism for the oxidation of monoterpenes by OH radicals.

In the first step, a hydroxyl group is added to a C=C bond in the monoterpene to form an alkyl radical. Oxygen then rapidly adds to the alkyl radical to form a peroxy radical. The peroxy radical then reacts with NO to form a hydroxy nitrate (HN). This step can also form an alkoxy radical, which can add O_2 forming carbonyl products. The alkoxy radical can also go on to propagate another peroxy radical after the addition of O_2, which will go on to form more oxygenated species like hydroxy and/or carbonyl nitrates. Figures 4.3-4.7 show more extensive proposed reaction mechanisms for each of these monoterpenes.

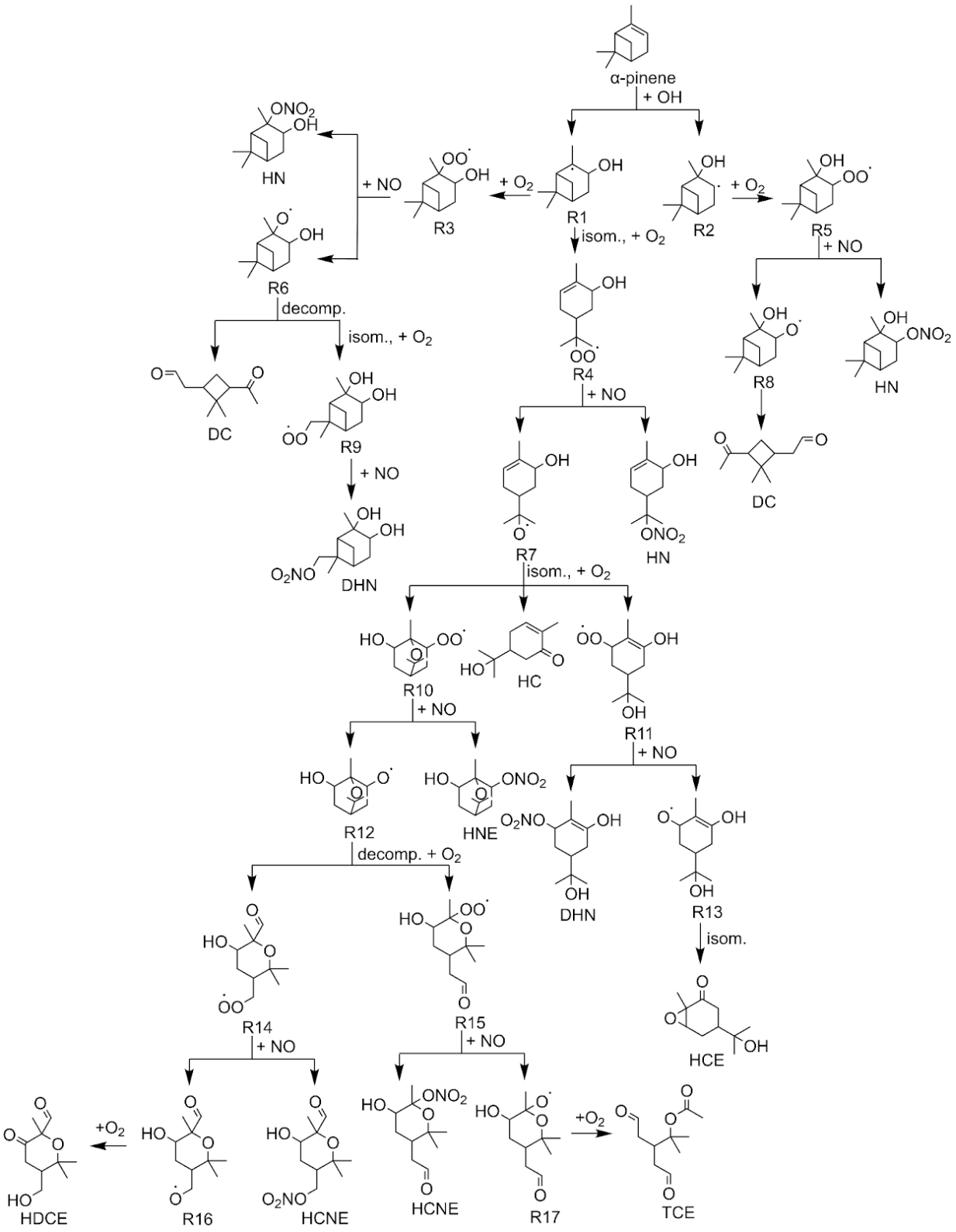

Figure 4.3 Proposed gas-phase reaction mechanism for the oxidation of α-pinene by NO_3 radicals.

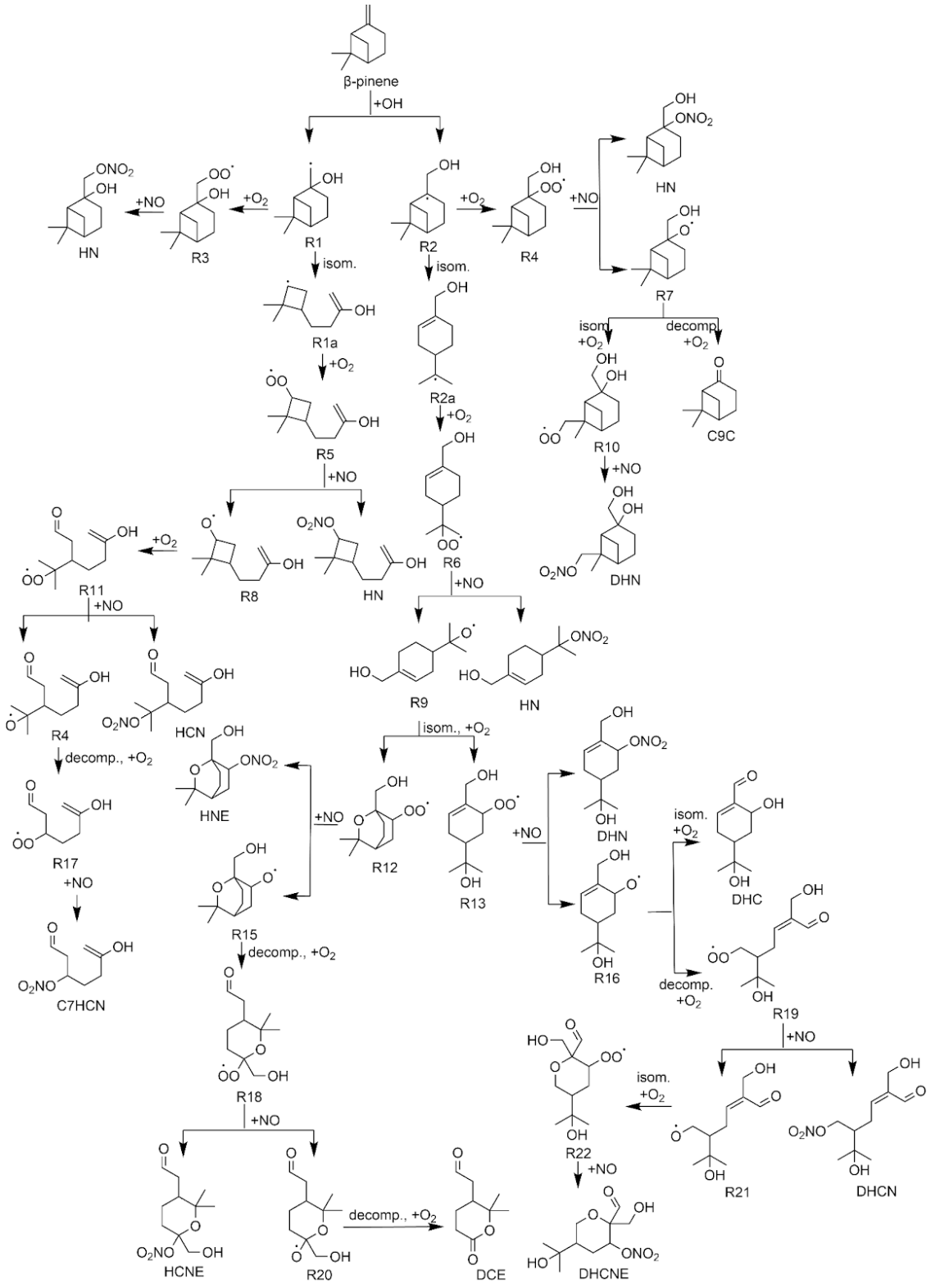

Figure 4.4 Proposed gas-phase reaction mechanism for the oxidation of β-pinene by NO_3 radicals.

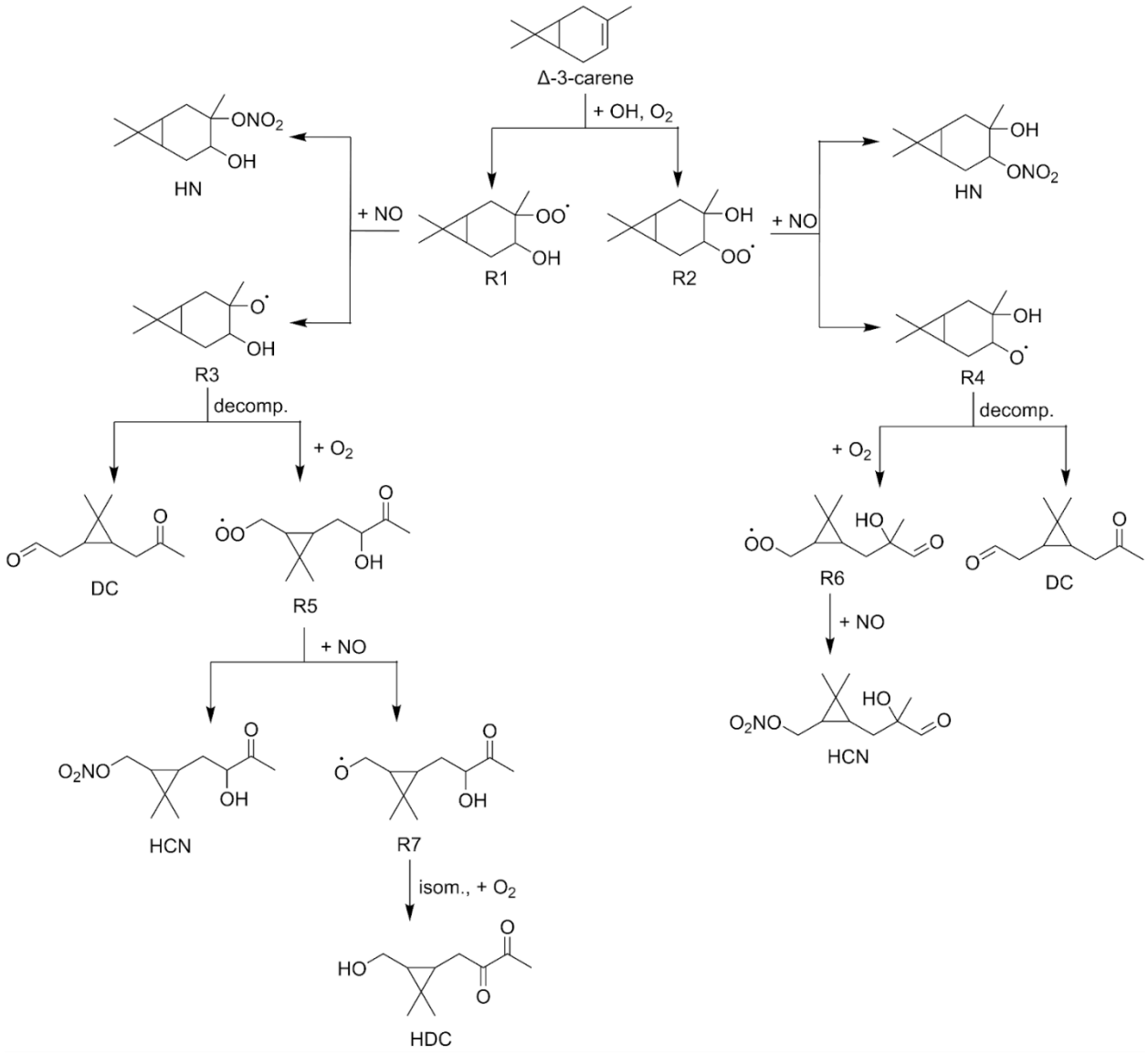

Figure 4.5 Proposed gas-phase reaction mechanism for the oxidation of Δ-3-carene by NO_3 radicals.

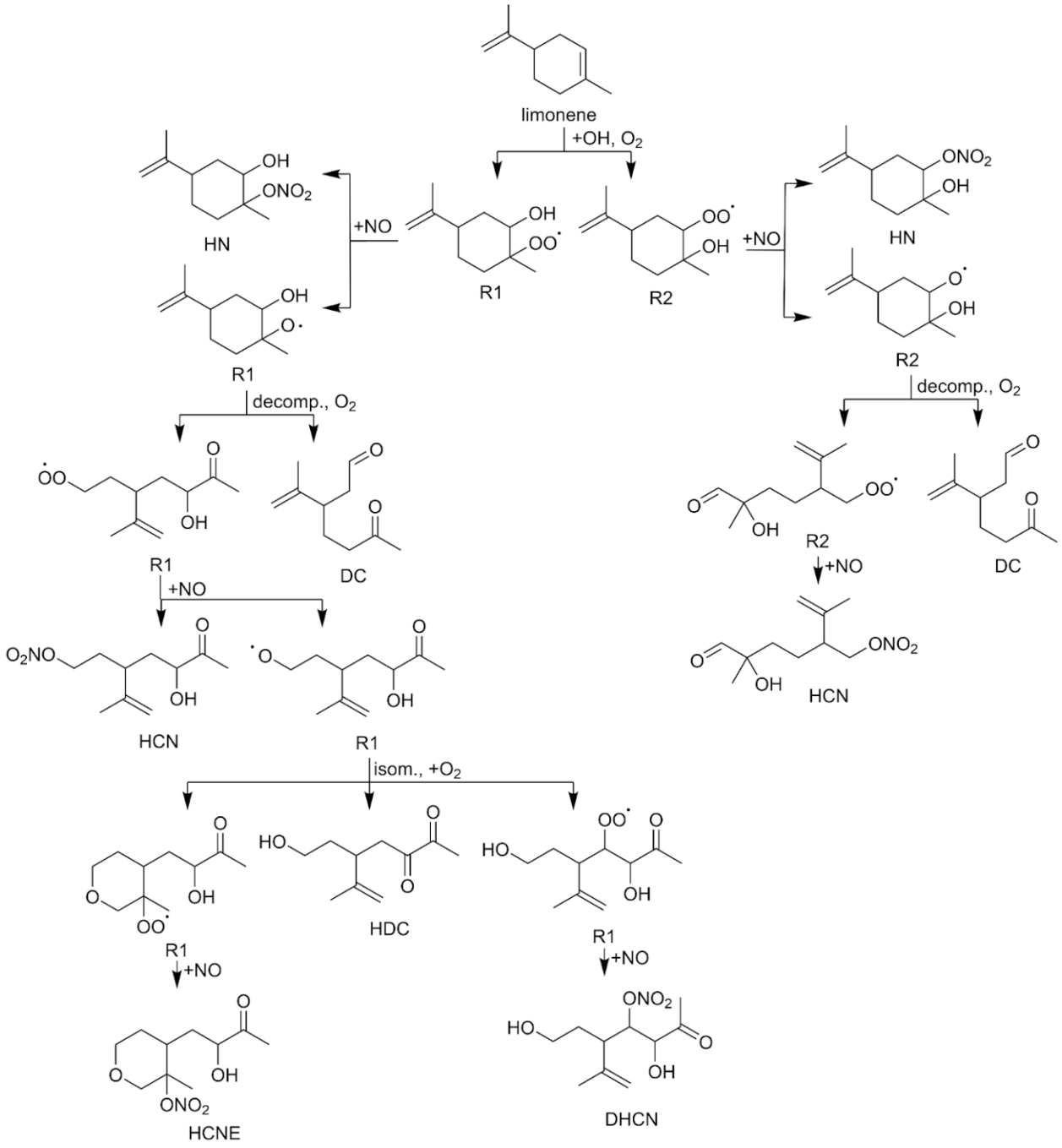

Figure 4.6 Proposed gas-phase reaction mechanism for the oxidation of limonene by NO_3 radicals.

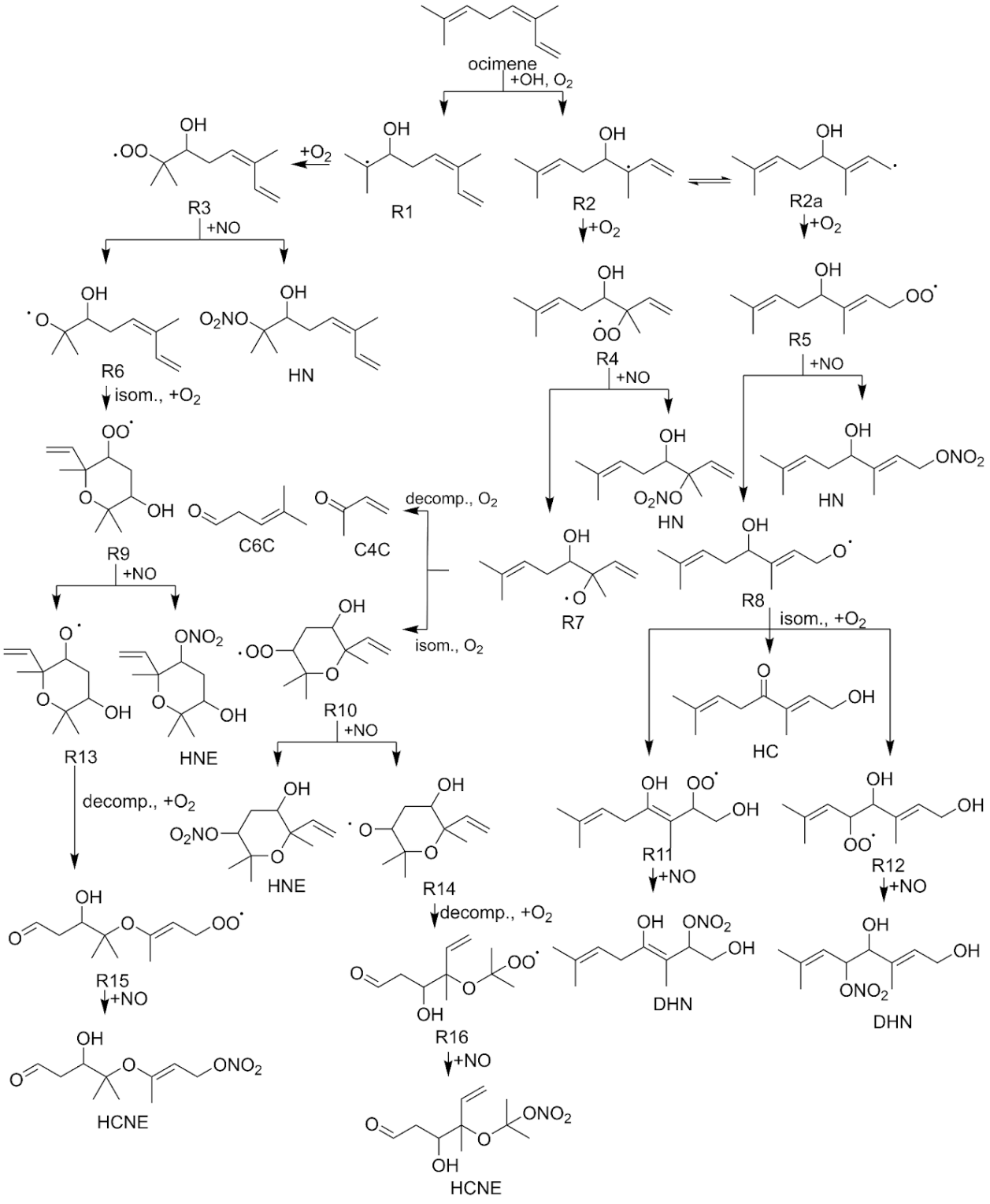

Figure 4.7 Proposed gas-phase reaction mechanism for the oxidation of ocimene by NO_3 radicals.

4.3.2. Time Series Measurements and Mass Spectra

Figure 4.8 illustrates the time series data for the five monoterpenes, NO_3, and several gas-phase oxidation products detected by the Vocus (Figure 1A-E) and by the iodide CIMS (Figure 1F-J) observed in each experiment. The reactions were initiated by turning on the UV lights to form OH radicals. Within less than 5 minutes, about half of the monoterpene had reacted and the lights were shut off. The iodide CIMS time series depicts the increase in products such as HN, HCN, DHN, DHC, and DC. Similarly, the Vocus time series demonstrates a decrease in monoterpene signal by approximately 40%, coupled with an increase in products like DC, C9C, and HC.

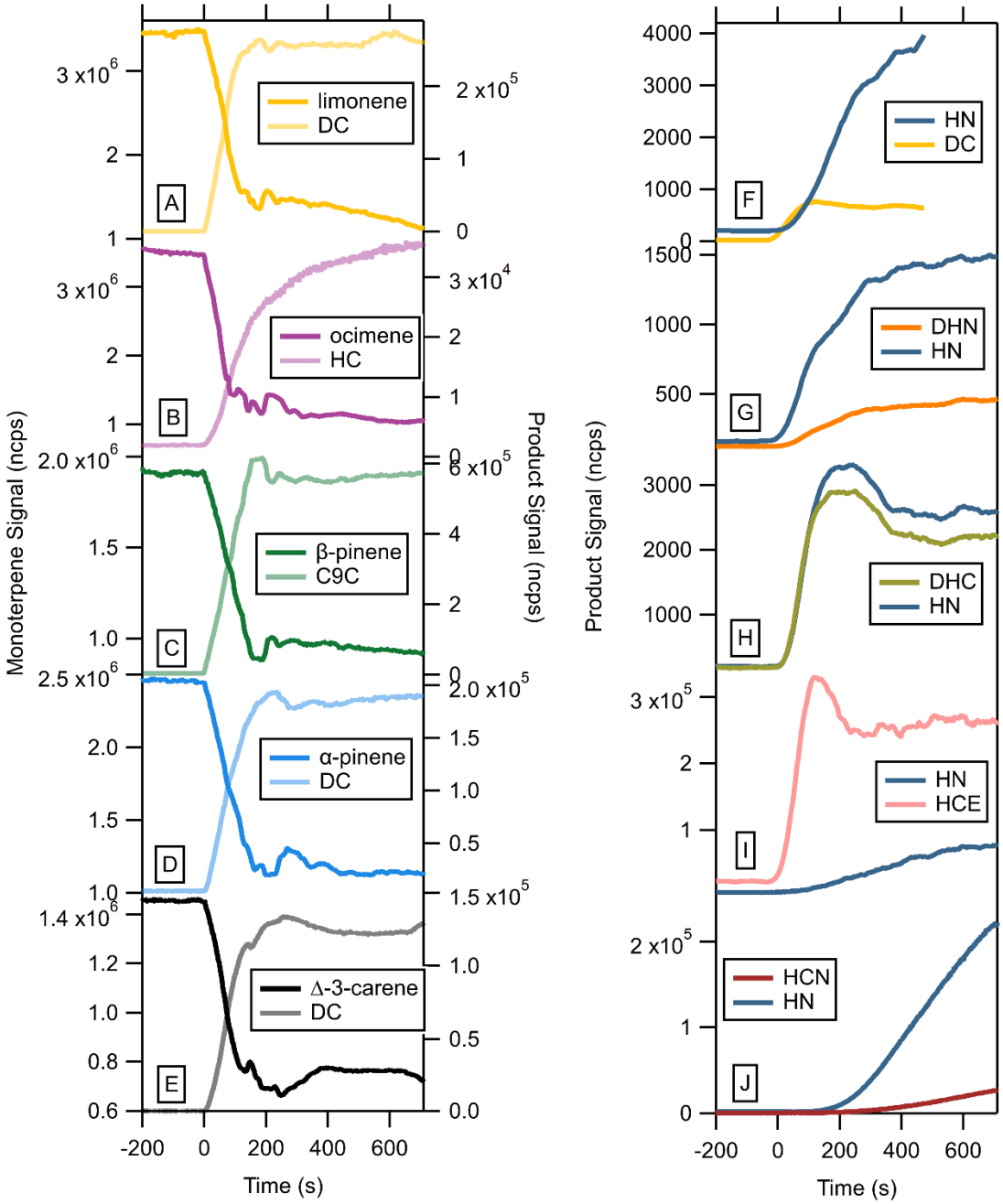

Figure 4.8 (A-E) Time series of ocimene, α-pinene, limonene, Δ-3-carene, and β-pinene and a carbonyl oxidation product for each monoterpene detected by the Vocus. (F-J) Time series of a few products detected by the iodide CIMS.

Figures 4.9 and 4.10 present the mass spectra of the oxidation products detected by the Vocus and the iodide CIMS, respectively. The Vocus mass spectra reveal similarities among all

five monoterpenes, with the carbonyl product labeled. A C9 carbonyl is formed from β-pinene, a hydroxy carbonyl is formed from ocimene, and a dicarbonyl is formed from limonene, Δ-3-carene, and α-pinene.

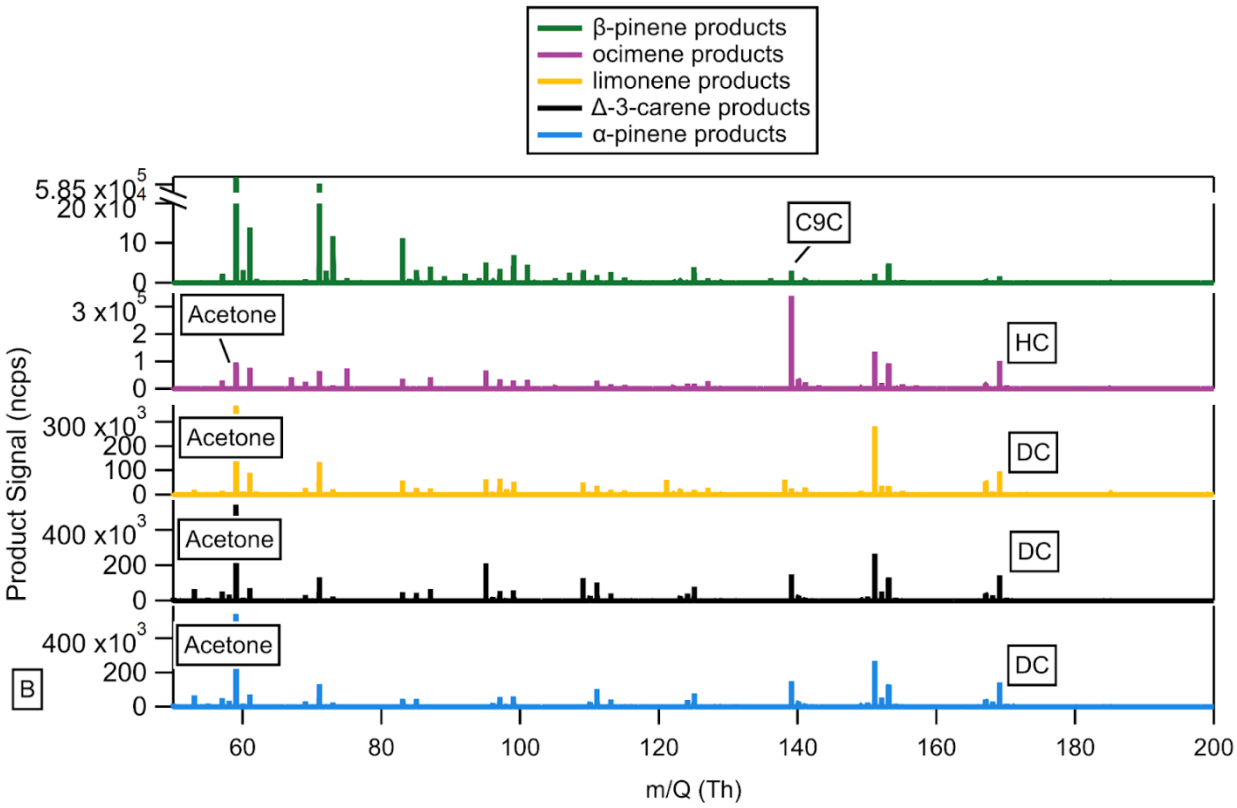

Figure 4.9 Vocus mass spectra of the products detected from the reaction of ocimene (purple), α-pinene (blue), limonene (yellow), Δ-3-carene (black), and β-pinene (green) by OH radicals.

The iodide CIMS mass spectrum showcases resemblances among all monoterpenes in the formation of a hydroxy nitrate. A dihydroxy nitrate or hydroxy carbonyl nitrate is detected in the mass spectra of ocimene, α-pinene, Δ-3-carene, and β-pinene.

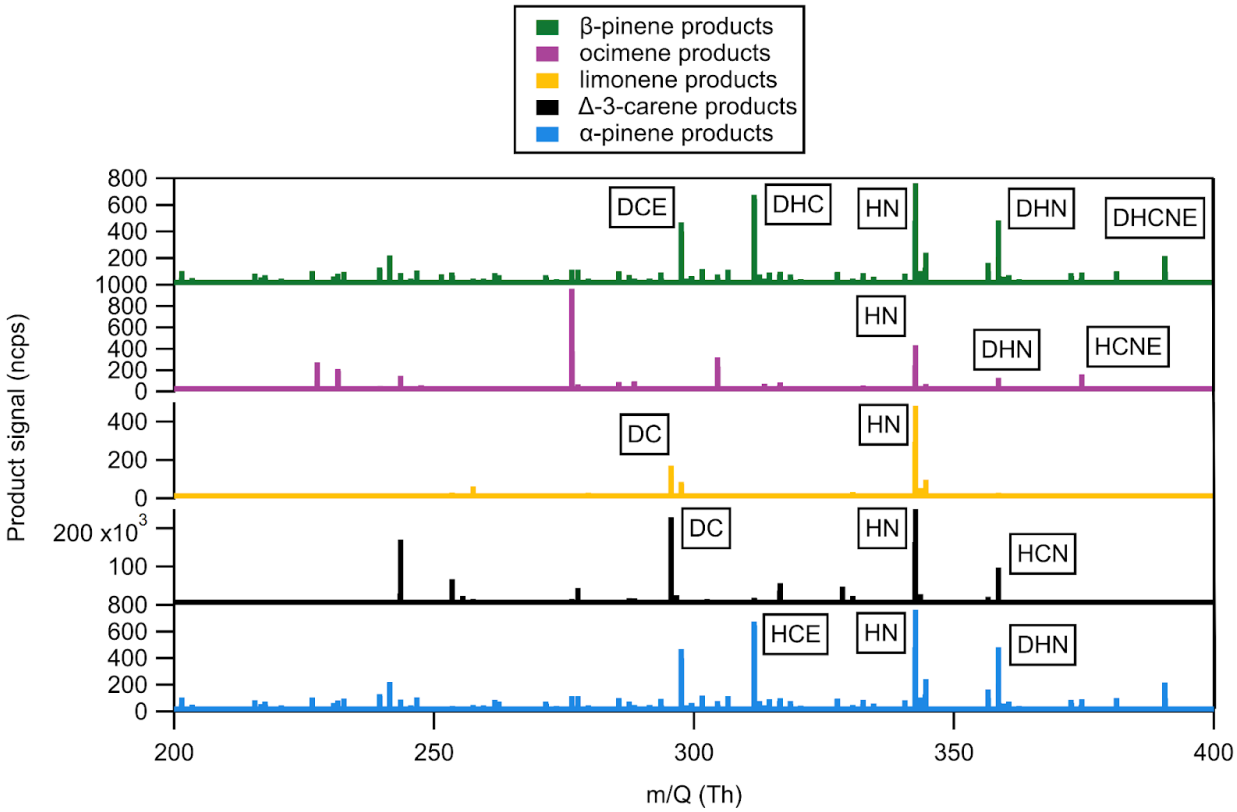

Figure 4.10 Iodide CIMS mass spectra of the products detected from the reaction of ocimene (purple), α-pinene (blue), limonene (yellow), Δ-3-carene (black), and β-pinene (green) by OH radicals.

4.3.3. Voltage Scanning

The oxidation products are detected using iodide CIMS with minimal or no fragmentation, enabling the identification of products and assessment of reaction mechanisms. However, quantifying product yields through iodide CIMS proves challenging due to significant variations in sensitivity among different compounds. Instrument sensitivities have been approximated using a "voltage scanning" technique as outlined by Lopez-Hilfiker et al. (2016), which estimates the bond strengths of iodide-product adducts. As the voltage difference between the skimmer and the BSQ increases in the iodide CIMS, so does the collision energy, allowing adducts to dissociate into I^- and a neutral molecule based on the strength of the adduct binding energy. We employed

this method to expand upon the research by Jenks et al. (2023). The same pattern is observed: less functionalized compounds dissociate at lower voltages (collision energies) compared to more functionalized compounds. The sigmoidal fit of the declustering scan curve determines S_0 (the amplitude of the fit) and dV_{50} (the inflection point of the fit), which is shown for all product ions measured by iodide CIMS, resembling findings from Hilfiker et al. (2016).

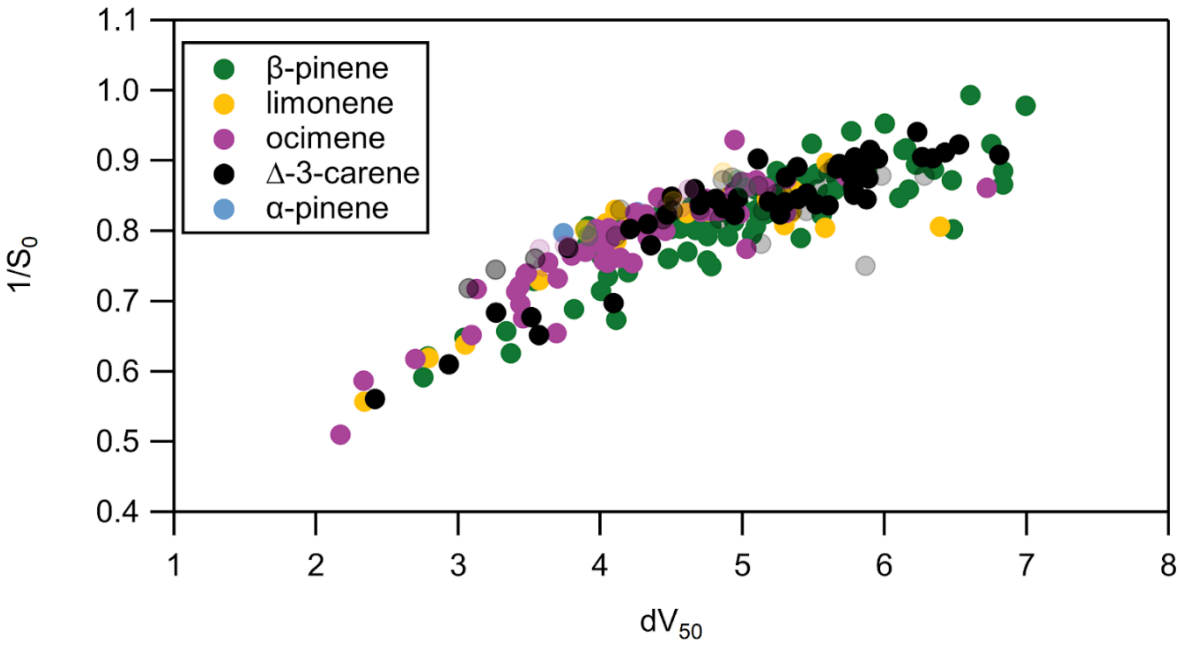

Figure 4.11 Results from voltage-scanning experiments on the products of the OH + monoterpene (opaque markers) and NO_3 + monoterpene (transparent markers) from Jenks et al., (2024). Changes in iodide adduct signals were measured by the iodide CIMS as a function of the voltage difference between the skimmer and quadrupole ion guide located between the ion-molecule reactor and mass analyzer.

Products of the same type from different precursors fall within a similar region on the diagram. For instance, most of the less-functionalized products cluster towards the lower end of the dV_{50} range, indicating weaker binding with iodide, whereas most of the more-functionalized products cluster towards the higher end, indicating stronger binding. Nonetheless, even within one product class, there remains a considerable range in dV50 values. While it might be expected that

the number and nature of functional groups in these products could parameterize instrument sensitivities, these results suggest that such an analysis only constrains sensitivities to within an order of magnitude or so.

4.4. Future Work and Conclusions

This study investigates the reaction mechanisms and gas-phase oxidation products resulting from the OH radical oxidation of five monoterpenes. Time series data and mass spectra were analyzed to understand the composition of the oxidation products. The mass spectra indicate similarities among the monoterpenes in the formation of certain oxidation products, such as carbonyl compounds and hydroxy nitrates. Voltage scanning techniques are employed to assess the sensitivity of the iodide CIMS instrument, revealing variations in sensitivity among different compounds by the number of functional groups. Overall, the findings contribute to a deeper understanding of monoterpene oxidation mechanisms and the challenges associated with quantifying product yields. Future work will compare these results to the ambient measurements from the Cal-Next-2022 field campaign in Pasadena, California.

Effects of Germicidal Ultraviolet Light on Aerosol Formation from Limonene

5.1. Introduction

Since the mid-1800s it has been known that light affects microorganisms, and germicidal ultraviolet (GUV), also known as ultraviolet germicidal irradiation (UVGI) has been used to inactivate airborne microbes since the early 1900s (Reed, 2010). GUV light fixtures have been installed in hospitals to decrease postoperative wound infections and prevent the spread of tuberculosis and influenza, as well as in schools to prevent the transmission of measles (Hart, 1960; Wells, 1942; McLean, 1961; Riley et al., 1959). The use of GUV decreased in the mid-1900s partially due to the development of antibiotics and immunizations, and due to the perceived low importance of airborne transmission (Reed, 2010; Jimenez et al., 2022). Recently, there has been renewed interest in GUV for air disinfection because of the COVID-19 pandemic, for which airborne transmission was found to be important (Jimenez et al., 2022; Greenhalgh et al., 2021). Studies have shown that UV lamps at 254 nm (GUV254) and 222 nm (GUV222) are effective in inactivating SARS-CoV-2 (Ma et al., 2021; Camargo et al., 2022).

One limitation of using 254 nm UV (GUV254) fixtures for air disinfection is that they are not safe for human exposure, so they are usually either mounted near the ceiling for upper room irradiation, or are used inside ventilation ducts (Talbot et al., 2002; Nardell et al., 2008). Studies have shown that 222 nm lamps can be used for whole-room disinfection to inactivate airborne bacteria and viruses without harm to human skin and eyes (Buonanno et al., 2017; Narita et al., 2018; Peng et al., 2023b). However, it has also been shown that GUV222 forms substantial ozone, which can react further in the indoor environment to form harmful pollutants like formaldehyde and $PM_{2.5}$ (Peng et al., 2023b; Barber et al., 2023; Link et al., 2023).

Given that the majority of people in the developed world spend a large fraction of their time indoors, ensuring good indoor air quality is crucial for promoting overall health and well-being

(Klepeis et al., 2001). Volatile organic compounds (VOCs) can be emitted from many sources indoors including cleaning products, paint, furniture, and humans (McDonald et al., 2018; Stönner et al., 2018). Some of these VOCs, like formaldehyde are known to have negative health effects (Bernstein et al., 2008; Weschler, 2009). Some compounds undergo reactions to produce hazardous products like secondary organic aerosol (SOA). For example, a study by Graeffe et al. showed that commercial GUV254 devices can increase particle number concentrations and gas-phase species concentrations in indoor air (Graeffe et al., 2023).

This work evaluates the effects of GUV222 on the chemistry of limonene and limonene oxidation products. Limonene, a common fragrance ingredient in personal care and cleaning products, is one of the most common VOCs in indoor air (Stönner et al., 2018; Logue et al, 2011). Limonene is also highly reactive with hydroxyl (OH), ozone (O_3) and nitrate (NO_3). Ozone, a common indoor pollutant, comes from outdoor air, can be enhanced by GUV222 and reacts with VOCs like limonene (Weschler et al., 1989). Limonene ozonolysis can be a significant source of particulate matter (PM) indoors and can also form gas-phase products such as formaldehyde and glyoxal (Weschler et al., 1999; Grosjean et al., 1992; Wainman et al., 2000). While limonene ozonolysis has been studied in detail, the question we focus on here is whether the formation of products is modified by the presence of GUV222. For example, photolysis could potentially remove limonene oxidation products with carbonyl and acid groups and thereby lower (SOA) yields (Deal and Vaida, 2023).

In this paper, we study the chemistry of limonene induced by GUV222 in an environmental chamber. We address how well a commonly used chemical mechanism, the Regional Atmospheric Chemistry Mechanism (RACM), with modifications that account for SOA formation and wall loss in a chamber, predicts limonene removal and SOA formation under the experimental conditions

used in the chamber (Stockwell et al., 1997). We then analyze in detail if the 222 nm light impacts the formation of gas-phase and particle-phase oxidation products. This work builds on previous studies that focused on the formation of O_3 by GUV222 and the modeling of that formation (Peng et al., 2023a; Peng et al., 2023b).

5.2. Methods

5.2.1. Chamber Experiments.

Chamber experiments were conducted in a ~21 m^3 Teflon FEP chamber. Clean air was supplied to the chamber with AADCO 737-15A clean air generators (NO_x <0.2 ppb; VOC <50 ppb). An Ushio B1 KrCl excimer 222 nm lamp was placed inside the chamber, which has previously been shown to lead to rapid ozone formation (Peng et al., 2023b). Here, ~20 ppb ozone was produced in two steps of 30 min with 15 min in between. Liquid precursor (limonene and/or hexanal) was then evaporated into the chamber using a glass bulb under nitrogen flow to produce a ~20 ppb concentration. An experiment using α-pinene as the precursor was also performed. A Teflon-coated fan was run during these additions for about 2 minutes to ensure complete mixing in the chamber. The 222 nm lamp was turned on continuously for several hours or alternated in steps of 30 min on/off. Experiments were performed at ambient pressure (~830 mbar in Boulder, CO), room temperature (25-27 °C), and low (<1%) and moderate (~25%) RH. Experiment summaries are shown in Table 5.1 and Figure 5.1. Further details on the environmental chamber facility have been described in several previous publications (Peng et al., 2023b; Liu et al., 2019; Day et al., 2022; Krechmer et al., 2017).

Table 5.1 Experiment Summary.

Experiment	α-pinene dry	limonene dry	limonene humid	hexanal dry	hexanal humid	limonene + hexanal dry	limonene + hexanal humid
Instruments used	Vocus, SMPS, O_3 monitor	Vocus, SMPS, O_3 monitor, AMS	Vocus, SMPS, O_3 monitor	Vocus, SMPS, O_3 monitor	Vocus, SMPS, O_3 monitor	Vocus, SMPS, O_3 monitor, AMS	Vocus, SMPS, O_3 monitor, AMS
Initial monoterpene conc. (ppb)	17±2.0	17±2.0	17±2.0	N/A	N/A	16±2.0	18±2.0
Initial hexanal conc. (ppb)	N/A	N/A	N/A	22±2.0	22±2.0	23±2.0	21±2.0
O_3 conc. beginning - end (ppb)	20±0.9 - 54±1.0	22±0.71 - 52±0.65	20±0.82 - 64±0.63	28±0.79 - 96±1.0	12±0.92 - 58±0.95	17±0.65 - 48±0.91	20±0.84 - 46±0.52
O_3 prod. Rate when GUV222 on (ppb hr^{-1})[8]	26	25	25	26	24	21	23
RH (%)	-0.29±0.074	-0.30±0.075	26±0.18	0.05±0.1	25±0.16	0.1±0.07	27±0.17
Temp (°C)	29±0.095	27±0.17	28±0.12	25±0.28	25±0.11	27±0.46	26±0.14
Estimated GUV222 fluence rate (µW cm^{-2})	2.5	2.4	2.4	2.5	2.3	2.0	2.2
Max SOA concentration (µg m^{-3})	3.60±0.07	9.60±0.10	9.60±0.10	0.01±0.02	0.76±0.05	6.00±0.08	8.40±0.07

[8] Measured in the absence of limonene.

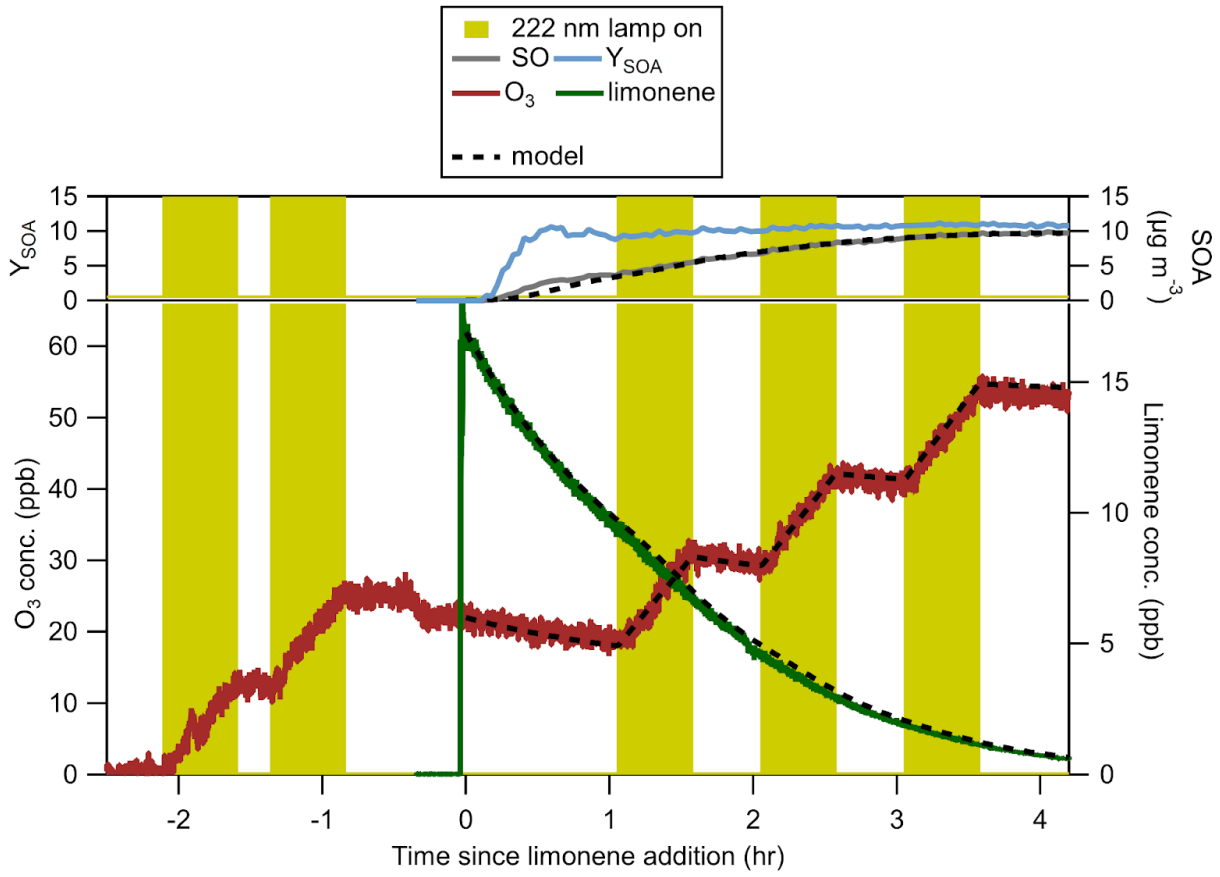

Figure 5.1 Modeled and experimental time series of limonene, ozone, and SOA mass concentration for an experiment under dry conditions.

5.2.2. Chemicals.

The following chemicals with purities and suppliers were used: (R)-(+)-limonene (97%) and hexanal (99%) from Aldrich Chemical Company; acetone (99%) from Sigma-Aldrich; ultra-high purity (UHP) N_2 from Airgas; and a standard gas mixture (methanol, acetonitrile, acetaldehyde, acetone, acrylonitrile, isoprene, 2-butanone, benzene, toluene, m-xylene, 1,2,4-trimethylbenzene, α-pinene, and β-caryophyllene in N_2) from Apel-Riemer to calibrate the Vocus proton-transfer-reaction time-of-flight mass spectrometer (see Instrumentation).

5.2.3. Instrumentation.

A Tofwerk AG and Aerodyne Research Inc. Vocus 2R proton-transfer-reaction time-of-flight mass spectrometer (Vocus) was used to measure VOCs, including limonene and its gas-phase ozonolysis products. A 2-m long Teflon sample line was used with a flow rate of ~2 LPM (0.635 cm OD, 0.397 cm ID). Vocus data were obtained at 1 Hz. The Vocus was calibrated using a standard gas mixture containing several VOCs (see above). For VOCs not contained in this mixture like limonene, we used calculated sensitivities based on the quantitative liquid amount injected into the known chamber volume.

Ozone was monitored using a Thermo Scientific 49i Ozone Analyzer. The SOA concentration was obtained primarily through scanning mobility particle sizer measurements (SMPS, TSI models: 3080 electrostatic classifier, 3081 differential mobility analyzer, and 3775 condensation particle counter). In one instance, a high-resolution time-of-flight aerosol mass spectrometer (AMS, Aerodyne Research, Inc., described in DeCarlo et al., 2006) was used to obtain 1 second measurements. The size distributions using the SMPS were measured every 135 seconds, and the volume distributions were integrated over a 16-600 nm mobility diameter range. The AMS was run in the "fast mass spec" mode (FMS), where data was obtained at 1 Hz (Kimmel et l., 2001; Nault et al., 2018). The average resolution ($m/\Delta m$) at m/z < 120 was ~2500. Copper and/or stainless-steel tubing was used for the aerosol measurements with a sample flow rate of ~1 LPM (0.635 cm OD, 0.380 cm ID, ~1.2 m for long for AMS, ~2.5 m for SMPS).

5.2.4. Data Processing.

Tofware (v3.2.3) in the Igor Pro 8 (Wavemetrics, OR, USA) environment was used for processing the Vocus data. Peaks were assigned elemental formulas manually, and the time series of these peak integrals were calculated using the peak shape fit. Mass-to-charge ratio calibration

was performed using ions between *m/z* 45 and 297. Backgrounds were measured from the clean chamber immediately before the addition of the precursor. In the hexanal experiments, the decrease in hexanal was very slow and care must be taken to differentiate the chemical loss of hexanal versus a drift in detection sensitivity. For this purpose, acetone was used as a tracer of Vocus sensitivity throughout the dry and humid hexanal experiments. In those experiments, Vocus data were normalized to $2x10^5$ cps of $C_3H_6OH^+$, which is indicated by the units of normalized counts per second (ncps). For the limonene experiments, the Vocus data were not normalized. The condensational sink was calculated from particle size distribution measured by the SMPS. This is shown in Figure 5.2.

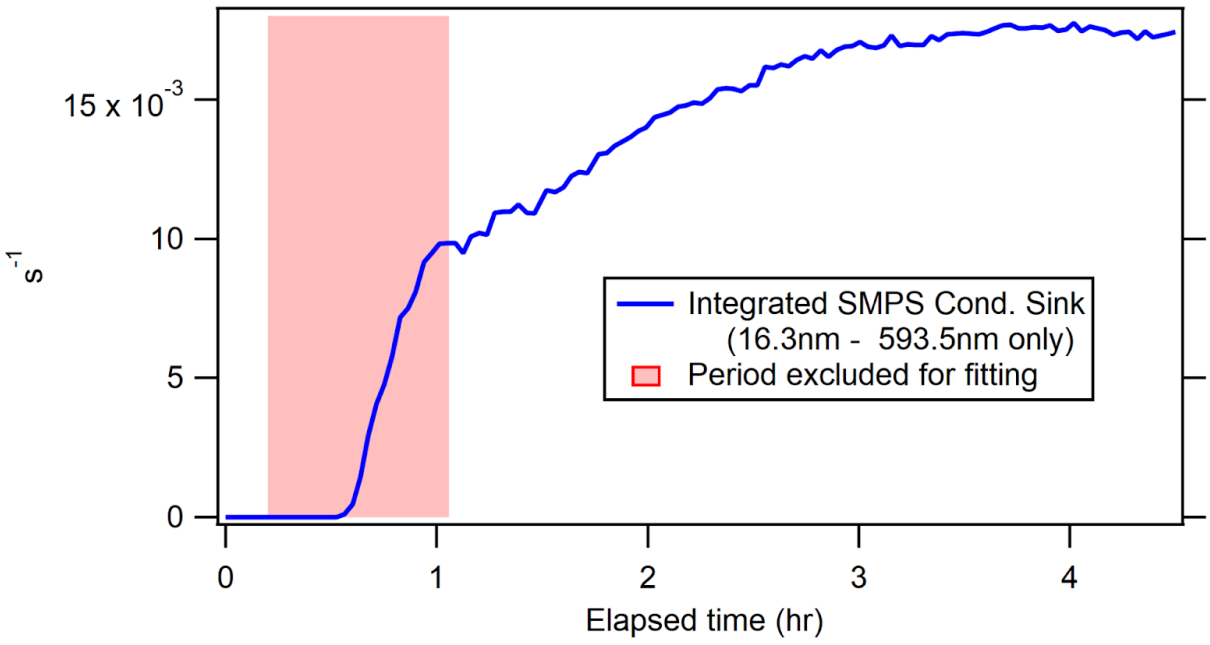

Figure 5.2 Condensation sink calculated from particle size distribution measured by the SMPS. The shaded area denotes the period excluded for fitting the limonene oxidation product molar yields.

AMS data was processed using Squirrel (version 1.65F) and PIKA (version 1.25F) in the Igor Pro 8 (Wavemetrics, OR, USA) environment (Sueper, 2021). The SMPS measures size

particle number distributions and was converted to integrated volume concentrations using custom software in the Igor Pro 8 environment (Day et al., 2024). The volume concentration were converted to mass concentrations by multiplying the SMPS volume concentration by the density derived from AMS elemental ratios (O:C, H:C), as described in Kuwata et al., (2012) and shown in Figure 5.3 (Kuwata et al., 2012). The O:C and H:C ratios were calculated as described in Canagaratna et. al. (2015). The AMS SOA concentration reported in Fig. 5.3 was corrected for differences from the default AMS OA relative ionization efficiency (RIE, 1.4) and collection efficiency (CE, 1) (RIE*CE of 1.4) by calibrating the AMS to the measured SMPS SOA mass concentration (using a single factor determined from a regression). This was necessary since organic RIE and CE can vary by as much as factors of 2-3 for chamber-generated SOA and standards (Xu et al., 2018; Nault et al., 2023; Day et al., 2022).

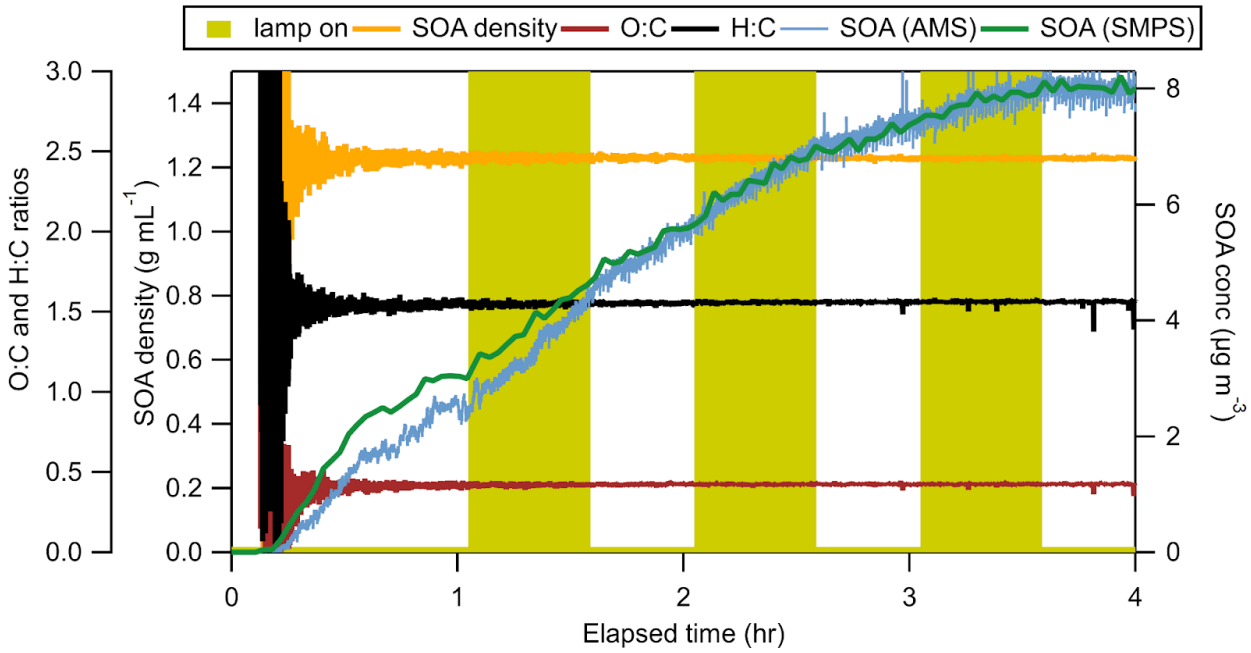

Figure 5.3 O:C and H:C atomic ratios of the SOA measured by the AMS; high levels of noise at the start of the experiment are due to low SOA concentrations. The material density of SOA was estimated from the measured O:C and H:C using the method of Kuwata et al. (2012) The SOA

mass concentration calculated from the volume measured by the SMPS and the AMS density is also shown.

5.2.5. Kinetic Modeling.

A kinetic model for the limonene ozonolysis chamber experiments was built and run in KinSim version 4.24 (a kinetics simulator developed for educational and research purposes) within Igor Pro 8 (Peng et al., 2019). This model was based on the model in Peng et al. (2023a) with the mechanisms for inorganic and organic chemistries being the oxidation flow reactor chemical mechanism and part of the RACM, respectively (Stockwell et al., 1997; Peng et al., 2023a; Peng et al., 2020). The relevant reactions are shown in Table 5.2.

Table 5.2 Reaction mechanism input for the KinSim model. The mechanism has been made freely available at https://gitlab.com/JimenezGroup/KinSim_Cases_Mechs. The mechanism can be run within KinSim, which can be freely downloaded from http://tinyurl.com/kinsim-release.

Process	Rate / rate coefficient	Reference for rate / rate coefficient
limonene + OH → 0.0823 SVOC + 0.0816 LVOC	1.71×10^{-10} cm^3 molecule^{-1} s^{-1}	Stockwell et al., 1997
limonene + O_3 → 0.0823 SVOC + 0.0816 LVOC	2.0×10^{-16} cm^3 molecule^{-1} s^{-1}	Stockwell et al., 1997
SVOC + OH → 0.955 LVOC	1×10^{-10} cm^3 molecule^{-1} s^{-1}	Estimated based on MCM (Jenkin et al., 2015)
SVOC + O_3 → 0.955 LVOC	1×10^{-17} cm^3 molecule^{-1} s^{-1}	Estimated based on MCM (Jenkin et al., 2015)
SVOC (LVOC) → $SVOC_w$ ($LVOC_w$)	3.6 h^{-1}	Krechmer et al., 2020
$SVOC_w$ → SVOC	0.55 h^{-1}	Calculated based on Liu et al., 2019
SVOC (LVOC) → $SVOC_p$ ($LVOC_p$)	Constrained by SMPS measurements	N/A
$SVOC_p$ ($LVOC_p$) → SVOC (LVOC)	Calculated real-time in simulation	N/A
$SVOC_p$ ($LVOC_p$) wall deposition	0.052 h^{-1}	Day et al., 2022

The condensable product formation, the gas-particle partitioning, the wall losses of gas- and particle-phase products in the model were simulated in a dynamical manner based on Krechmer et al. (2020), but with different values for several key parameters (Krechmer et al., 2020). In the model, first-generation oxidation of limonene is assumed to produce two products, a semivolatile species (SVOC) and a low-volatility species (LVOC), with saturation mass concentrations being 10 and 0.0001 μg m^{-3}, respectively, and molecular weights being 250 g mol^{-1}. The second-generation oxidation is assumed only to convert SVOC to LVOC. Both OH and O_3 can be the oxidant of these oxidation reactions, with rate coefficients reported in Table 5.2. The lifetime for condensable gases to deposit onto chamber walls in the model was 1000 s (Krechmer et al., 2020). The evaporation rates of gases partitioned to chamber walls were calculated per Liu et al. (2019). To best fit the experimental results, the particle deposition rate in the chamber was fitted as 0.052 h^{-1}, which is consistent with other experiments conducted in this chamber (Liu et al., 2019; Day et al., 2022).

5.3. Results and Discussion

5.3.1. Gas-Phase Removal of Limonene

Results of limonene chamber experiments under dry conditions are shown in Figure 5.1 and under humid conditions in Figure 5.4. Prior to the addition of limonene to the chamber, O_3 was produced by the 222 nm lamp in 2 steps. The O_3 production rate during these steps was measured at ~24 ppb hr^{-1}, which is consistent with previous measurements (Peng et al., 2023b). At time zero, limonene was added to the chamber. Ozonolysis of limonene leads to removal of limonene and O_3, and to formation of SOA. After 1 hour, the GUV222 lamp was switched on and then alternated on a 30-min on-off cycle. When the GUV222 lamp was on, the O_3 started to increase again and, as

will be shown below, the removal of limonene and the formation of SOA were accelerated at these times. Also included in Figure 5.1 are the model results for the concentrations of limonene, O_3, and SOA.

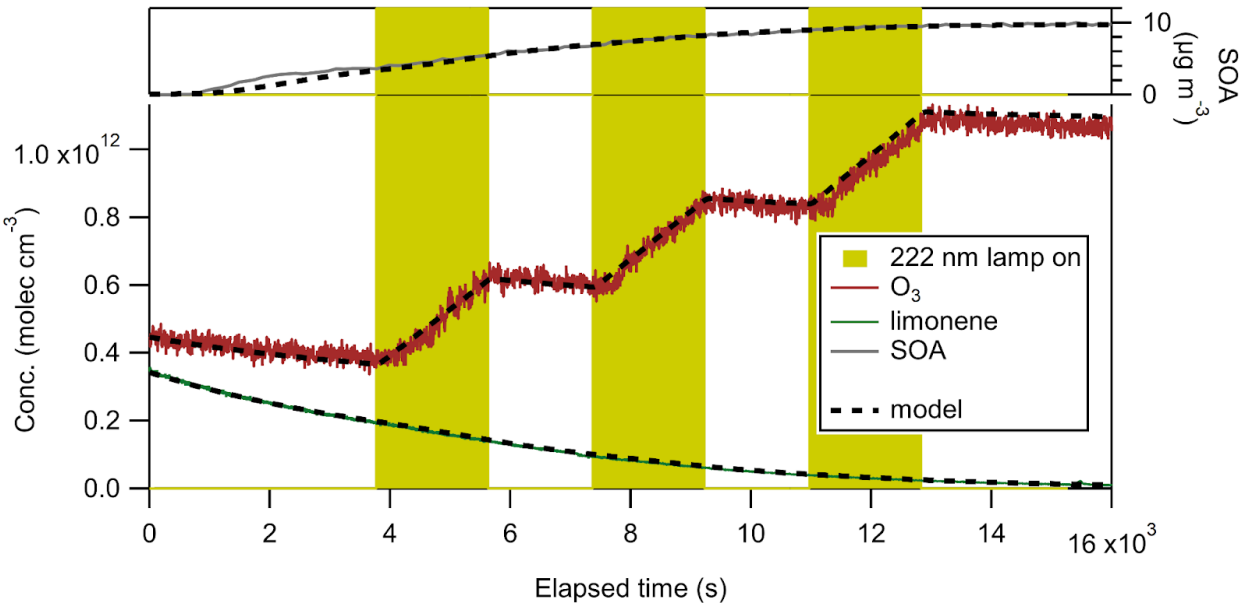

Figure 5.4 Modeled and experimental results for limonene ozonolysis under humid conditions.

In Figure 5.5A, the limonene data from Figure 5.1 are reproduced. While the data appear to show an approximate exponential decay, this should not be strictly true, since O_3 was not constant. The limonene loss rate, -d[LIM]/dt (Figure 5.5B), is described by:

$$\frac{d[LIM]}{dt} = -k_{LIM+O_3}[LIM][O_3] - k_{LIM+OH}[LIM][OH] \qquad (5.1)$$

in which the concentrations of limonene, [LIM], ozone, [O_3], and hydroxyl, [OH], all vary in time. We include hydroxyl (OH) reactions here for 2 reasons: (i) primary OH can be formed from ozone photolysis, and (ii) secondary OH can be formed from limonene ozonolysis. It is seen from Figure 5.5B that the limonene loss rate shows a clear kink when the GUV222 lamp comes on at t=1 hour.

At this time, O_3 starts to increase again due to the GUV222 lamp and the limonene loss rate accelerates. Similar changes in slope in the limonene loss rate can also be seen at t=2 and t=3 h, though less clearly. Also added to Figure 5.5B is the limonene loss rate that can be explained from ozone only (first term on the right-hand side of Equation (5.1)). The ozone reaction does not fully account for the observed loss rate of limonene, and the difference can be explained by OH as will be shown quantitatively below. We conclude that the decrease in limonene is not a simple exponential in time, but that it is modulated by the GUV222 light, which enhances the concentrations of O_3 and OH in the chamber.

To address the loss of limonene by OH, we can rearrange Equation (5.1) as follows:

$$\frac{k_{LIM+OH}[LIM][OH]}{k_{LIM+O_3}[LIM][O_3]} = \frac{\frac{-d[LIM]}{dt}}{k_{LIM+O_3}[LIM][O_3]-1} \quad \textbf{(5.2)}$$

The term on the left represents the relative loss rates of limonene in reaction with OH and O_3, respectively. The term on the right is composed of measured concentrations and the literature value for the rate coefficient (Atkinson, 1986; Shu and Atkinson, 1994). Figure 5.5C shows the numerical value for the parameter $k_{LIM+OH}[OH] / k_{LIM+O3}[O_3]$ calculated from the data using equation (5.2). The ratio is initially around 1, indicating that limonene is removed by O_3 and OH at equal rates. Later, the ratio approaches zero, indicating that the loss to OH is much smaller than the loss to O_3. Also shown in Figure 5.5C is the parameter $k_{LIM+OH}[OH] / k_{LIM+O3}[O_3]$ calculated from the model. The excellent agreement with the data shows that the removal of limonene by O_3 and OH, as well as the formation of OH is well represented in the mechanism. The time series also gives some insight into the source of OH. Primary OH, produced from O_3 photolysis and subsequent reaction of O^1D with water (under humid conditions), can only be produced when the GUV222 lamp is on. In contrast, secondary OH, produced from limonene ozonolysis, does not require the lamp to be

on. As the ratio $k_{LIM+OH}[OH]$ / $k_{LIM+O3}[O_3]$ is not strongly modulated by the GUV222 lamp, we conclude that most of the OH is secondary, which is consistent with the modeled OH and previous measurements (Barber et al., 2023; Atkinson and Aschmann, 1993; Aschmann et al., 2002).

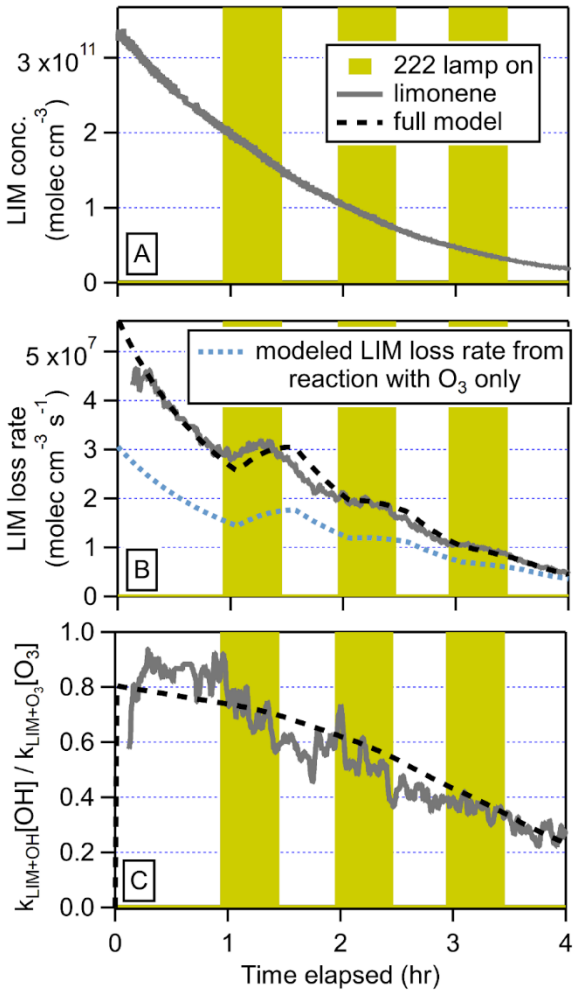

Figure 5.5 Time series of limonene (LIM) reacting with O_3 measured by the Vocus under dry conditions, similar to Fig 1, but now in units of molecules cm^{-3} (A); the modeled and experimental decay rate of limonene and the modeled decay rate of limonene due to only O_3 (B) per equation (1); and modeled and experimental $k_{LIM+OH}[OH]$ / $k_{LIM+O3}[O_3]$ (C) per equation (2).

To further evaluate the production of primary OH radicals, chamber experiments exposing hexanal to 222 nm light were performed under humid conditions (Figure 5.6B). Hexanal reacts

efficiently with OH but not with O_3. Any removal of hexanal would therefore be due to primary OH formation. Also, photolysis of hexanal is expected to be minimal, and this was confirmed in a chamber experiment exposing hexanal to 222 nm light under dry conditions (Figure 5.6A). Figure 5.6 summarizes the results of these experiments. It was found that removal of hexanal is exceedingly slow under these conditions (0.2 molecules cm^{-3} hr^{-1}), indicating that primary OH production is not important for VOC removal in these experiments. Barber et al. (2023) found primary OH production to be more important at fluence rates about 18 times larger than the fluence rates in our experiments.

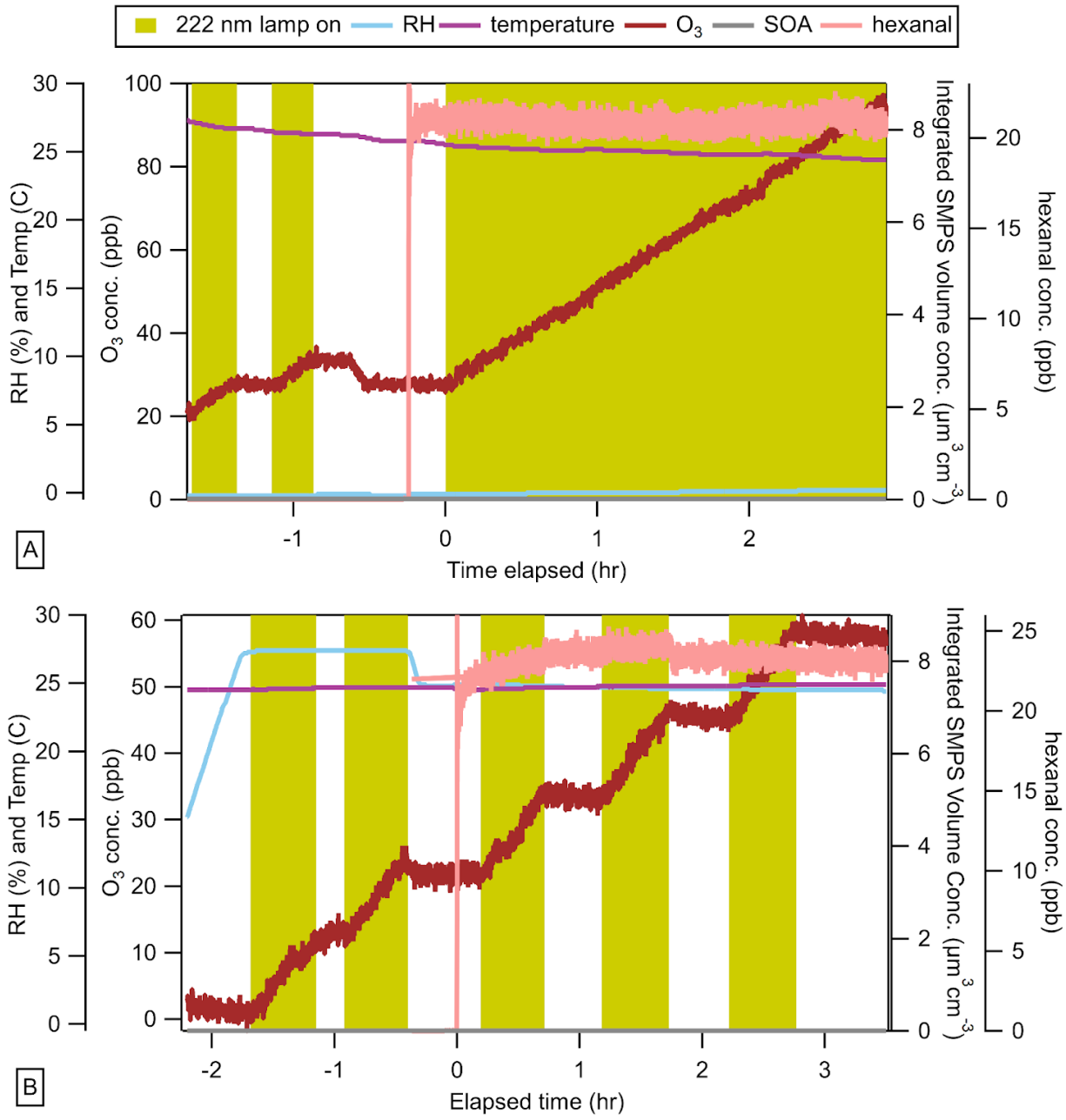

Figure 5.6 Time series of hexanal, ozone, and integrated particle volume concentration under dry conditions (A) and humid conditions (B). No limonene was present during these experiments.

5.3.2. Formation of Secondary Organic Aerosol

Figure 5.1 also shows the formation of SOA measured by the SMPS resulting from the reactions of limonene induced by the GUV222 lamp. Also included in Figure 5.1 is the calculated

SOA formation from the model. Here, we have adjusted the values for the molar yield of gas-phase products of limonene oxidation and used the measured wall deposition rate of particles to obtain a better match with the data. The distribution of SVOC and LVOC for the limonene ozonolysis experiments under dry and humid conditions is shown in Figure 5.7

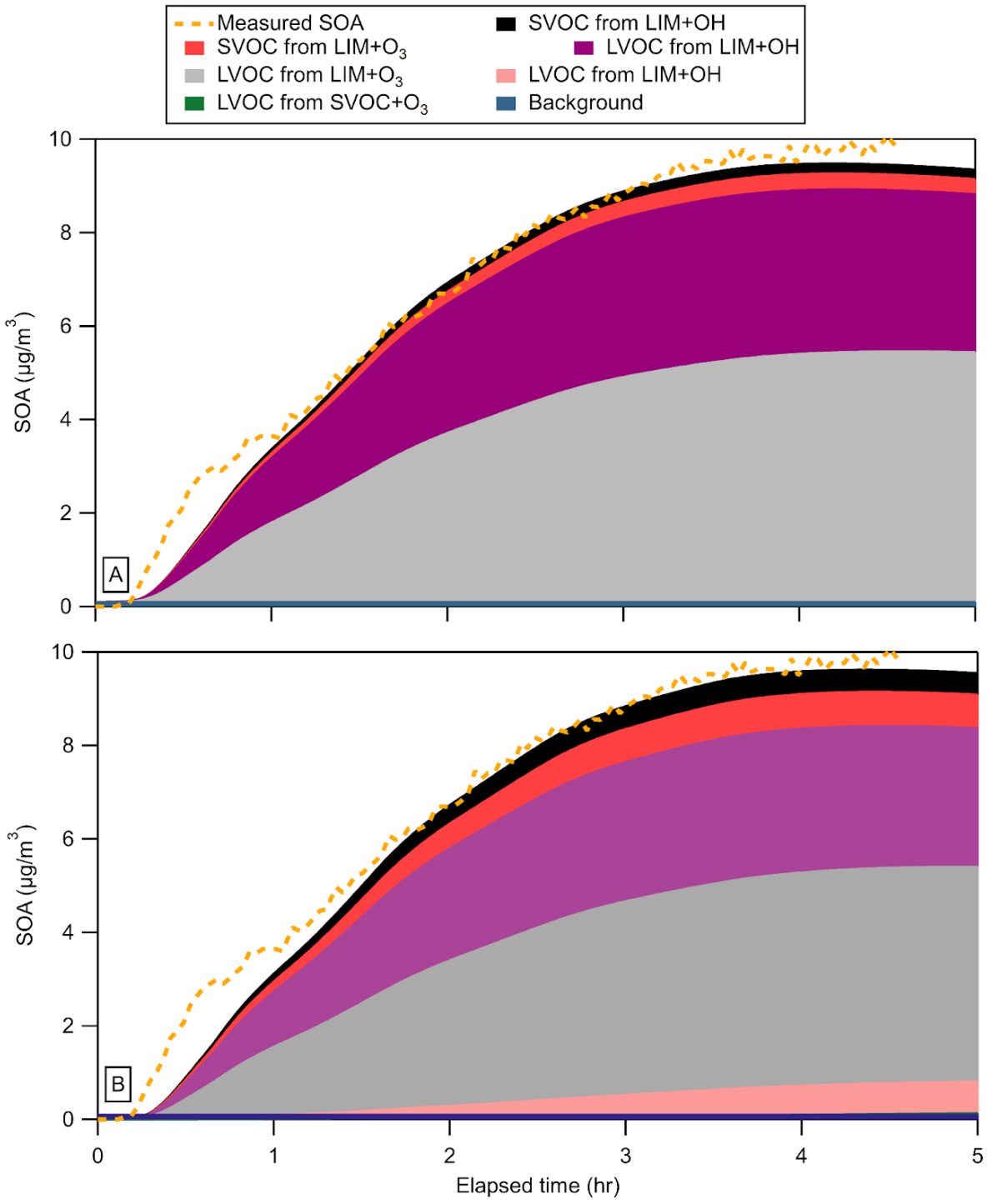

Figure 5.7 Measured SOA (dashed) and the stacked modeled SOA distribution (solid) for limonene irradiation by GUV222 under dry (A) and humid (B) conditions.

The molar yields of the first-generation LVOC and SVOC, and the second-generation LVOC before partitioning were estimated to be 8.23%, 8.16%, and 95.5%, respectively (assuming a molar mass of 250 g mol^{-1}) to best reproduce the observed SOA formation and growth with the model (see Figure 5.1 and Formation of Secondary Organic Aerosol for details). The period near the beginning of the experiment saw condensation sink increasing very rapidly (Figure 5.2). The SMPS could not sufficiently detect the ultrafine particles that were formed in a large number during that period. To avoid possible biases, that period was thus excluded for the fitting that estimated the molar yields of SVOC and LVOC.

SOA formation is analyzed further in Figure 5.8. Figure 5.8B shows the derivative of the SOA concentration versus time, in other words the SOA formation rate. As the concentration of O_3 and OH are both modulated by the GUV222 lamp, the SOA formation rate also shows a modulation by the lamp. When the lamp is on, the SOA formation rate accelerates as O_3 is formed by the lamp. In contrast, when the lamp is off, the SOA formation rate decreases as ozone and limonene are both removed.

Figure 5.8B also shows the modeled SOA formation rate, which shows a similar modulation by the GUV222 lamp. To be clear, the modulation in the model is only caused by the modulation of the O_3 formation by the lamp. The measured and modeled SOA formation rates are in good agreement, but the comparison shows some evidence that the measured SOA formation rates are more strongly modulated by the GUV222 lamp than the modeled SOA formation rates. To investigate this in more detail, Figure 5.8C shows the ratio of the modeled SOA formation rate divided by the measured SOA formation rate. Here it is seen that while the ratio hovers around 1 (modeled and measured SOA formation rates agree), there is a slight dependence of this ratio on the lamp: when the lamp is on, the ratio between modeled and measured SOA formation rates

increases by ~19% when the lamp is on relative to the periods when the lamp is off. This would suggest that the measured SOA formation rate actually decreases slightly with the GUV222 lamp, but the effect is small.

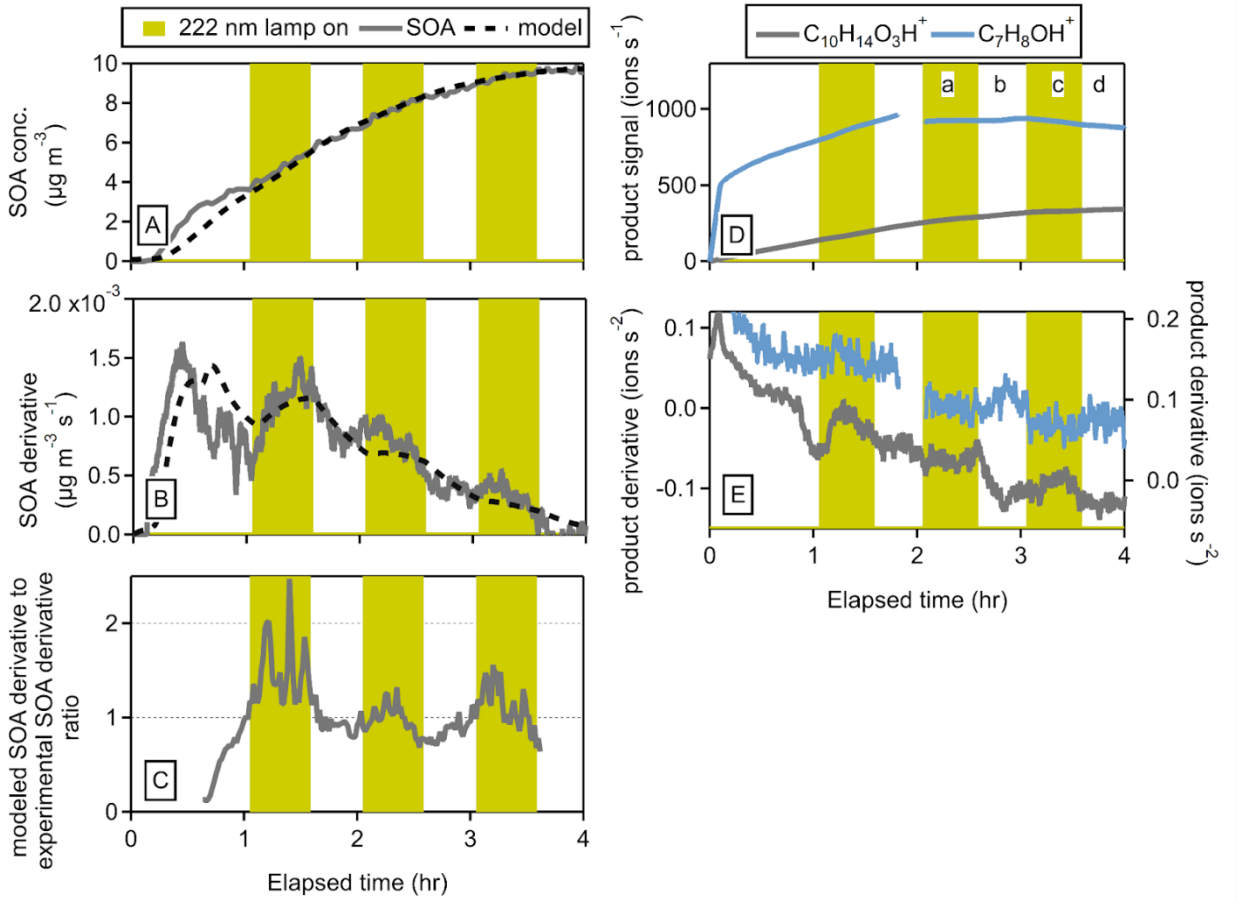

Figure 5.8 Experimental and modeled SOA produced from the oxidation of limonene (A), the experimental and modeled SOA derivative (B), and the ratio of the modeled SOA derivative to the experimental SOA derivative (C) under dry conditions; gas-phase products produced from the oxidation of limonene (D), and the gas-phase products derivatives (E) under dry conditions.

We conclude that the GUV222 lamp causes small but noticeable differences in the SOA formation rate. Nevertheless, the effect is small and representing the SOA formation from limonene induced by GUV222 can be described by using well-known ozonolysis reactions. The congruence between modeled SOA formation and experimental results under both dry and humid

conditions, even during GUV222 lamp activation, suggests that the lamp did not substantially impact SOA formation, and the amount of SOA formed is not impacted by the humidity. Next, we will discuss results from the gas-phase product measurements to study the effects of GUV222 in more detail.

5.3.3. Formation of Gas-Phase Products

Finally, we studied the effects of the GUV222 lamp on the formation of gas-phase products. Previous research has identified both the gas-phase products resulting from the ozonolysis of limonene, as well as the underlying reaction mechanisms (Weschler and Shields, 1999; Grosjean et al., 1992; Grosjean et al., 1993; Ham et al., 2016; Wang and Wang, 2021; Chen et al., 2021). Expected products for the ozonolysis of limonene (limonaldehyde, limonaketone, limononic acid, keto-limonaldehyde, and keto-limononic acid) are shown in Figure 5.9 (Weschler and Shields, 1999; Wang ang Wang, 2021). The product mass spectra observed in this work (Figure 5.9) have some main oxidation products labeled at MH^+. There is significant fragmentation in the Vocus and although there are ways to account for product fragmentation, this was not done here (Jenks et al., 2023).

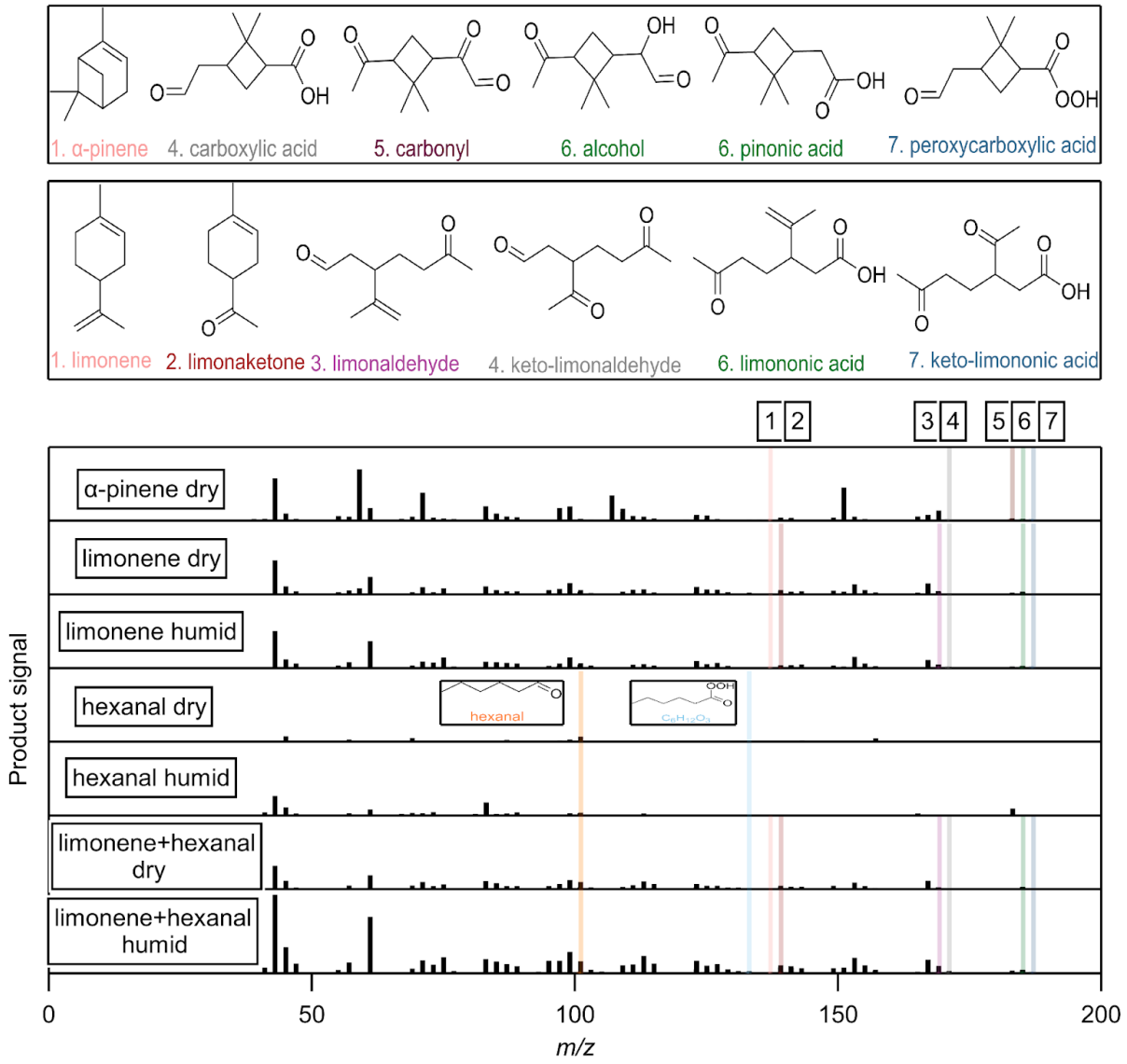

Figure 5.9 Mass spectra of oxidation products from α-pinene under dry conditions, limonene under dry and humid conditions, hexanal under dry and humid conditions, and limonene and hexanal under dry and humid conditions measured by the Vocus. Some limonene oxidation products are highlighted.

To qualitatively evaluate the effect of the 222 nm lamp on the formation of gas-phase products, Figure 5.8D shows the measured time series for 2 of the ions related to the gas-phase products. After an initial increase in their concentrations, the signal reaches a plateau after ~2 hours as the formation rates slow down and/or the formation and loss are in steady state. Again, the

derivative of the time series, in other words the product formation rates, were calculated (Figure 5.8E). There are small changes in the time derivatives for both gas-phase products as the GUV222 light is turned on and off under both humid and dry conditions (for both limonene and α-pinene), but the changes are not large. The derivative for some ions approaches 0, meaning the production and loss of that ion are approaching steady state. The derivative for some ions becomes negative, meaning they are predominantly removed. To summarize this analysis across all *m/z*, we have calculated the change in product ion signal (Figure 5.10A) and formation rates (Figure 5.10B) when the GUV222 lamp is on. Specifically, we calculate the average signal and formation rate during period c (lamp on) and divide it by average signal and formation rates during periods b and d (lamp off). The resulting ratio is presented as a function of *m/z* in Figure 5.10. Clearly, the lamp does cause significant changes in the product formation rates of some gas-phase species (as the values for the above metric range from 1.5×10^{-1} to 2.8×10^{1}), but these do not lead to large changes in the concentration of the gas-phase species in the chamber, as seen in Figure 5.10A. There appears to be a periodicity in the metric indicating that molecules with certain functional groups behave differently; we have not investigated this further. Our goal here was a qualitative analysis to look for large changes in the gas-phase products during the lamp-on periods, which were not observed.

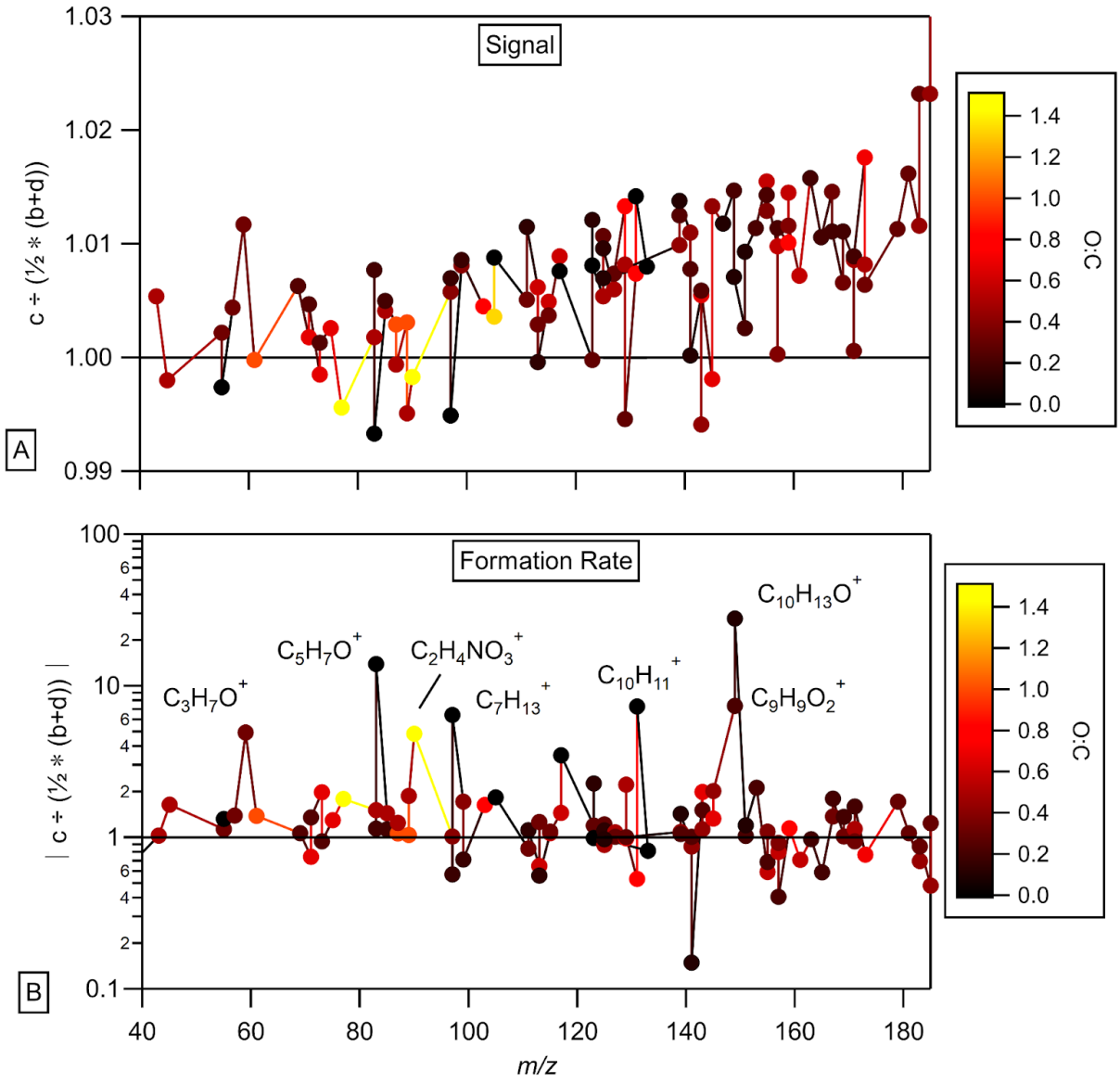

Figure 5.10 The average signal (A) and the average formation rate (B) of gas-phase products during period c (lamp on) divided by the average formation rates during periods b and d (lamp off) as a function of *m/z*.

5.4. Implications

The health impacts of O_3, PM, and toxic organics should be considered when using 222 nm lamps to disinfect indoor air. The overall conclusion from this work is that existing knowledge on

limonene photolysis is sufficient to describe SOA formation associated with the use of GUV222. We found that this chemistry is only slightly perturbed by the presence of 222 nm light.

Thesis Conclusions

The research presented in Chapter 2 findings on the gas-phase products, yields, and mechanism resulting from the reaction between Δ-3-carene and NO_3 radicals. The measured total molar yield of gas-phase products was 50%, comprising multifunctional compounds with various functional groups such as ketone, aldehyde, alcohol, carboxylic acid, peroxide, epoxide, and nitrate. Acetic acid exhibited the largest yield at 14%, followed by acetone at 9%, DC at 8%, CN at 4%, acetaldehyde at 4%, and HN at 2%. The total gas-phase organic nitrate yield was 7%, mainly attributed to CN and HN.

The iodide CIMS proved invaluable for identifying parent ions, while the Vocus facilitated easier quantification of gas-phase products. Tubing delay experiments aided in identifying ion fragments in the Vocus, crucial for more accurate quantification of gas-phase product yields. The implementation of the voltage scanning technique demonstrated the iodide CIMS's heightened sensitivity to the degree of product functionalization compared to the Vocus. Explorations are underway to determine if these differences can be explained by structure-activity relationships, potentially enhancing product quantification with the iodide CIMS.

Additionally, this study sheds light on the oxidation of Δ-3-carene by NO_3 radicals, offering insights into the fate of monoterpenes in the atmosphere and their resultant reaction products, including organic nitrates. These findings are expected to aid in the interpretation of field data and the refinement of chemical models.

The research in Chapter 3 evaluated the gas-phase products, yields, and mechanism involved in the reaction of five monoterpenes - Δ-3-carene, α-pinene, β-pinene, ocimene, and limonene - with NO_3 radicals. Using the Vocus and iodide CIMS, multifunctional compounds containing ketone, aldehyde, alcohol, carboxylic acid, peroxide, epoxide, and nitrate functional

groups were identified. The iodide CIMS played a crucial role in identifying parent ions, while the Vocus aided in quantifying gas-phase products. Tubing delay experiments enhanced precision by identifying ion fragments, while the integration of the voltage scanning technique confirmed the stronger binding of more functionalized monoterpene oxidation products to the iodide adduct. This information could facilitate the development of a structure-activity relationship to predict iodide CIMS sensitivity in the future.

Furthermore, several ions derived from monoterpene oxidation products observed in the laboratory were also detected in ambient measurements. A comparison revealed that the ambient measurements closely resembled laboratory measurements of α-pinene, suggesting its predominance during the ambient measurements. The oxidation of monoterpenes by NO_3 radicals enhances our understanding of their atmospheric fate, particularly regarding the formation of organic nitrates. These insights are expected to provide valuable contributions to the interpretation of field data and the refinement of chemical models.

Chapter 4 evaluated the mechanisms and gas-phase oxidation products from the OH radical oxidation of five monoterpenes. Analysis of time series data and mass spectra provided insight into the composition of these oxidation products. Notably, the mass spectra highlight similarities among the monoterpenes in the formation of specific oxidation products, including carbonyl compounds and hydroxy nitrates. Additionally, voltage scanning techniques are employed to evaluate the sensitivity of the iodide CIMS instrument, revealing variability in sensitivity based on the number of functional groups present in the compounds. These findings deepen our understanding of monoterpene oxidation mechanisms and shed light on the challenges associated with quantifying product yields.

In chapter 5 the influence of GUV222 on limonene-derived secondary organic aerosol (SOA) formation was evaluated. Chamber experiments revealed the generation of ozone (O_3) by the 222 nm lamp. Upon exposure to this oxidant, volatile organic compounds (VOCs) like limonene produced both gas- and particle-phase oxidation products. Our findings indicate that limonene degradation occurs due to the combined effects of O_3 (produced by GUV222) and secondary hydroxyl radicals (from limonene ozonolysis). A kinetic model based on the RACM mechanism effectively reproduced these observations. The congruence between modeled SOA formation and experimental results suggests minimal impact on SOA formation during GUV222 lamp activation. Gas-phase product analyses underscored the consistency of existing knowledge on limonene ozonolysis, with minor alterations observed under GUV222 conditions.

Considering the health implications of O_3, particulate matter (PM), and toxic organic compounds, caution is warranted when employing 222 nm lamps for indoor air disinfection. Our study concludes that existing understanding of limonene photolysis adequately explains SOA formation associated with GUV222 usage, with minimal disturbance by the presence of 222 nm light. Future investigations will assess the real-world implications of GUV222 on indoor air quality.

References

Aschmann, Sara M., Janet Arey, and Roger Atkinson. “OH Radical Formation from the Gas-Phase Reactions of O3 with a Series of Terpenes.” *Atmospheric Environment* 36, no. 27 (September 2002): 4347–55. https://doi.org/10.1016/S1352-2310(02)00355-2.

Atkinson, Roger. “Kinetics and Mechanisms of the Gas-Phase Reactions of the Hydroxyl Radical with Organic Compounds under Atmospheric Conditions.” *Chemical Reviews* 86, no. 1 (February 1, 1986): 69–201. https://doi.org/10.1021/cr00071a004.

Atkinson, Roger, and Sara M. Aschmann. “Hydroxyl Radical Production from the Gas-Phase Reactions of Ozone with a Series of Alkenes under Atmospheric Conditions.” *Environmental Science & Technology* 27, no. 7 (July 1, 1993): 1357–63. https://doi.org/10.1021/es00044a010.

Atkinson, Roger, and Janet Arey. “Gas-Phase Tropospheric Chemistry of Biogenic Volatile Organic Compounds: A Review.” *Atmospheric Environment* 37, no. SUPPL. 2 (2003): 197–219. https://doi.org/10.1016/S1352-2310(03)00391-1.

Baptista, Leonardo, Lilian Fernandes Francisco, Jacques Fernandes Dias, Edilson Clemente Da Silva, Claudio Vinicius Ferreira Dos Santos, Felipe Simões Gil De Mendonça, and Graciela Arbilla. “Theoretical Study of Δ-3-(+)-Carene Oxidation.” *Phys. Chem. Chem. Phys.* 16, no. 36 (2014): 19376–85. https://doi.org/10.1039/C4CP02627F.

Barber, Victoria P., Matthew B. Goss, Lesly J. Franco Deloya, Lexy N. LeMar, Yaowei Li, Erik Helstrom, Manjula Canagaratna, Frank N. Keutsch, and Jesse H. Kroll. “Indoor Air Quality Implications of Germicidal 222 Nm Light.” *Environmental Science & Technology* 57, no. 42 (October 24, 2023): 15990–98. https://doi.org/10.1021/acs.est.3c05680.

Bates, Kelvin H., Guy J. P. Burke, James D. Cope, and Tran B. Nguyen. “Secondary Organic Aerosol and Organic Nitrogen Yields from the Nitrate Radical (NO₃) Oxidation of Alpha-Pinene from Various RO₂ Fates.” *Atmospheric Chemistry and Physics* 22, no. 2 (January 31, 2022): 1467–82. https://doi.org/10.5194/acp-22-1467-2022.

Bernstein, Jonathan A., Neil Alexis, Hyacinth Bacchus, I. Leonard Bernstein, Pat Fritz, Elliot Horner, Ning Li, et al. “The Health Effects of Nonindustrial Indoor Air Pollution.” *Journal of Allergy and Clinical Immunology* 121, no. 3 (March 2008): 585–91. https://doi.org/10.1016/j.jaci.2007.10.045.

Bi, Chenyang, Jordan E. Krechmer, Graham O. Frazier, Wen Xu, Andrew T. Lambe, Megan S. Claflin, Brian M. Lerner, et al. “Quantification of Isomer-Resolved Iodide Chemical Ionization Mass Spectrometry Sensitivity and Uncertainty Using a Voltage-Scanning Approach.” *Atmospheric Measurement Techniques* 14, no. 10 (October 25, 2021): 6835–50. https://doi.org/10.5194/amt-14-6835-2021.

Biesenthal, T.A., Q. Wu, P.B. Shepson, H.A. Wiebe, K.G. Anlauf, and G.I. Mackay. “A Study of Relationships between Isoprene, Its Oxidation Products, and Ozone, in the Lower Fraser Valley, BC.” *Atmospheric Environment* 31, no. 14 (July 1997): 2049–58. https://doi.org/10.1016/S1352-2310(96)00318-4.

Bilde, Merete, Kelley Barsanti, Murray Booth, Christopher D. Cappa, Neil M. Donahue, Eva U. Emanuelsson, Gordon McFiggans, et al. “Saturation Vapor Pressures and Transition Enthalpies of Low-Volatility Organic Molecules of Atmospheric Relevance: From Dicarboxylic Acids to Complex Mixtures.” *Chemical Reviews* 115, no. 10 (May 27, 2015): 4115–56. https://doi.org/10.1021/cr5005502.

Boyd, C. M., J. Sanchez, L. Xu, A. J. Eugene, T. Nah, W. Y. Tuet, M. I. Guzman, and N. L. Ng. “Secondary Organic Aerosol Formation from the β-pinene+NO3 System: Effect of Humidity and Peroxy Radical Fate.” *Atmospheric Chemistry and Physics* 15, no. 13 (2015): 7497–7522. https://doi.org/10.5194/acp-15-7497-2015.

Browne, E. C., and R. C. Cohen. “Effects of Biogenic Nitrate Chemistry on the NO_X Lifetime in Remote Continental Regions.” *Atmospheric Chemistry and Physics* 12, no. 24 (December 17, 2012): 11917–32. https://doi.org/10.5194/acp-12-11917-2012.

Buonanno, Manuela, Brian Ponnaiya, David Welch, Milda Stanislauskas, Gerhard Randers-Pehrson, Lubomir Smilenov, Franklin D. Lowy, David M. Owens, and David J. Brenner. “Germicidal Efficacy and Mammalian Skin Safety of 222-Nm UV Light.” *Radiation Research* 187, no. 4 (April 2017): 493–501. https://doi.org/10.1667/RR0010CC.1.

Camargo, Carolina, Andréanne Lupien, Fiona McIntosh, Dick Menzies, Marcel A. Behr, and Selena M. Sagan. “Effectiveness of Germicidal Ultraviolet Light to Inactivate Coronaviruses on Personal Protective Equipment to Reduce Nosocomial Transmission.” *Infection Control & Hospital Epidemiology* 43, no. 7 (July 2022): 886–91. https://doi.org/10.1017/ice.2021.249.

Canagaratna, M. R., J. L. Jimenez, J. H. Kroll, Q. Chen, S. H. Kessler, P. Massoli, L. Hildebrandt Ruiz, et al. “Elemental Ratio Measurements of Organic Compounds Using Aerosol Mass Spectrometry: Characterization, Improved Calibration, and Implications.” *Atmospheric Chemistry and Physics* 15, no. 1 (January 12, 2015): 253–72. https://doi.org/10.5194/acp-15-253-2015.

Capouet, M, J Peeters, and B Noziere. “Alpha-Pinene Oxidation by OH: Simulations of Laboratory Experiments.” *Atmos. Chem. Phys.*, 2004.

Cappellin, Luca, Thomas Karl, Michael Probst, Oksana Ismailova, Paul M. Winkler, Christos Soukoulis, Eugenio Aprea, Tilmann D. Märk, Flavia Gasperi, and Franco Biasioli. “On Quantitative Determination of Volatile Organic Compound Concentrations Using Proton Transfer Reaction Time-of-Flight Mass Spectrometry.” *Environmental Science & Technology* 46, no. 4 (February 21, 2012): 2283–90. https://doi.org/10.1021/es203985t.

Carlton, Annmarie G., Robert W. Pinder, Prakash V. Bhave, and George A. Pouliot. “To What Extent Can Biogenic SOA Be Controlled?” *Environmental Science & Technology* 44, no. 9 (May 1, 2010): 3376–80. https://doi.org/10.1021/es903506b.

Chen, Wei, Yuqing Ye, Weiwei Hu, Huaishan Zhou, Tianle Pan, Yingkun Wang, Wei Song, et al. “Real-Time Characterization of Aerosol Compositions, Sources, and Aging Processes in Guangzhou During PRIDE-GBA 2018 Campaign.” *Journal of Geophysical Research: Atmospheres* 126, no. 16 (August 27, 2021). https://doi.org/10.1029/2021JD035114.

Claflin, Megan S., and Paul J. Ziemann. “Identification and Quantitation of Aerosol Products of the Reaction of β-Pinene with NO_3 Radicals and Implications for Gas- and Particle-Phase Reaction Mechanisms.” *The Journal of Physical Chemistry A* 122, no. 14 (April 12, 2018): 3640–52. https://doi.org/10.1021/acs.jpca.8b00692.

Dam, Michelia, Danielle C Draper, Andrey Marsavin, Juliane L Fry, and James N Smith. “Observations of Gas-Phase Products from the Nitrate Radical-Initiated Oxidation of Four Monoterpenes.” *Atmospheric Chemistry and Physics Discussions*, no. 3 (2022): 1–22.

D’Ambro, Emma L., Noora Hyttinen, Kristian H. Møller, Siddharth Iyer, Rasmus V. Otkjær, David M. Bell, Jiumeng Liu, et al. “Pathways to Highly Oxidized Products in the Δ3-Carene + OH System.” *Environmental Science & Technology* 56, no. 4 (February 15, 2022): 2213–24. https://doi.org/10.1021/acs.est.1c06949.

Davis, M, and P Stevens. “Measurements of the Kinetics of the OH-Initiated Oxidation of -Pinene: Radical Propagation in the OH+-pinene+O+NO Reaction System.” *Atmospheric Environment* 39, no. 10 (March 2005): 1765–74. https://doi.org/10.1016/j.atmosenv.2004.09.068.

Day, Douglas A., Juliane L. Fry, Hyun Gu Kang, Jordan E. Krechmer, Benjamin R. Ayres, Natalie I. Keehan, Samantha L. Thompson, et al. “Secondary Organic Aerosol Mass Yields from NO_3 Oxidation of α-Pinene and Δ-Carene: Effect of RO_2 Radical Fate.” *The Journal of Physical Chemistry A* 126, no. 40 (October 13, 2022): 7309–30. https://doi.org/10.1021/acs.jpca.2c04419.

Day, D. A., Michael J. Cubison, B. B. Palm, and J. L. Jimenez. “Scanning Mobility Particle Sizer Loader and Plotter.” University of Colorado Boulder, 2024. https://gitlab.com/JimenezGroup/smps_loader_plotter.

Deal, Alexandra M., and Veronica Vaida. “Oxygen Effect on the Ultraviolet-C Photochemistry of Lactic Acid.” *The Journal of Physical Chemistry A* 127, no. 13 (April 6, 2023): 2936–45. https://doi.org/10.1021/acs.jpca.3c00992.

DeCarlo, Peter F., Joel R. Kimmel, Achim Trimborn, Megan J. Northway, John T. Jayne, Allison C. Aiken, Marc Gonin, et al. “Field-Deployable, High-Resolution, Time-of-Flight Aerosol Mass Spectrometer.” *Analytical Chemistry* 78, no. 24 (December 1, 2006): 8281–89. https://doi.org/10.1021/ac061249n.

Deming, Benjamin L., Demetrios Pagonis, Xiaoxi Liu, Douglas A. Day, Ranajit Talukdar, Jordan E. Krechmer, Joost A. De Gouw, Jose L. Jimenez, and Paul J. Ziemann. "Measurements of Delays of Gas-Phase Compounds in a Wide Variety of Tubing Materials Due to Gas–Wall Interactions." *Atmospheric Measurement Techniques* 12, no. 6 (June 28, 2019): 3453–61. https://doi.org/10.5194/amt-12-3453-2019.

DeVault, Marla P., and Paul J. Ziemann. "Gas- and Particle-Phase Products and Their Mechanisms of Formation from the Reaction of Δ-3-Carene with NO_3 Radicals." *The Journal of Physical Chemistry A* 125, no. 47 (December 2, 2021): 10207–22. https://doi.org/10.1021/acs.jpca.1c07763.

DeVault, Marla P., Anna C. Ziola, and Paul J. Ziemann. "Products and Mechanisms of Secondary Organic Aerosol Formation from the NO_3 Radical-Initiated Oxidation of Cyclic and Acyclic Monoterpenes." *ACS Earth and Space Chemistry* 6, no. 8 (August 18, 2022): 2076–92. https://doi.org/10.1021/acsearthspacechem.2c00130.

Draper, Danielle C., Nanna Myllys, Noora Hyttinen, Kristian H. Møller, Henrik G. Kjaergaard, Juliane L. Fry, James N. Smith, and Theo Kurtén. "Formation of Highly Oxidized Molecules from NO_3 Radical Initiated Oxidation of Δ-3-Carene: A Mechanistic Study." *ACS Earth and Space Chemistry* 3, no. 8 (August 15, 2019): 1460–70. https://doi.org/10.1021/acsearthspacechem.9b00143.

Du, Benni, and Weichao Zhang. "Atmospheric Degradation Mechanisms and Kinetics for OH-Initiated Oxidation of *Trans* -β-Ocimene." *Molecular Physics* 121, no. 2 (January 17, 2023): e2152747. https://doi.org/10.1080/00268976.2022.2152747.

Duncianu, Marius, Marc David, Sakthivel Kartigueyane, Manuela Cirtog, Jean-François Doussin, and Benedicte Picquet-Varrault. "Measurement of Alkyl and Multifunctional Organic Nitrates by Proton-Transfer-Reaction Mass Spectrometry." *Atmospheric Measurement Techniques* 10, no. 4 (April 18, 2017): 1445–63. https://doi.org/10.5194/amt-10-1445-2017.

Fisher, J. A., D. J. Jacob, K. R. Travis, P. S. Kim, E. A. Marais, C. Chan Miller, K. Yu, et al. "Organic Nitrate Chemistry and Its Implications for Nitrogen Budgets in an Isoprene- and Monoterpene-Rich Atmosphere: Constraints from Aircraft (SEAC⁴RS) and Ground-Based (SOAS) Observations in the Southeast US." Preprint. Gases/Atmospheric Modelling/Troposphere/Chemistry (chemical composition and reactions), February 4, 2016. https://doi.org/10.5194/acp-2016-52.

Fry, Juliane L., Danielle C. Draper, Kelley C. Barsanti, James N. Smith, John Ortega, Paul M. Winkler, Michael J. Lawler, et al. "Secondary Organic Aerosol Formation and Organic Nitrate Yield from NO_3 Oxidation of Biogenic Hydrocarbons." *Environmental Science & Technology* 48, no. 20 (October 21, 2014): 11944–53. https://doi.org/10.1021/es502204x.

Fry, J. L., A. Kiendler-Scharr, A. W. Rollins, T. Brauers, S. S. Brown, H. P. Dorn, W. P. Dubé, et al. "SOA from Limonene: Role of NO3 in Its Generation and Degradation."

Atmospheric Chemistry and Physics 11, no. 8 (2011): 3879–94. https://doi.org/10.5194/acp-11-3879-2011.

Geron, Chris, Rei Rasmussen, Robert R. Arnts, and Alex Guenther. "A Review and Synthesis of Monoterpene Speciation from Forests in the United States." *Atmospheric Environment* 34, no. 11 (January 2000): 1761–81. https://doi.org/10.1016/S1352-2310(99)00364-7.

Gkatzelis, Georgios I., Matthew M. Coggon, Brian C. McDonald, Jeff Peischl, Kenneth C. Aikin, Jessica B. Gilman, Michael Trainer, and Carsten Warneke. "Identifying Volatile Chemical Product Tracer Compounds in U.S. Cities." *Environmental Science & Technology* 55, no. 1 (January 5, 2021): 188–99. https://doi.org/10.1021/acs.est.0c05467.

Graeffe, Frans, Yuanyuan Luo, Yishuo Guo, and Mikael Ehn. "Unwanted Indoor Air Quality Effects from Using Ultraviolet C Lamps for Disinfection." *Environmental Science & Technology Letters* 10, no. 2 (February 14, 2023): 172–78. https://doi.org/10.1021/acs.estlett.2c00807.

Greenhalgh, Trisha, Jose L Jimenez, Kimberly A Prather, Zeynep Tufekci, David Fisman, and Robert Schooley. "Ten Scientific Reasons in Support of Airborne Transmission of SARS-CoV-2." *The Lancet* 397, no. 10285 (May 2021): 1603–5. https://doi.org/10.1016/S0140-6736(21)00869-2.

Grosjean, Daniel, Edwin L. Williams, and John H. Seinfeld. "Atmospheric Oxidation of Selected Terpenes and Related Carbonyls: Gas-Phase Carbonyl Products." *Environmental Science & Technology* 26, no. 8 (August 1992): 1526–33. https://doi.org/10.1021/es00032a005.

Grosjean, Daniel, Edwin L. Williams, Eric Grosjean, Jean M. Andino, and John H. Seinfeld. "Atmospheric Oxidation of Biogenic Hydrocarbons: Reaction of Ozone with .Beta.-Pinene, D-Limonene and Trans-Caryophyllene." *Environmental Science & Technology* 27, no. 13 (December 1, 1993): 2754–58. https://doi.org/10.1021/es00049a014.

Guenther, A. B., X. Jiang, C. L. Heald, T. Sakulyanontvittaya, T. Duhl, L. K. Emmons, and X. Wang. "The Model of Emissions of Gases and Aerosols from Nature Version 2.1 (MEGAN2.1): An Extended and Updated Framework for Modeling Biogenic Emissions." *Geoscientific Model Development* 5, no. 6 (November 26, 2012): 1471–92. https://doi.org/10.5194/gmd-5-1471-2012.

Hallquist, Mattias, Ingvar Wängberg, Evert Ljungström, Ian Barnes, and Karl-Heinz Becker. "Aerosol and Product Yields from NO $_3$ Radical-Initiated Oxidation of Selected Monoterpenes." *Environmental Science & Technology* 33, no. 4 (February 1, 1999): 553–59. https://doi.org/10.1021/es980292s.

Hallquist, M, J C Wenger, U Baltensperger, Y Rudich, D Simpson, M Claeys, J Dommen, et al. "The Formation, Properties and Impact of Secondary Organic Aerosol: Current and Emerging Issues." *Atmos. Chem. Phys.*, 2009.

Ham, Jason E., Joel C. Harrison, Stephen R. Jackson, and J.R. Wells. “Limonene Ozonolysis in the Presence of Nitric Oxide: Gas-Phase Reaction Products and Yields.” *Atmospheric Environment* 132 (May 2016): 300–308. https://doi.org/10.1016/j.atmosenv.2016.03.003.

Hantschke, Luisa, Anna Novelli, Birger Bohn, Changmin Cho, David Reimer, Franz Rohrer, Ralf Tillmann, et al. “Atmospheric Photooxidation and Ozonolysis of Δ3-Carene and 3-Caronaldehyde: Rate Constants and Product Yields.” *Atmospheric Chemistry and Physics* 21, no. 16 (August 26, 2021): 12665–85. https://doi.org/10.5194/acp-21-12665-2021.

Hart, Deryl. “Bactericidal Ultraviolet Radiation in the Operating Room: Twenty-Nine-Year Study for Control of Infections.” *Journal of the American Medical Association* 172 (1960): 1019–28.

Hatakeyama, Shiro, Katsuyuki Izumi, Tsutomu Fukuyama, Hajime Akimoto, and Nobuaki Washida. “Reactions of OH with α-Pinene and β-Pinene in Air: Estimate of Global CO Production from the Atmospheric Oxidation of Terpenes.” *Journal of Geophysical Research* 96, no. D1 (1991): 947. https://doi.org/10.1029/90JD02341.

Iyer, Siddharth, Felipe Lopez-Hilfiker, Ben H. Lee, Joel A. Thornton, and Theo Kurtén. “Modeling the Detection of Organic and Inorganic Compounds Using Iodide-Based Chemical Ionization.” *The Journal of Physical Chemistry A* 120, no. 4 (February 4, 2016): 576–87. https://doi.org/10.1021/acs.jpca.5b09837.

Jenks, Olivia J., Marla P. DeVault, Anna C. Ziola, Melissa A. Morris, Melinda K. Schueneman, Harald Stark, Jose L. Jimenez, Paul J. Ziemann, and Joost A. De Gouw. “Investigation of Gas-Phase Products from the NO_3 Radical Oxidation of Δ-3-Carene.” *ACS Earth and Space Chemistry* 7, no. 5 (May 18, 2023): 1097–1106. https://doi.org/10.1021/acsearthspacechem.3c00020.

Jensen, Andrew R. “Measurements of Volatile Organic Compounds in Urban Air by Proton-Transfer-Reaction Mass Spectrometry.” University of Colorado Boulder, 2023. https://www.proquest.com/docview/2813833671?accountid=14503&parentSessionId=pouU5UM5r%252BWDSRoTvf5HgQQtCWNc83lDpa8wcwomADo%253D.

Jimenez, Jose L., Linsey C. Marr, Katherine Randall, Edward Thomas Ewing, Zeynep Tufekci, Trish Greenhalgh, Raymond Tellier, et al. “What Were the Historical Reasons for the Resistance to Recognizing Airborne Transmission during the COVID -19 Pandemic?” *Indoor Air* 32, no. 8 (August 2022). https://doi.org/10.1111/ina.13070.

Kaidzu, Sachiko. “Re-Evaluation of Rat Corneal Damage by Short-Wavelength UV Revealed Extremely Less Hazardous Property of Far-UV-C.” *Photochemistry and Photobiology* 97 (2021): 505–16. https://doi.org/DOI: 10.1111/php.13419.

Kaminski, Martin, Hendrik Fuchs, Ismail-Hakki Acir, Birger Bohn, Theo Brauers, Hans-Peter Dorn, Rolf Häseler, et al. “Investigation of the B-Pinene Photooxidation by OH in the Atmosphere Simulation Chamber SAPHIR.” *Atmospheric Chemistry and Physics* 17, no. 11 (June 6, 2017): 6631–50. https://doi.org/10.5194/acp-17-6631-2017.

Kimmel, Joel R., Delphine K. Farmer, Michael J. Cubison, Donna Sueper, Christian Tanner, Eiko Nemitz, Douglas R. Worsnop, Marc Gonin, and Jose L. Jimenez. "Real-Time Aerosol Mass Spectrometry with Millisecond Resolution." *International Journal of Mass Spectrometry* 303, no. 1 (May 2011): 15–26. https://doi.org/10.1016/j.ijms.2010.12.004.

Klepeis, Neil E, William C Nelson, Wayne R Ott, John P Robinson, Andy M Tsang, Paul Switzer, Joseph V Behar, Stephen C Hern, and William H Engelmann. "The National Human Activity Pattern Survey (NHAPS): A Resource for Assessing Exposure to Environmental Pollutants." *Journal of Exposure Science & Environmental Epidemiology* 11, no. 3 (July 1, 2001): 231–52. https://doi.org/10.1038/sj.jea.7500165.

Krechmer, Jordan E., Demetrios Pagonis, Paul J. Ziemann, and Jose L. Jimenez. "Quantification of Gas-Wall Partitioning in Teflon Environmental Chambers Using Rapid Bursts of Low-Volatility Oxidized Species Generated in Situ." *Environmental Science & Technology* 50, no. 11 (June 7, 2016): 5757–65. https://doi.org/10.1021/acs.est.6b00606.

Krechmer, Jordan E., Douglas A. Day, Paul J. Ziemann, and Jose L. Jimenez. "Direct Measurements of Gas/Particle Partitioning and Mass Accommodation Coefficients in Environmental Chambers." *Environmental Science & Technology* 51, no. 20 (October 17, 2017): 11867–75. https://doi.org/10.1021/acs.est.7b02144.

Krechmer, Jordan, Felipe Lopez-Hilfiker, Abigail Koss, Manuel Hutterli, Carsten Stoermer, Benjamin Deming, Joel Kimmel, et al. "Evaluation of a New Reagent-Ion Source and Focusing Ion–Molecule Reactor for Use in Proton-Transfer-Reaction Mass Spectrometry." *Analytical Chemistry* 90, no. 20 (October 16, 2018): 12011–18. https://doi.org/10.1021/acs.analchem.8b02641.

Krechmer, Jordan E., Douglas A. Day, and Jose L. Jimenez. "Always Lost but Never Forgotten: Gas-Phase Wall Losses Are Important in All Teflon Environmental Chambers." *Environmental Science & Technology* 54, no. 20 (October 20, 2020): 12890–97. https://doi.org/10.1021/acs.est.0c03381.

Kurtén, Theo, Kristian H. Møller, Tran B. Nguyen, Rebecca H. Schwantes, Pawel K. Misztal, Luping Su, Paul O. Wennberg, Juliane L. Fry, and Henrik G. Kjaergaard. "Alkoxy Radical Bond Scissions Explain the Anomalously Low Secondary Organic Aerosol and Organonitrate Yields From α-Pinene + NO_3." *The Journal of Physical Chemistry Letters* 8, no. 13 (July 6, 2017): 2826–34. https://doi.org/10.1021/acs.jpclett.7b01038.

Kuwata, Mikinori, Soeren R. Zorn, and Scot T. Martin. "Using Elemental Ratios to Predict the Density of Organic Material Composed of Carbon, Hydrogen, and Oxygen." *Environmental Science & Technology* 46, no. 2 (January 17, 2012): 787–94. https://doi.org/10.1021/es202525q.

Lee, Anita, Allen H. Goldstein, Jesse H. Kroll, Nga L. Ng, Varuntida Varutbangkul, Richard C. Flagan, and John H. Seinfeld. "Gas-Phase Products and Secondary Aerosol Yields from the Photooxidation of 16 Different Terpenes." *Journal of Geophysical Research* 111, no. D17 (2006): D17305. https://doi.org/10.1029/2006JD007050.

Lee, Ben H., Siddharth Iyer, Theo Kurtén, Jonathan G. Varelas, Jingyi Luo, Regan J. Thomson, and Joel A. Thornton. “Ring-Opening Yields and Auto-Oxidation Rates of the Resulting Peroxy Radicals from OH-Oxidation of α-Pinene and β-Pinene.” *Environmental Science: Atmospheres* 3, no. 2 (2023): 399–407. https://doi.org/10.1039/D2EA00133K.

Leungsakul, Sirakarn, Harvey E. Jeffries, and Richard M. Kamens. “A Kinetic Mechanism for Predicting Secondary Aerosol Formation from the Reactions of D-Limonene in the Presence of Oxides of Nitrogen and Natural Sunlight.” *Atmospheric Environment* 39, no. 37 (2005): 7063–82. https://doi.org/10.1016/j.atmosenv.2005.08.024.

Li, Haiyan, Matthieu Riva, Pekka Rantala, Liine Heikkinen, Kaspar Daellenbach, Jordan E. Krechmer, Pierre-Marie Flaud, et al. “Terpenes and Their Oxidation Products in the French Landes Forest: Insights from Vocus PTR-TOF Measurements.” *Atmospheric Chemistry and Physics* 20, no. 4 (February 21, 2020): 1941–59. https://doi.org/10.5194/acp-20-1941-2020.

Liebmann, Jonathan, Nicolas Sobanski, Jan Schuladen, Einar Karu, Heidi Hellén, Hannele Hakola, Qiaozhi Zha, et al. “Alkyl Nitrates in the Boreal Forest: Formation via the NO₃-, OH- and O₃-Induced Oxidation of Biogenic Volatile Organic Compounds and Ambient Lifetimes.” *Atmospheric Chemistry and Physics* 19, no. 15 (August 15, 2019): 10391–403. https://doi.org/10.5194/acp-19-10391-2019.

Link, Michael F., Andrew Shore, Behrang H. Hamadani, and Dustin Poppendieck. “Ozone Generation from a Germicidal Ultraviolet Lamp with Peak Emission at 222 Nm.” *Environmental Science & Technology Letters* 10, no. 8 (August 8, 2023): 675–79. https://doi.org/10.1021/acs.estlett.3c00318.

Liu, Xiaoxi, Benjamin Deming, Demetrios Pagonis, Douglas A. Day, Brett B. Palm, Ranajit Talukdar, James M. Roberts, et al. “Effects of Gas–Wall Interactions on Measurements of Semivolatile Compounds and Small Polar Molecules.” *Atmospheric Measurement Techniques* 12, no. 6 (June 13, 2019): 3137–49. https://doi.org/10.5194/amt-12-3137-2019.

Liu, Xiaoxi, Douglas A. Day, Jordan E. Krechmer, Wyatt Brown, Zhe Peng, Paul J. Ziemann, and Jose L. Jimenez. “Direct Measurements of Semi-Volatile Organic Compound Dynamics Show near-Unity Mass Accommodation Coefficients for Diverse Aerosols.” *Communications Chemistry* 2, no. 1 (August 21, 2019): 98. https://doi.org/10.1038/s42004-019-0200-x.

Logue, J. M., T. E. McKone, Sherman, M. H., and Singer , B. C. “Hazard Assessment of Chemical Air Contaminants Measured in Residences.” *Indoor Air* 21, no. 2 (2011): 92–109. https://doi.org/10.1111/j.1600-0668.2010.00683.x.

Lopez-Hilfiker, Felipe D., Siddarth Iyer, Claudia Mohr, Ben H. Lee, Emma L. D’Ambro, Theo Kurtén, and Joel A. Thornton. “Constraining the Sensitivity of Iodide Adduct Chemical Ionization Mass Spectrometry to Multifunctional Organic Molecules Using the Collision

Limit and Thermodynamic Stability of Iodide Ion Adducts." *Atmospheric Measurement Techniques* 9, no. 4 (April 6, 2016): 1505–12. https://doi.org/10.5194/amt-9-1505-2016.

Ma, Ben, Patricia M. Gundy, Charles P. Gerba, Mark D. Sobsey, and Karl G. Linden. "UV Inactivation of SARS-CoV-2 across the UVC Spectrum: KrCl* Excimer, Mercury-Vapor, and Light-Emitting-Diode (LED) Sources." Edited by Edward G. Dudley. *Applied and Environmental Microbiology* 87, no. 22 (October 28, 2021): e01532-21. https://doi.org/10.1128/AEM.01532-21.

McDonald, Brian C., Joost A. De Gouw, Jessica B. Gilman, Shantanu H. Jathar, Ali Akherati, Christopher D. Cappa, Jose L. Jimenez, et al. "Volatile Chemical Products Emerging as Largest Petrochemical Source of Urban Organic Emissions." *Science* 359, no. 6377 (February 16, 2018): 760–64. https://doi.org/10.1126/science.aaq0524.

McLean, RL. "The Mechanism of Spread of Asian Influenza: General Discussion," 1961.

Morales, Ana C., Thilina Jayarathne, Jonathan H. Slade, Alexander Laskin, and Paul B. Shepson. "The Production and Hydrolysis of Organic Nitrates from OH Radical Oxidation of B-Ocimene." *Atmospheric Chemistry and Physics* 21, no. 1 (January 8, 2021): 129–45. https://doi.org/10.5194/acp-21-129-2021.

Nardell, Edward A., Scott J. Bucher, Philip W. Brickner, Charles Wang, Richard L. Vincent, Kathleen Becan-McBride, Mark A. James, Max Michael, and James D. Wright. "Safety of Upper-Room Ultraviolet Germicidal Air Disinfection for Room Occupants: Results from the Tuberculosis Ultraviolet Shelter Study." *Public Health Reports* 123, no. 1 (January 2008): 52–60. https://doi.org/10.1177/003335490812300108.

Narita, Kouji, Krisana Asano, Yukihiro Morimoto, Tatsushi Igarashi, and Akio Nakane. "Chronic Irradiation with 222-Nm UVC Light Induces Neither DNA Damage nor Epidermal Lesions in Mouse Skin, Even at High Doses." Edited by Albert J. Fornace. *PLOS ONE* 13, no. 7 (July 25, 2018): e0201259. https://doi.org/10.1371/journal.pone.0201259.

Nault, Benjamin A., Pedro Campuzano-Jost, Douglas A. Day, Jason C. Schroder, Bruce Anderson, Andreas J. Beyersdorf, Donald R. Blake, et al. "Secondary Organic Aerosol Production from Local Emissions Dominates the Organic Aerosol Budget over Seoul, South Korea, during KORUS-AQ." *Atmospheric Chemistry and Physics* 18, no. 24 (December 14, 2018): 17769–800. https://doi.org/10.5194/acp-18-17769-2018.

Nault, Benjamin A., Philip Croteau, John Jayne, Anandi Williams, Leah Williams, Douglas Worsnop, Erin F. Katz, Peter F. DeCarlo, and Manjula Canagaratna. "Laboratory Evaluation of Organic Aerosol Relative Ionization Efficiencies in the Aerodyne Aerosol Mass Spectrometer and Aerosol Chemical Speciation Monitor." *Aerosol Science and Technology* 57, no. 10 (October 3, 2023): 981–97. https://doi.org/10.1080/02786826.2023.2223249.

Ng, Nga Lee, Steven S. Brown, Alexander T. Archibald, Elliot Atlas, Ronald C. Cohen, John N. Crowley, Douglas A. Day, et al. "Nitrate Radicals and Biogenic Volatile Organic

Compounds: Oxidation, Mechanisms, and Organic Aerosol." *Atmospheric Chemistry and Physics* 17, no. 3 (February 13, 2017): 2103–62. https://doi.org/10.5194/acp-17-2103-2017

Pagonis, Demetrios, Jordan E. Krechmer, Joost De Gouw, Jose L. Jimenez, and Paul J. Ziemann. "Effects of Gas–Wall Partitioning in Teflon Tubing and Instrumentation on Time-Resolved Measurements of Gas-Phase Organic Compounds." *Atmospheric Measurement Techniques* 10, no. 12 (December 4, 2017): 4687–96. https://doi.org/10.5194/amt-10-4687-2017.

Pagonis, Demetrios, Kanako Sekimoto, and Joost De Gouw. "A Library of Proton-Transfer Reactions of H_3O^+ Ions Used for Trace Gas Detection." *Journal of the American Society for Mass Spectrometry* 30, no. 7 (July 1, 2019): 1330–35. https://doi.org/10.1007/s13361-019-02209-3.

Pang, Jacky Yat Sing, Anna Novelli, Martin Kaminski, Ismail-Hakki Acir, Birger Bohn, Philip T. M. Carlsson, Changmin Cho, et al. "Investigation of the Limonene Photooxidation by OH at Different NO Concentrations in the Atmospheric Simulation Chamber SAPHIR (Simulation of Atmospheric PHotochemistry In a Large Reaction Chamber)." *Atmospheric Chemistry and Physics* 22, no. 13 (July 4, 2022): 8497–8527. https://doi.org/10.5194/acp-22-8497-2022.

Pankow, J F, and W E Asher. "SIMPOL.1: A Simple Group Contribution Method for Predicting Vapor Pressures and Enthalpies of Vaporization of Multifunctional Organic Compounds." *Atmos. Chem. Phys.*, 2008.

Peeters, Jozef, Luc Vereecken, and Gaia Fantechi. "The Detailed Mechanism of the OH-Initiated Atmospheric Oxidation of α-Pinene: A Theoretical Study." *Physical Chemistry Chemical Physics* 3, no. 24 (2001): 5489–5504. https://doi.org/10.1039/b106555f.

Peng, Zhe, and Jose L. Jimenez. "KinSim: A Research-Grade, User-Friendly, Visual Kinetics Simulator for Chemical-Kinetics and Environmental-Chemistry Teaching." *Journal of Chemical Education* 96, no. 4 (April 9, 2019): 806–11. https://doi.org/10.1021/acs.jchemed.9b00033.

Peng, Zhe, and Jose L Jimenez. "Radical Chemistry in Oxidation Flow Reactors for Atmospheric Chemistry Research." *Chemical Society Reviews* 49, no. 9 (2020): 2570–2616. https://doi.org/DOI https://doi.org/10.1039/C9CS00766K.

Peng, Zhe, Douglas A. Day, Guy A. Symonds, Olivia J. Jenks, Harald Stark, Anne V. Handschy, Joost A. De Gouw, and Jose L. Jimenez. "Significant Production of Ozone from Germicidal UV Lights at 222 Nm." *Environmental Science & Technology Letters* 10, no. 8 (August 8, 2023): 668–74. https://doi.org/10.1021/acs.estlett.3c00314.

Peng, Zhe, Shelly L. Miller, and Jose L. Jimenez. "Model Evaluation of Secondary Chemistry Due to Disinfection of Indoor Air with Germicidal Ultraviolet Lamps." *Environmental Science & Technology Letters* 10, no. 1 (January 10, 2023): 6–13. https://doi.org/10.1021/acs.estlett.2c00599.

Perraud, Véronique, Emily A. Bruns, Michael J. Ezell, Stanley N. Johnson, Yong Yu, M. Lizabeth Alexander, Alla Zelenyuk, et al. "Nonequilibrium Atmospheric Secondary Organic Aerosol Formation and Growth." *Proceedings of the National Academy of Sciences* 109, no. 8 (February 21, 2012): 2836–41. https://doi.org/10.1073/pnas.1119909109.

Perring, A. E., S. E. Pusede, and R. C. Cohen. "An Observational Perspective on the Atmospheric Impacts of Alkyl and Multifunctional Nitrates on Ozone and Secondary Organic Aerosol." *Chemical Reviews* 113, no. 8 (2013): 5848–70. https://doi.org/10.1021/cr300520x.

Piletic, Ivan R., and Tadeusz E. Kleindienst. "Rates and Yields of Unimolecular Reactions Producing Highly Oxidized Peroxy Radicals in the OH-Induced Autoxidation of α-Pinene, β-Pinene, and Limonene." *The Journal of Physical Chemistry A* 126, no. 1 (January 13, 2022): 88–100. https://doi.org/10.1021/acs.jpca.1c07961.

Pope, C. Arden, and Douglas W. Dockery. "Health Effects of Fine Particulate Air Pollution: Lines That Connect." *Journal of the Air & Waste Management Association* 56, no. 6 (June 2006): 709–42. https://doi.org/10.1080/10473289.2006.10464485.

Pöschl, Ulrich. "Atmospheric Aerosols: Composition, Transformation, Climate and Health Effects." *Angewandte Chemie - International Edition* 44, no. 46 (2005): 7520–40. https://doi.org/10.1002/anie.200501122.

Pusede, Sally E., Allison L. Steiner, and Ronald C. Cohen. "Temperature and Recent Trends in the Chemistry of Continental Surface Ozone." *Chemical Reviews* 115, no. 10 (May 27, 2015): 3898–3918. https://doi.org/10.1021/cr5006815.

Reichstein, Markus, Andrew D. Richardson, Micro Migliavacca, and Nuno Carvalhais. "Plant-environment interactions across multiple scales." *Ecology and the Environment.* (2014) https://doi.org/10.1007/978-1-4614-7501-9_22

Reed, Nicholas G. "The History of Ultraviolet Germicidal Irradiation for Air Disinfection." *Public Health Reports* 125, no. 1 (January 2010): 15–27. https://doi.org/10.1177/003335491012500105.

Ren, Yangang, Max McGillen, Ibrahim Ouchen, Veronique Daële, and Abdelwahid Mellouki. "Kinetic and Product Studies of the Reactions of NO3 with a Series of Unsaturated Organic Compounds." *Journal of Environmental Sciences* 95 (September 2020): 111–20. https://doi.org/10.1016/j.jes.2020.03.022.

Riley, R. L., C. C. Mills, W. Nyka, N. Weinstock, P. B. Storey, L. U. Sultan, M. C. Riley, and W. F. Wells. "Aerial Dissemination of Pulmonary Tuberculosis: A Two-Year Study of Contagion in a Tuberculosis Ward." *American Journal of Epidemiology* 142, no. 1 (1959): 3–14. https://doi.org/10.1093/oxfordjournals.aje.a117542.

Rollins, A. W., E. C. Browne, K.-E. Min, S. E. Pusede, P. J. Wooldridge, D. R. Gentner, A. H. Goldstein, et al. “Evidence for NO $_x$ Control over Nighttime SOA Formation.” *Science* 337, no. 6099 (September 7, 2012): 1210–12. https://doi.org/10.1126/science.1221520.

Ryerson, T. B., A. E. Andrews, W. M. Angevine, T. S. Bates, C. A. Brock, B. Cairns, R. C. Cohen, et al. “The 2010 California Research at the Nexus of Air Quality and Climate Change (CalNex) Field Study.” *Journal of Geophysical Research: Atmospheres* 118, no. 11 (June 16, 2013): 5830–66. https://doi.org/10.1002/jgrd.50331.

Sakamoto, Yosuke, Nanase Kohno, Sathiyamurthi Ramasamy, Kei Sato, Yu Morino, and Yoshizumi Kajii. “Investigation of OH-Reactivity Budget in the Isoprene, α-Pinene and m-Xylene Oxidation with OH under High NOx Conditions.” *Atmospheric Environment* 271 (February 2022): 118916. https://doi.org/10.1016/j.atmosenv.2021.118916.

Saunders, S M, M E Jenkin, R G Derwent, and M J Pilling. “Protocol for the Development of the Master Chemical Mechanism, MCM v3 (Part A): Tropospheric Degradation of Non-Aromatic Volatile Organic Compounds.” *Atmos. Chem. Phys.*, 2003.

Schott, Garry, and Norman Davidson. “Shock Waves in Chemical Kinetics: The Decomposition of N $_2$ O $_5$ at High Temperatures ^{1}.” *Journal of the American Chemical Society* 80, no. 8 (April 1958): 1841–53. https://doi.org/10.1021/ja01541a019.

Sekimoto, Kanako, Shao-Meng Li, Bin Yuan, Abigail Koss, Matthew Coggon, Carsten Warneke, and Joost De Gouw. “Calculation of the Sensitivity of Proton-Transfer-Reaction Mass Spectrometry (PTR-MS) for Organic Trace Gases Using Molecular Properties.” *International Journal of Mass Spectrometry* 421 (October 2017): 71–94. https://doi.org/10.1016/j.ijms.2017.04.006.

Shrivastava, Manish, Meinrat O. Andreae, Paulo Artaxo, Henrique M. J. Barbosa, Larry K. Berg, Joel Brito, Joseph Ching, et al. “Urban Pollution Greatly Enhances Formation of Natural Aerosols over the Amazon Rainforest.” *Nature Communications* 10, no. 1 (March 5, 2019): 1046. https://doi.org/10.1038/s41467-019-08909-4.

Shu, Yonghui, and Roger Atkinson. “Rate Constants for the Gas-Phase Reactions of O $_3$ with a Series of Terpenes and OH Radical Formation from the O $_3$ Reactions with Sesquiterpenes at 296 ± 2 K: GAS-PHASE REACTIONS OF O $_3$.” *International Journal of Chemical Kinetics* 26, no. 12 (December 1994): 1193–1205. https://doi.org/10.1002/kin.550261207.

Sindelarova, K., C. Granier, I. Bouarar, A. Guenther, S. Tilmes, T. Stavrakou, J.-F. Müller, U. Kuhn, P. Stefani, and W. Knorr. “Global Data Set of Biogenic VOC Emissions Calculated by the MEGAN Model over the Last 30 Years.” *Atmospheric Chemistry and Physics* 14, no. 17 (September 9, 2014): 9317–41. https://doi.org/10.5194/acp-14-9317-2014.

Spanke, Jorg, Ullar Rannik, Renate Forkel, Walter Nigge, and Thorsten Hoffmann. “Emission Fluxes and Atmospheric Degradation of Monoterpenes above a Boreal Forest: Field

Measurements and Modelling." *Tellus B* 53, no. 4 (September 2001): 406–22. https://doi.org/10.1034/j.1600-0889.2001.530407.x.

Spittler, M., I. Barnes, I. Bejan, K.J. Brockmann, Th. Benter, and K. Wirtz. "Reactions of NO3 Radicals with Limonene and α-Pinene: Product and SOA Formation." *Atmospheric Environment* 40 (January 2006): 116–27. https://doi.org/10.1016/j.atmosenv.2005.09.093.

Staudt, M., and N. Bertin. "Light and Temperature Dependence of the Emission of Cyclic and Acyclic Monoterpenes from Holm Oak (*Quercus Ilex* L.) Leaves." *Plant, Cell & Environment* 21, no. 4 (April 1998): 385–95. https://doi.org/10.1046/j.1365-3040.1998.00288.x.

Stockwell, William R., Frank Kirchner, Michael Kuhn, and Stephan Seefeld. "A New Mechanism for Regional Atmospheric Chemistry Modeling." *Journal of Geophysical Research: Atmospheres* 102, no. D22 (November 27, 1997): 25847–79. https://doi.org/10.1029/97JD00849.

Stönner, C., A. Edtbauer, and J. Williams. "Real-World Volatile Organic Compound Emission Rates from Seated Adults and Children for Use in Indoor Air Studies." *Indoor Air* 28 (2018): 164–72. https://doi.org/10.1111/ina.12405.

Sueper, Donna, 2021. https://cires1.colorado.edu/jimenez-group/ToFAMSResources/ToFSoftware/.

Talbot, E A, P Jensen, H J Moffat, and C D Wells. "Occupational Risk from Ultraviolet Germicidal Irradiation (UVGI) Lamps." *International Journal of Tuberculosis and Lung Disease* 6, no. 8 (2002): 738–41.

Taylor, W. D., T. D. Allston, M. J. Moscato, G. B. Fazekas, R. Kozlowski, and G. A. Takacs. "Atmospheric Photodissociation Lifetimes for Nitromethane, Methyl Nitrite, and Methyl Nitrate." *International Journal of Chemical Kinetics* 12, no. 4 (April 1980): 231–40. https://doi.org/10.1002/kin.550120404.

Twomey, S. "The Influence of Pollution on the Shortwave Albedo of Clouds." *Journal of the Atmospheric Sciences* 34, no. 7 (July 1977): 1149–52. https://doi.org/10.1175/1520-0469(1977)034<1149:TIOPOT>2.0.CO;2.

Vereecken, L., and J. Peeters. "Theoretical Study of the Formation of Acetone in the OH-Initiated Atmospheric Oxidation of α-Pinene." *The Journal of Physical Chemistry A* 104, no. 47 (November 1, 2000): 11140–46. https://doi.org/10.1021/jp0025173.

Wainman, Thomas, Junfeng Zhang, Charles J Weschler, and Paul J Lioy. "Ozone and Limonene in Indoor Air: A Source of Submicron Particle Exposure." *Environmental Health Perspectives* 108, no. 12 (2000).

Wang, Lingyu, and Liming Wang. “The Oxidation Mechanism of Gas-Phase Ozonolysis of Limonene in the Atmosphere.” *Physical Chemistry Chemical Physics* 23, no. 15 (2021): 9294–9303. https://doi.org/10.1039/D0CP05803C.

Wängberg, I., I. Barnes, and K. H. Becker. “Product and Mechanistic Study of the Reaction of NO 3 Radicals with α-Pinene.” *Environmental Science & Technology* 31, no. 7 (July 1, 1997): 2130–35. https://doi.org/10.1021/es960958n.

Warneke, C., P. Veres, J. S. Holloway, J. Stutz, C. Tsai, S. Alvarez, B. Rappenglueck, et al. “Airborne Formaldehyde Measurements Using PTR-MS: Calibration, Humidity Dependence, Inter-Comparison and Initial Results.” *Atmospheric Measurement Techniques* 4, no. 10 (October 31, 2011): 2345–58. https://doi.org/10.5194/amt-4-2345-2011.

Weber, Rodney J., Amy P. Sullivan, Richard E. Peltier, Armistead Russell, Bo Yan, Mei Zheng, Joost De Gouw, et al. “A Study of Secondary Organic Aerosol Formation in the Anthropogenic-influenced Southeastern United States.” *Journal of Geophysical Research: Atmospheres* 112, no. D13 (July 16, 2007): 2007JD008408. https://doi.org/10.1029/2007JD008408.

Wells, W.F. “The Environmental Control of Epidemic Contagion: I. An Epidemiologic Study of Radiant Disenfection of Air in Day Schools.” *American Journal of Epidemiology* 35, no. 1 (1942): 97–121.

Wennberg, Paul O., Kelvin H. Bates, John D. Crounse, Leah G. Dodson, Renee C. McVay, Laura A. Mertens, Tran B. Nguyen, et al. “Gas-Phase Reactions of Isoprene and Its Major Oxidation Products.” *Chemical Reviews* 118, no. 7 (April 11, 2018): 3337–90. https://doi.org/10.1021/acs.chemrev.7b00439.

Weschler, Charles J., Helen C. Shields, and Datta V. Naik. “Indoor Ozone Exposures.” *JAPCA* 39, no. 12 (December 1989): 1562–68. https://doi.org/10.1080/08940630.1989.10466650.

Weschler, Charles J., and Helen C. Shields. “Indoor Ozone/Terpene Reactions as a Source of Indoor Particles.” *Atmospheric Environment* 33, no. 15 (July 1999): 2301–12. https://doi.org/10.1016/S1352-2310(99)00083-7.

Weschler, Charles J. “Changes in Indoor Pollutants since the 1950s.” *Atmospheric Environment* 43, no. 1 (January 2009): 153–69. https://doi.org/10.1016/j.atmosenv.2008.09.044.

Wolfe, Glenn M., Margaret R. Marvin, Sandra J. Roberts, Katherine R. Travis, and Jin Liao. “The Framework for 0-D Atmospheric Modeling (F0AM) v3.1.” *Geoscientific Model Development* 9, no. 9 (September 20, 2016): 3309–19. https://doi.org/10.5194/gmd-9-3309-2016.

Xu, Lu, Hongyu Guo, Christopher M. Boyd, Mitchel Klein, Aikaterini Bougiatioti, Kate M. Cerully, James R. Hite, et al. “Effects of Anthropogenic Emissions on Aerosol Formation from Isoprene and Monoterpenes in the Southeastern United States.” *Proceedings of the*

National Academy of Sciences of the United States of America 112, no. 32 (2015): E4506–7. https://doi.org/10.1073/pnas.1512277112.

Xu, Wen, Andrew Lambe, Philip Silva, Weiwei Hu, Timothy Onasch, Leah Williams, Philip Croteau, et al. "Laboratory Evaluation of Species-Dependent Relative Ionization Efficiencies in the Aerodyne Aerosol Mass Spectrometer." *Aerosol Science and Technology* 52, no. 6 (June 3, 2018): 626–41. https://doi.org/10.1080/02786826.2018.1439570.

Zhang, Haofei, Lindsay D. Yee, Ben H. Lee, Michael P. Curtis, David R. Worton, Gabriel Isaacman-VanWertz, John H. Offenberg, et al. "Monoterpenes Are the Largest Source of Summertime Organic Aerosol in the Southeastern United States." *Proceedings of the National Academy of Sciences* 115, no. 9 (February 27, 2018): 2038–43. https://doi.org/10.1073/pnas.1717513115.